Light Control with Ordered and Disordered Nanophotonic Media

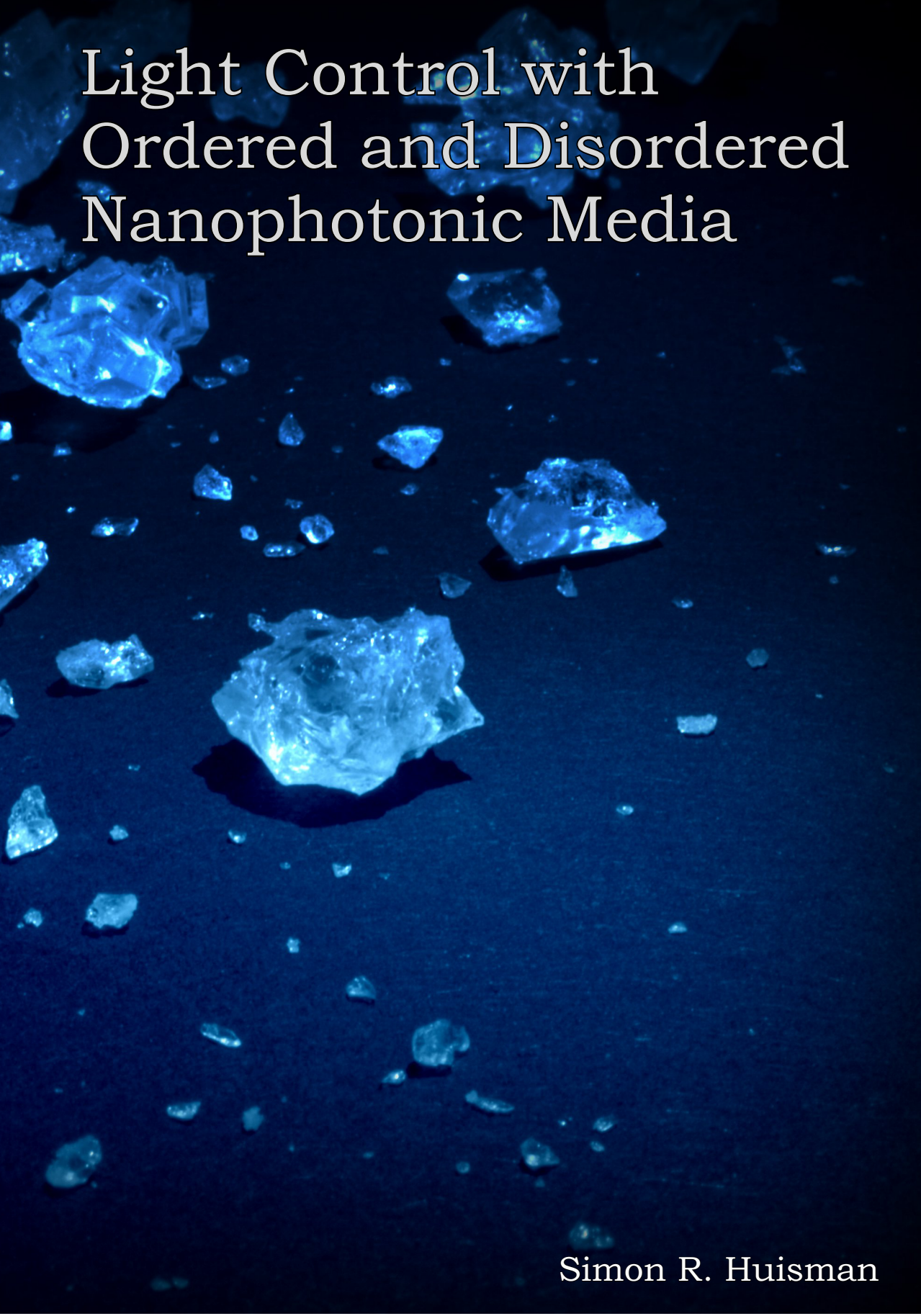

Simon R. Huisman

LIGHT CONTROL WITH ORDERED AND DISORDERED NANOPHOTONIC MEDIA

Licht temmen op de golflengteschaal met geordende en wanordelijke nanostructuren

Promotiecommissie

Promotoren	prof. dr. J.L. Herek prof. dr. W.L. Vos
Assistent-promotor	dr. P.W.H. Pinkse
Voorzitter en secretaris	prof. dr. G. van der Steenhoven
Overige leden	dr. M.P. van Exter prof. dr. L. Kuipers prof. dr. P. Lodahl prof. dr. H.J.W. Zandvliet

Cover image: photograph of sugar crystals by Simon Huisman.

This work was carried out at the Complex Photonic Systems chair (COPS) and the Optical Sciences chair (OS). Both groups are part of:

Department of Science and Technology
and MESA$^+$ Institute for Nanotechnology,
University of Twente, P.O. Box 217,
7500 AE Enschede, The Netherlands.

This work was financially supported by MESA$^+$. Additional funding was provided by FOM, NWO, STW-NanoNed, and Smartmix-Memphis.

This thesis can be downloaded from
http://www.adaptivequantumoptics.com
ISBN: 978-94-6191-829-1

LIGHT CONTROL WITH ORDERED AND DISORDERED NANOPHOTONIC MEDIA

PROEFSCHRIFT

ter verkrijging van
de graad van doctor aan de Universiteit Twente,
op gezag van de rector magnificus,
prof. dr. H. Brinksma,
volgens besluit van het College voor Promoties
in het openbaar te verdedigen
op woensdag 11 september 2013 om 16.45 uur

door

Simon Reinald Huisman

geboren op 26 mei 1986
te Naarden

Dit proefschrift is goedgekeurd door:

prof. dr. J.L. Herek en prof. dr. W.L. Vos

Contents

CHAPTER 1

Introduction

There is a strong worldwide drive to fundamentally control the behavior of light with tailored nanophotonic media. Ordered, weakly disordered, and completely disordered nanophotonic media exhibit unique light transport properties that make them unprecedented and versatile platforms for, *e.g.*, tailoring light emission, sculpting integrated linear optical circuits, controlling quantum interference, and exploring novel fundamental physics.

Nanophotonic media are composite dielectric optical materials in which the refractive index spatially varies on length scales comparable to the wavelength of light. Light propagation in nanophotonic media strongly deviates from rectilinear plane wave propagation in homogenous media by optical interference in the multiple-scattering structure [1–9]. Nanophotonic media uniquely define light propagation and enhance or decrease interactions with the light field as a consequence of the rich dispersion characteristics. The wide availability of high refractive index materials, scalable fabrication methods with nanometer accuracy, and reversible refractive-index control mechanisms, make nanophotonic media a key technology of modern optics.

Both ordered nanophotonic media [10–12], such as photonic crystals, and disordered media [13, 14], such as white paint, have been topic of intense research for many decades and have found their way even in daily used devices such as white light LEDs and solar cells. Available fabrication methods make ordered nanophotonic media ideally suited for mass production. Nevertheless, any fabricated structure contains intrinsic disorder, and therefore it is essential to understand the impact of unavoidable deviations from designed structures. Furthermore, weak disorder results in phenomena that are also observed in on-purposely designed delicate structures, such as cavities with high quality factors [15], opening new opportunities to embrace disorder for functionality. Disordered systems even support intriguing quantum correlations [16–23]. Quantum optics in nanophotonic media is a promising candidate for practical implementation of quantum technology, since devices are compact, scalable, have minor losses, and support enhanced fields [24, 25]. With recent progress in programming classical light propagation in random multiple-scattering media by wavefront shaping [26, 27], the road is open to exploit strongly disordered nanophotonic media for integrated quantum optics.

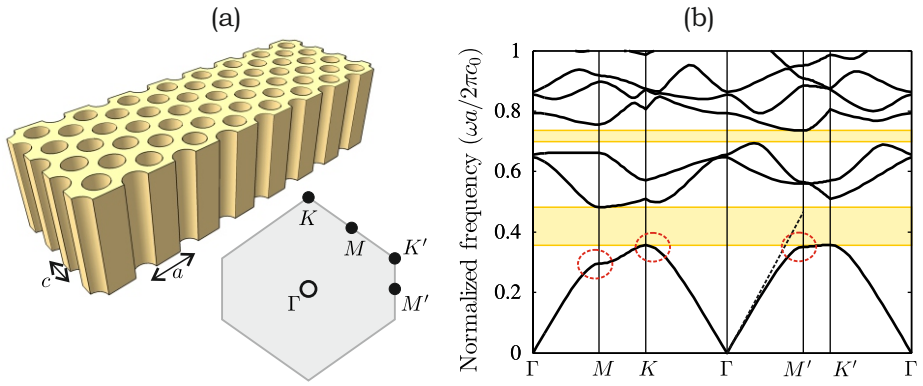

Figure 1.1. Geometry and dispersion of a two-dimensional photonic crystal. (*a*) Geometry of a macroporous two-dimensional silicon photonic crystal with a centered-rectangular lattice with a unit cell with long side a, short side c and pore radius r. The bottom shows the corresponding Brillouin zone in reciprocal space, where the labels mark points of high symmetry. (*b*) Calculated band structure for $r/a = 0.225$ and $a/c = 1.41$ for transverse-electric (TE) polarized light. The band structure shows two two-dimensional band gaps for TE-polarized light (yellow bars) and regimes that sustain slow-light propagation (red encircled areas). The dashed diagonal line indicates a fraction of the dispersion for rectilinear plane wave propagation in a homogeneous medium with constant effective refractive index similar to the one of the crystal.

1.1. Ordered nanophotonic media: photonic crystals

Photonic crystals are long-range periodic ordered two- or three-dimensional nanophotonic media with a periodicity of the order of the wavelength of light [6]. Light propagation in photonic crystals has much in common with electron transport in solid-state systems [28, 29]. The key difference is that light is represented by a vector field that is occupied by bosonic massless quanta known as *photons*. Nevertheless, just like electrons in semiconductors, the resulting interference of multiple-scattered light restricts the allowed fields to be a superposition of Bloch modes. The optical Bloch modes exhibit a rich dispersion that strongly deviates from the linear dispersion relation in homogenous materials. The dispersion makes photonic crystals ultimate tools to, *e.g.*, control spontaneous emission, redirect, and slow-down light propagation.

Figure 1.1 shows the geometry and dispersion relation for a two-dimensional photonic crystal. The dispersion can be calculated by solving the Maxwell's equations inside the photonic medium, analogous to solving the Schrödinger equation for electrons propagating in a solid-state crystal.[1] Methods are described in

[1] The optical Helmholtz equation contains a second-order time derivative, resulting in a linear dispersion relation between energy and wave vector. The Schrödinger equation contains a first-order time derivative, resulting in a quadratic dispersion relation between energy and

Refs. [6, 30]. The dispersion relation of light in photonic crystals exhibits four characteristics features that are studied in this dissertation:

1. Frequency bands emerge in which there are no modes. Hence, light cannot propagate in a certain direction by Bragg diffraction, known as *stop gaps*.[2] Light at the frequency and direction of the stop gap cannot be transmitted and therefore gets scattered in other allowed directions. The effect is well known in one-dimensional structures such as Bragg mirrors. Stop gaps are especially useful to confine light on few-wavelength scales in, *e.g.*, photonic-crystal waveguides and cavities, or to diffract light with high efficiency. A *photonic band gap* is a common stop gap for all directions and polarizations. Figure 1.1(b) reveals two two-dimensional photonic band gaps for TE-polarized light.[3]

2. The dispersion strongly deviates from that of a homogeneous material, especially near the band edge of a stop gap. Figure 1.1(b) illustrates the linear dispersion in a homogoneous material by the diagonal dashed line between $\Gamma M'$. In contrast, the band becomes curved for the photonic crystal if light travels along $\Gamma M'$. The group index n_{eff} is given by the inverse slope of the band $n_g = (1/c_0)(\partial\omega/\partial k)^{-1}$. The group velocity is given by $v_g = c_0/n_g$ and describes the rate at which energy travels. The group index is strongly frequency-dependent and diverges near the band edge, leading to *slow light*. The red encircled areas in Fig. 1.1(b) mark regions where slow light occurs. Slow light is extremely useful in optical sensing, as slow light interacts strongly with matter. The energy density of the pulse is determined by the energy of the pulse and its spatial extent. If we assume that all the energy of the pulse has been transmitted into the medium, slowing down the speed of light results in a higher energy density in the medium. In a photonic crystal, this results in an increase of the intensity in the medium, roughly proportional to the inverse of the group velocity [31]. Another intriguing consequence is that an incident pulse is reshaped since certain frequencies travel faster through the crystal. The locus of maximum constructive interference, the pulse's peak, is shifted forward toward the leading edge of the pulse, so that the peak of a replica of the original pulse seems to arrive before the peak of a similar pulse propagating through a nondispersive medium with the same group index [32].

3. The modified dispersion can result in a noticeable effect in the frequency-dependent number of modes, defined as the *density of optical states* (DOS).

wave vector.

[2] There is the unfortunate habit of confusing the term stop gap, stop band and band gap. There is a fundamental difference between them that is explained in this section.

[3] The term photonic band gap is also used to describe a common stop gap in two-dimensional structures. The light field cannot be absent everywhere, because diffraction in the third dimension is absent. Often a common two-dimensional stop gap is formed for a specific polarization only. Therefore in the case of for example triangular photonic crystals, one should speak about a two-dimensional band gap for transverse-electric polarized light.

The geometry and dimension of the structure determine whether the modified dispersion will appear in the DOS. For one-dimensional structures and propagation, any modification of the dispersion of the modes will be likely noticeable since there are few modes at the same frequency that can counteract or average out this effect; a stop gap would result immediately in a $\mathrm{DOS}^{(1D)}$ of 0 and a divergence near the band edge. In three-dimensional structures, an altered dispersion might not be noticeable in the DOS, since there are many other modes at the same frequency that contribute. Therefore a stop gap for a single direction might hardly affect the DOS, while a photonic band gap would give a DOS of 0 by definition. The modification of the DOS has drastic consequences for phenomena that are caused by the interaction with the (vacuum) field, such as spontaneous emission and Casimir forces.

4. The crystal modes are Bloch modes and therefore have a particular mode profile different from a plane wave. A Bloch mode in a crystal with periodicity a propagating in the $\hat{\mathbf{k}}$ direction with wave vector $\mathbf{k} = |\mathbf{k}|\,\hat{\mathbf{k}}$, at position $\mathbf{r}$, and frequency ω, is described by:

$$\Psi_{\mathbf{k}}(\mathbf{r},\omega) = \psi(\mathbf{r},\omega)\exp\left(\mathrm{i}\mathbf{k}\cdot\mathbf{r}\right). \tag{1.1}$$

Here $\psi(\mathbf{r},\omega)$ is an envelope that is periodic with the lattice and satisfies $\psi(\mathbf{r},\omega) = \psi(\mathbf{r} + a\hat{\mathbf{k}},\omega)$. The Bloch envelope can be expanded as:

$$\psi(\mathbf{r},\omega) = \sum_m a_m(\omega)\exp(\mathrm{i}m\frac{2\pi}{a}\mathbf{r}\cdot\hat{\mathbf{k}}). \tag{1.2}$$

All Bloch modes have harmonics in all Brillouin zones, including one harmonic in the first irreducible Brillouin zone. Therefore, we consider in this dissertation mainly folded band structures, such as shown in Fig. 1.1(b).

1.1.1. Stop gaps, stop bands and band gaps

Stop gaps are unique properties of photonic crystals that form true forbidden zones for light. The presence of stop gaps can be explained with both Bragg diffraction or the von Laue diffraction condition, which are equivalent descriptions of elastic scattering and propagation of any kind of wave phenomenon in a periodic lattice [28, 33].

Bragg diffraction describes scattering in real space. Figure 1.2(a) illustrates the geometry for simple Bragg diffraction. Scattered waves on a set of lattice planes interfere constructively if the Bragg condition is met:

$$m\lambda = 2dn_{\mathrm{eff}}\cos(\theta), \tag{1.3}$$

where m is an integer, λ is the wavelength in vacuum, d is the lattice spacing, n_{eff} the effective refractive index and θ the angle of the incident wave with the normal to the lattice planes. Incident waves that satisfy the Bragg condition for

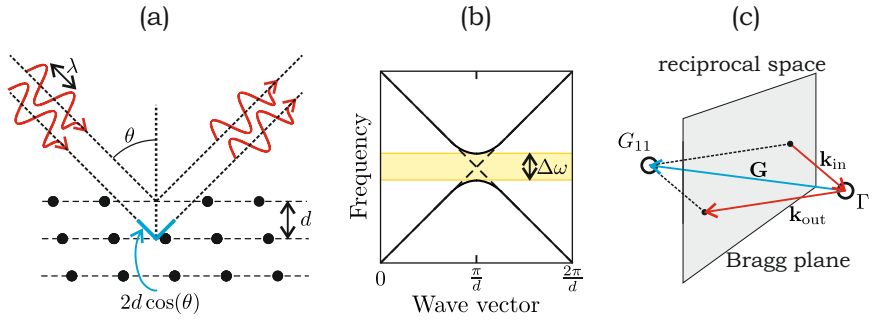

Figure 1.2. Formation of stop gaps in photonic crystals. (*a*) Illustration of simple Bragg diffraction on a set of lattice planes with lattice spacing d. Constructive interference of the scattered waves occurs if the path length difference $2d\cos(\theta)$ (blue) between reflections from successive planes equals an integer number of wavelengths λ. (*b*) Dispersion relation along the normal to the lattice planes in (*a*). At the Bragg condition $k = \pi/d$, the dispersion relation (black) splits and forms a stop gap (yellow). In the limit of vanishing photonic interaction, the dispersion relation shows no stop gaps (dashed lines). (*c*) The von Laue condition is satisfied if scattered wave vectors are bisected by a Bragg plane. The incident wave vector $\mathbf{k}_{\text{in}}$ and outgoing wave vector $\mathbf{k}_{\text{out}}$ lie on this Bragg plane. The difference vector $\mathbf{k}_{\text{out}} - \mathbf{k}_{\text{in}}$ is equal to the reciprocal lattice vector $\mathbf{G}$ that extends between Γ and G_{11}.

a set of lattice planes are diffracted for a range of frequencies, forming a stop gap in the dispersion relation. The dimensionless photonic strength S can be physically defined as the polarizability per unit cell volume [34]. The photonic strength of a crystal is gauged by the relative width $\Delta\omega/\omega_{\text{center}}$ of the main stop gap. The interaction strength between light and a crystal increases with the dielectric contrast between the composite materials [9, 35], resulting into broader stop gaps. The Bragg length L_b is the typical length scale that is required for Bragg diffraction to occur. The Bragg length is related to the photonic strength as $L_b = \lambda_{\text{center}}/\pi S$, with λ_{center} the center wavelength of the stop gap.

The solid curves in Fig. 1.2(*b*) indicate the dispersion relation for light in a one-dimensional photonic structure. At the Bragg condition ($k = \pi/d$), there exist two standing waves: one mostly in the medium with high refractive index (low frequency band) and one mostly in the medium with low refractive index (high frequency band) [6, 30]. These standing waves result in different frequencies of light, which form the edges of the stop gap $\Delta\omega$. Stop gaps are the result of destructive interference of Bloch modes inside the crystal. Therefore, true stop gaps only exist in structures of infinite size. The modes in a structure of finite size are still strongly suppressed by Bragg diffraction. In real photonic crystals, the width of reflectivity peaks gauge *stop bands* to indicate the difference from infinite and perfect structures.[4]

[4] Stop bands are experimentally observed frequency regions for which light cannot propagate

An alternative formulation for diffraction of waves is provided by the von Laue condition [28, 37]. The von Laue approach describes scattering in reciprocal space and differs from the Bragg approach in that no particular sectioning of the crystal into lattice planes is singled out, and no ad hoc assumption of specular reflection is imposed. One regards the crystal as composed of identical microscopic objects placed at the sites of a Bravais lattice, each object can scatter the incident radiation in all directions. Constructive interference occurs in directions and at wavelengths for which the radiation scattered from all lattice points interfere constructively. This occurs when the difference between the incident wave vector $\mathbf{k}_{\text{in}}$ and outgoing wave vector $\mathbf{k}_{\text{out}}$ is equal to a reciprocal lattice vector $\mathbf{G}$:

$$\mathbf{k}_{\text{out}} - \mathbf{k}_{\text{in}} = \mathbf{G}. \tag{1.4}$$

This condition is called the von Laue condition and describes diffraction of waves in reciprocal space. The von Laue condition is satisfied at certain planes in reciprocal space, called Bragg planes. Wave vectors $\mathbf{k}_{\text{in}}$ and $\mathbf{k}_{\text{out}}$ satisfy the von Laue condition if the tips of both vectors lie in a plane that is the perpendicular bisector of a line joining the origin of reciprocal space to a reciprocal lattice vector $\mathbf{G}$, as illustrated in Fig. 1.2(c). In reciprocal space, the points on the boundary of the Brillouin zone, which is enclosed by Bragg planes, are special because every wave with a vector extending from the origin to the zone boundary both satisfies the von Laue condition and Bragg condition.

Diffraction becomes more complex in the case of multiple-Bragg wave coupling. With increasing photonic interaction and increasing frequency, light can diffract from more than one set of lattice planes simultaneously [38]. Such multiple-Bragg diffraction results in band repulsions between Bloch modes, causing the frequencies of the edges of the stop gaps to become independent of angle of incidence. In reciprocal space, this can occur at a corner of the Brillouin zone edge at the intersection of multiple Bragg planes.

In the limit of strong photonic interaction, many Bloch modes interact so strongly that the edges of the stop gaps hardly vary for all propagation directions. This results in a photonic band gap [38, 39]. Only specific three-dimensional photonic crystals have a band gap if the refractive index contrast is sufficiently high: the simple cubic [40], the diamond [41] and diamond-like [42] structures, such as the Yablonovite structure [43], the woodpile [44], and the close packed *fcc* and *hcp* structures [45].

Experimentally realizing a photonic band gap is a tremendous challenge. One needs a state-of-the-art structure with a minimum amount of disorder, since disorder reduces the width of the gaps by the formation of defect states.[5] The fabricated structure is of finite size and therefore a suppressed DOS is expected if

due to Bragg diffraction. These can be observed in diffraction measurements, like reflectance or transmission spectroscopy. Not every reflectance peak or transmission trough is caused by interference, it can also be caused by, *e.g.*, absorption or bad coupling to crystal modes [6, 36].

[5] A famous example is the observed inhibited spontaneous emission rates in inverse opal photonic crystals. A very narrow band gap is expected between higher order modes. Because of small imperfections this gap will close, and therefore it is hard to claim the presence of the photonic band gap.

there exists a common stop band for all directions and polarizations. To confirm the presence of a band gap one has to demonstrate (*i*) a common stop band and (*ii*) a strong suppression of the DOS. Each demonstration in itself is not sufficient to conclude there is a band gap, since both separate observations can be caused by different effects, such as bad mode coupling, incomplete gap for all directions, and measuring emission statistics from sources distributed at specific locations in the structure resulting in an improper ensemble average for the DOS. We have recently demonstrated both criteria for the presence of a photonic band gap in inverse woodpile photonic crystals [46, 47].

1.2. Weakly disordered nanophotonic media: photonic-crystal waveguides

One cannot engineer a perfectly long-range ordered system; there is always disorder caused by, *e.g.*, material impurities and fabrication. In the end, the third law of thermodynamics forbids perfectly long-range ordered structures. Random multiple scattering forces light to follow a random walk through the material, resulting in diffuse light transport if interference effects are neglected. For very pronounced random scattering, when the distance between succeeding scattering events is in the order of a wavelength, interference cannot be ignored and ultimately light can become Anderson localized [13, 48]. Anderson localization is an ensemble-averaged effect where waves cannot propagate through a medium by interference, where disorder prevents waves to be in a propagating state. In Anderson localization light performs random walks that return to their origin after traveling a path length comparable to the wavelength of light. In three-dimensional structures this is most difficult to achieve since a phase transition must be crossed. But for one- and two-dimensional disordered structures of infinite size, light will always become localized.

Sheng explains that Anderson localization is not necessarily the same as wave confinement [49]. Wave confinement may involve walls made of materials that have no wave state at the relevant frequency, such as standing waves formed in a cavity. Gaps in finite-size photonic crystals are typical examples where the waves evanescently decay and therefore such crystals form excellent materials to confine light in nanocavities or waveguides. The crucial difference between confinement caused by a stop gap and Anderson localization is that a gap denotes a frequency range which is empty of wave states, whereas a localized wave is a non-propagating wave state. The two mechanisms can interact, especially in weakly disordered gap media in which the crystalline periodicity is perturbed by disorder. The band edge of the gaps would be smeared to form a transition regime. In that transition regime there would be spatial regions that are deficit of wave states, so that instead of total confinement, the waves would be restricted in their propagation directions. That is, instead of propagating in straight lines, the waves would be traveling in a labyrinth. Another way of saying the same thing is that the amount of random scattering is increased, leading to the enhancement of localization effect. That is why the band edge states are easily localized.

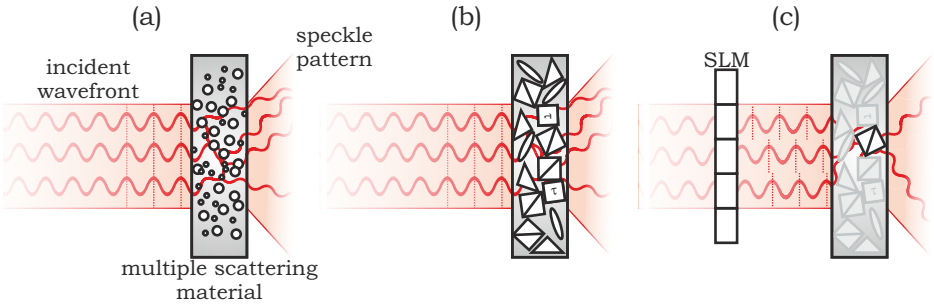

Figure 1.3. Wavefront-shaped adaptive linear optical circuits. (*a*) Incident light on a multiple-scattering medium results in a speckle pattern. (*b*) The scattered light can be described by a scattering matrix, representing a complicated linear optical circuit. (*c*) By modulation of the incident wavefront with a spatial light modulator (SLM) it becomes possible to address elements to create a speckle pattern with desired correlations for functionality, in this cartoon a beam splitter. Note: reflection is omitted in this figure for clarity.

Photonic-crystal waveguides form an excellent platform to investigate this effect.

Photonic-crystal waveguides consist of a two-dimensional photonic-crystal slab with a line defect. Light is confined in the line defect by Bragg diffraction in the surrounding photonic crystal, and total internal reflection. The Bloch modes guided by the line defect exhibit dispersion essential for slow-light propagation and enhanced light-matter interactions [6, 50–53]. The slow light is extraordinarily sensitive to unavoidable structure imperfections. Consequently, the light undergoes unintended multiple scattering, which ultimately leads to a blockade of its propagation by Anderson localization. The Anderson-localized modes were first observed in 2007 to form random cavities with a relative inverse linewidth of $Q \simeq 10^4$ [15]. It has been demonstrated that Anderson localization in photonic-crystal waveguides control the spontaneous emission decay rates of embedded quantum dots [18, 54]. Phase-sensitive near-field scanning optical microscopy (NSOM) is ideally suited to study the localized modes, because of its ability to probe evanescent fields with sub-wavelength resolution, and extract the dispersion [51, 55–59].

1.3. Disordered nanophotonic media: adaptive quantum optics

Light transport in any scattering nanophotonic medium can be described by a linear transformation of a multi-mode system by a scattering matrix. The scattering matrix of random multiple-scattering media, such as white paint, contains correlations that are very similar to correlations describing light transport in linear optical elements, in essence forming a very complicated linear optical circuit with many input and output modes. The output modes are generally known

as far-field speckle spots. Freund suggested that these correlations in random multiple-scattering media can be exploited for creating the functionality of linear optical elements [60]. This makes random multiple-scattering one of the most versatile platforms for creating linear optical circuits.

Wavefront shaping is an adaptive optical technique in which an incident wavefront on a scattering medium is modulated to obtain a speckle pattern with desired correlations. This technique allows for a complete control of light propagation in strongly-scattering media in space and time [26, 27]. The concept behind wavefront shaping is illustrated in Fig. 1.3. In essence one controls by modulating, *e.g.*, the phase of the incident wavefront the degree of mode-mixing of all scattered waves that contribute to a target speckle pattern with desired correlations. Although wavefront shaping has been generally known for focusing and imaging with multiple-scattering media, many linear optical components have been realized such as equivalents of waveguides and lenses [26, 61, 62], optical pulse compressors [63, 64], programmable waveplates [65], and plasmonic grating couplers [66]. Since one is in general not able to control all incident modes of the scattering matrix, and the scattering matrix might not contain all desired correlations, one has to tolerate losses that are typically orders of magnitude higher than of custom fabricated optical circuits. On the other hand, the created optical circuit is inherently programmable in functionality.

1.3.1. Wavefront shaping of quantum light

Quantum optics has given us groundbreaking insights in the most fundamental nature of light [32, 67]. We are now able to create, manipulate and characterize quantum states of the light field, making quantum optics of interest for applications [68, 69]. In most quantum optical experiments, the prepared quantum state propagates through an interferometric linear optical circuit. Even simple linear optical circuits, like a Mach-Zehnder interferometer, reveal unique phenomena relevant for establishing building blocks for quantum computing. These optical circuits are often realized either in bulky setups containing, *e.g.*, mirrors, lenses, polarizes, waveplates, or in state-of-the-art integrated photonics, such as coupled waveguides and cavities. Integrated photonic structures form an excellent platform for a practical implementation of quantum optics for three reasons: (*i*) the size of integrated photonics makes these circuits scalable. (*ii*) The light field can be enhanced by orders of magnitude with a mode volume below the wavelength cubed. (*iii*) State-of-the-art fabrication technologies reduce significantly the amount of disorder that would degrade quantum interference of two or more photons [24, 25].

Both free-space and integrated photonic linear optical circuits are robust platforms for performing quantum optical experiments with low optical losses. However, once the linear optical circuit has been built, one has often little flexibility in modifying or programming the evolution of the state, especially in a running experiment. One can design the experiment to partly circumvent this issue by including adaptive optical elements, which mostly give a controllable (phase)delay [70]. Quantum interference can be optimized both in the spatial domain and in

the time domain. Especially in nanophotonic structures much effort is invested in controlling the refractive index by, *e.g.*, temperature tuning, free-carrier excitation or optical Kerr switching [71–73]. Nevertheless, it becomes a major challenge if one would like to give the optical circuit a functionality that is entirely different from its original design purpose, *e.g.*, changing the number of input and output modes.

Random multiple scattering has become an exciting platform for quantum optical experiments [16–19, 21, 74, 75]. We introduce *adaptive quantum optics* in which wavefront shaping is applied to quantum light to obtain ample flexibility in programming the linear optical circuit for desired quantum interference. Spatial light modulation in combination with quantum light has been applied to quantum imaging, orbital momentum selection, and creating high-dimensional entangled states [76–80]. Since quantum correlations are conserved even in random multiple-scattering media, it becomes possible to optimize quantum interference. An important breakthrough is the recent capability to measure parts of the scattering matrix for randomly-scattering media [81]. This offers a promising route towards programming the desired effective transmission matrix for the incident light for the target quantum interference.

We have started a series of experiments to demonstrate the power of adaptive quantum optics. The best known example of quantum interference is the Hong-Ou-Mandel (HOM) experiment in which two indistinguishable photons are incident on the input ports of a 50:50 beam splitter. Quantum interference dictates that the photons always leave the beam splitter in pairs in either of the two output modes. We are working towards demonstrating adaptive quantum optics by repeating this experiment with phase modulation of the incident wavefronts and a multiple-scattering medium instead of the beam splitter.

Before one can demonstrate HOM interferometry with adaptive quantum optics, one has to demonstrate (*i*) the capability of wavefront shaping incident single-photon states and (*ii*) the capability of making a speckle pattern with correlations like an optical beam splitter. In this dissertation we demonstrate both aspects.

1.4. Overview of this dissertation

This dissertation describes six experiments in which light propagation is controlled with nanophotonic media. Each experiment forms the basis of a manuscript that has been accepted or submitted for publication. Therefore the chapters follow closely the original manuscript with updates added on. The experiments are thematically grouped in three parts.

Part I: Forbidden zones for light in photonic band gap crystals

State-of-the-art photonic crystals have been investigated with reflectance spectroscopy. The following chapters report two experiments that demonstrate light control by the close-to-perfect periodicity of the crystals.

In chapter 2 a novel diffraction phenomena is identified which is called *sub-Bragg*-diffraction. Sub-Bragg diffraction is multiple-Bragg diffraction in a direction of high symmetry, which occurs at a lower frequency than simple-Bragg diffraction. Sub-Bragg diffraction is even a general wave diffraction phenomenon that occurs in many different Bravais lattices, including the commonly known triangular and body-centered cubic lattices.

Chapter 3 presents an experimental signature of a photonic-band gap in three-dimensional inverse woodpile photonic crystals. A unique combination of polarization-resolved and position-dependent reflectance spectroscopy presents a strong signature of the presence of a photonic band gap, without the necessity to rely on calculated band structures or studying decay rates of embedded emitters.

Part II: Light near the band edge in photonic-crystal waveguides

The periodicity of the lattice makes photonic-crystal waveguides intriguing systems for slow light and enhanced light-matter interactions. Random deviations of the ideal non-disordered lattice are unavoidable. Especially near the band edge, the effects of weak disorder strongly alter light transport compared to ideal non-disordered structures. Phase-sensitive near-field microscopy is used to study light propagation in photonic-crystal waveguides.

Photonic-crystal waveguides are multi-mode systems, that are in general detected all at once with near-field microscopy. Chapter 4 describes a Bloch-mode reconstruction algorithm that has been tested on photonic-crystal waveguides. This algorithm allows for the extraction of field patterns of separate Bloch modes.

In chapter 5 Anderson-localized modes are observed near the band-edge. The experimentally measured band structure reveals a broadening of the band edge. The density of states is reconstructed revealing a smeared van Hove singularity and the optical equivalent of the Lifshitz tail.

Part III: Adaptive quantum optics

Disordered nanophotonic media contain correlations that are similar to those of linear optical elements. With wavefront shaping one can address these correlations for functionality. Two experiments are presented that form essential building blocks for a HOM experiment with adaptive quantum optics.

In chapter 6 wavefront shaping is applied to incident single-photon Fock states on a layer of white paint. The probability that a single photon arrives at a target speckle spot is increased 30 fold by phase modulation of the incident wavefront. This proof-of-principle experiment constitutes the first demonstration of wavefront shaped non-classical light. This experiment opens the road to address correlations in multiple-scattering media for desired quantum interference.

Chapter 7 demonstrates that a random scattering medium can be used as a balanced beam splitter by wavefront shaping. Two orthogonal wavefronts are phase modulated to create two enhanced output speckle spots of equal intensity. Interference measurements show that the output speckle spots are correlated like the ports of a coherent balanced beam splitter.

Forbidden zones for light in photonic band gap crystals. Photonic crystals are a special class of meta-materials that radically control emission and propagation of light. In specific three-dimensional crystals, a common frequency range is formed for which light is not allowed to propagate in any direction, called the photonic band gap. It is an outstanding challenge to create these crystals and experimentally demonstrate the photonic band gap. Photo: microscope image of an inverse woodpile photonic crystal surrounded by a two-dimensional crystal. Photo courtesy of Hannie van den Broek.

Part I.

Forbidden zones for light in photonic band gap crystals

CHAPTER 2

Observation of sub-Bragg diffraction of waves in crystals

We investigate the diffraction conditions and associated formation of stop gaps for waves in crystals with different Bravais lattices. We identify a prominent stop gap in high-symmetry directions that occurs at a frequency below the ubiquitous first-order Bragg condition. This sub-Bragg diffraction condition is demonstrated by reflectance spectroscopy on two-dimensional photonic crystals with a centered rectangular lattice, revealing prominent diffraction peaks for both the sub-Bragg and first-order Bragg condition. These results have implications for wave propagation in 2 of the 5 two-dimensional Bravais lattices and 7 out of 14 three-dimensional Bravais lattices, such as centered rectangular, triangular, hexagonal and body-centered cubic.

2.1. Introduction

The propagation and scattering of waves such as light, phonons and electrons are strongly affected by the periodicity of the surrounding structure [28, 29]. Frequency gaps called stop gaps, emerge for which waves cannot propagate inside crystals due to Bragg diffraction. Bragg diffraction is important for crystallography using X-ray diffraction [82] and neutron scattering [83]. Diffraction determines electronic conduction of semiconductors [28, 29] and of graphene [84], and broad gaps are fundamental for acoustic properties of phononic crystals [85, 86] and optical properties of photonic metamaterials [4, 6].

Bragg diffraction is described in reciprocal space by the Von Laue condition $\mathbf{k}_{\mathrm{out}} - \mathbf{k}_{\mathrm{in}} = \mathbf{G}$, where $\mathbf{k}_{\mathrm{out}}$, $\mathbf{k}_{\mathrm{in}}$ are the outgoing and incident wave vectors and $\mathbf{G}$ is a reciprocal lattice vector. As a result, a plane exists in reciprocal space that bisects the reciprocal lattice vector for which the Von Laue condition is satisfied, called a Bragg plane. When the incident and outgoing wave vectors are located on a Bragg plane these waves are hybridized, thereby opening up a stop gap at the Bragg condition. The boundary of the Brillouin zone is formed by intersecting Bragg planes and therefore gaps open on this boundary [28]. When diffraction involves a single Bragg plane, we are dealing with simple Bragg diffraction, which corresponds in real space with the well-known Bragg condition: $m\lambda = 2d\cos(\theta)$. Here m is an integer, λ is the wavelength inside the crystal, θ is

The content of this chapter has been published as: S.R. Huisman, R.V. Nair, A. Hartsuiker, L.A. Woldering, A.P. Mosk, and W.L. Vos, Phys. Rev. Lett. **108**, 083901 (2012).

the angle of incidence with the normal to the lattice planes, and d is the spacing between the lattice planes. A stop gap is also formed when Bragg diffraction occurs on multiple Bragg planes simultaneously, which is called multiple Bragg diffraction [87], and is fundamental for band gap formation [29, 38, 88]. Wave propagation in crystals is most often described along high-symmetry directions [28], since extrema occur in these directions. Multiple Bragg diffraction has been recognized in high-symmetry directions at frequencies above the first-order simple Bragg diffraction condition, where the simple Bragg diffraction condition is given by: $m = 1$, $\lambda = 2d$ or $\mathbf{k}_{\mathrm{out}} = -\mathbf{k}_{\mathrm{in}} = (1/2)\mathbf{G}$. For low-symmetry directions, multiple Bragg diffraction can occur at a frequency lower than simple Bragg diffraction [39, 89], which occurs in higher-order Brillouin zones. To our knowledge, for high-symmetry directions, multiple Bragg diffraction has not yet been observed at frequencies below simple Bragg diffraction.

In this chapter we show that for high-symmetry directions multiple Bragg diffraction can occur at frequencies[1] *below* the first order simple Bragg condition. As a demonstration we have investigated diffraction conditions for two-dimensional (2D) photonic crystals using reflectance spectroscopy. A broad stop gap is observed below the simple Bragg condition, depending on the symmetry of the lattice. Our findings are not limited to light propagation, but apply for wave propagation in general, and therefore we anticipate similar diffraction for electrons in graphene [84], and sound in phononic crystals [85, 86].

2.2. Reflectance spectroscopy on 2D photonic crystals with sub-Bragg diffraction

We have studied light propagation in 2D silicon photonic crystals [90]. Figure 2.1(a) shows a scanning electron microscope (SEM) image of one of these crystals from the top view. The centered rectangular unit cell has a long side $a = 693 \pm 10$ nm and a short side $c = 488 \pm 11$ nm. The pores have a radius of $r = 155 \pm 10$ nm and are approximately 6 μm deep. The photonic crystals are cleaved parallel to either the a-side or c-side of the unit cell. The cleavages define two directions of high symmetry, $\Gamma M'$ and ΓK, in the Brillouin zone, see Fig. 2.1(b). If light travels parallel with these directions, one expects simple Bragg diffraction from the lattice planes in real space (dashed lines in Fig. 2.1(a)). A stop gap should appear that is seen in reflectivity as a diffraction peak. Because both directions have a high symmetry, one naively expects that simple Bragg diffraction gives the lowest-frequency diffraction peak.

We have identified the diffraction conditions of our 2D photonic crystals along the $\Gamma M'$ and ΓK directions using reflectance spectroscopy [46]. The photonic crystals are illuminated with white light from a supercontinuum source (Fianium SC-450-2). TE-polarized light is focused on the crystal using a gold-coated reflecting objective (Ealing X74) with a numerical aperture of 0.65, resulting in a spectrum angle-averaged over 0.44π sr $\pm 10\%$ solid angle in air. By assuming an

[1] In this chapter we consider frequency, since this is a conserved quantity for waves.

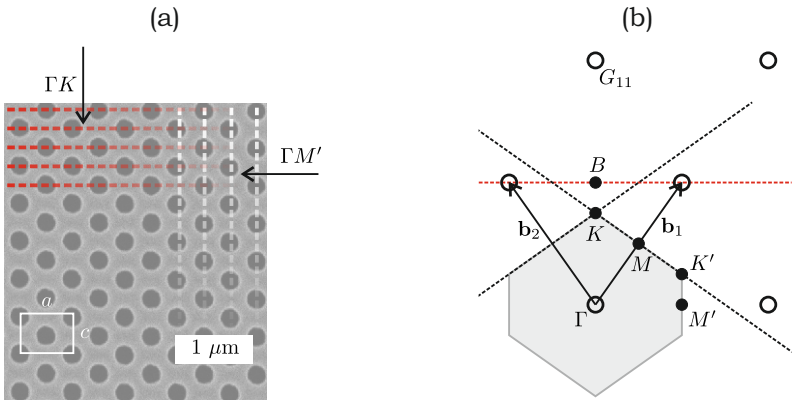

Figure 2.1. Geometry of 2D photonic crystals with a centered rectangular lattice. (a) SEM image of a 2D photonic crystal with a centered rectangular lattice. The white rectangle marks a unit cell with $a = 693 \pm 10$ nm, $c = 488 \pm 11$ nm and $r = 155 \pm 10$ nm. The arrows mark two directions of high symmetry ΓK and $\Gamma M'$. The red and gray dashed lines mark real space lattice planes whose lowest-frequency simple Bragg diffraction occurs along the ΓK and $\Gamma M'$ directions. (b) Reciprocal space of the centered rectangular lattice (circles). The filled area is the first Brillouin zone, $\mathbf{b}_1$ and $\mathbf{b}_2$ are primitive vectors. Γ, K, K', M, and M' are points of high symmetry. The dashed lines are Bragg planes.

average refractive index ($n_{\text{eff}} = 2.6$), the angular spread inside the crystal is only 14^o (half angle), corresponding to 0.06π sr $\pm 10\%$ solid angle. The diameter of the focused beam is estimated to be $2w_0 = 1$ μm. Reflected light is collected by the same objective, and the polarization is analyzed. The spectrum is resolved using Fourier transform infrared spectroscopy (BioRad FTS-6000) with an external InAs photodiode. The spectral resolution was 15 cm^{-1}, corresponding to about 10^{-3} relative resolution. For calibration, spectra are normalized to the reflectance spectra of a gold mirror.

Figure 2.2(a) shows the band structure calculated using a plane wave expansion method [91] and reflectivity measured along the $\Gamma M'$ direction (black solid). The broad lowest-frequency measured reflectivity peak between 4700 and 7300 cm^{-1} agrees well with the calculated stop gap. This reflectivity peak is caused by simple Bragg diffraction on the lattice planes indicated in the cartoon at the top of the figure, corresponding to the white lattice planes in Fig. 2.1(a). One can also approximate the lowest-frequency simple Bragg diffraction condition from the dispersion with a constant effective refractive index (n_{eff}), obtained from the low-frequency limit [34]. This estimation is marked by the dashed vertical line and agrees well with the center of the calculated stop gap. The two measured peaks between 9800 and 11100 cm^{-1} agree well with a higher-frequency stop gap marked by a second orange area, caused by multiple Bragg diffraction. The peaks appear at a higher frequency than simple Bragg diffraction, as expected.

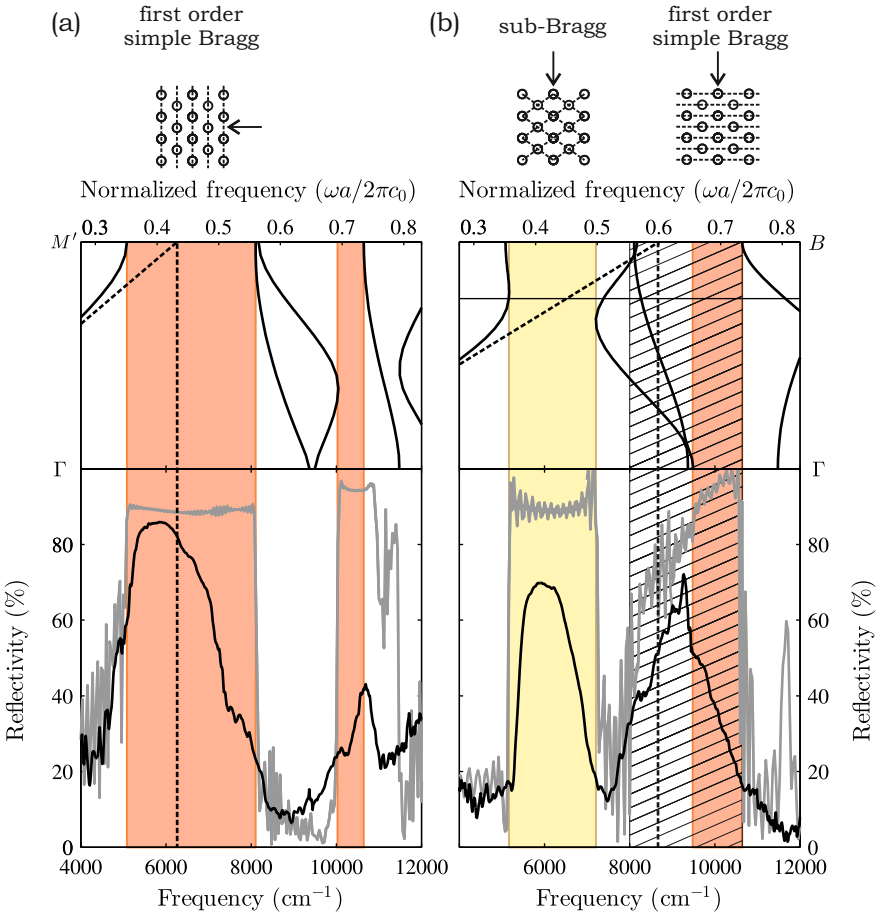

Figure 2.2. Observed diffraction peaks on 2D photonic crystals along high-symmetry directions. Measured (black) and simulated (gray) reflectivity spectra, and calculated band structures for TE-polarized light of a 2D photonic crystal along directions of high symmetry. (*a*) The measured and simulated lowest-frequency diffraction peaks in the $\Gamma M'$ direction match a calculated stop gap that occurs at the simple Bragg-diffraction condition. (*b*) The measured and simulated lowest-frequency diffraction peaks in the ΓK direction match a calculated stop gap and is caused by multiple Bragg diffraction that occurs at a lower frequency than simple Bragg diffraction.

The reflectivity of an incident plane wave on a finite size structure has been simulated with finite difference time domain (FDTD) simulations (gray) [92]. The agreement between the simulated and measured reflectivity is gratifying.

In Fig. 2.2(*b*) we show the calculated band structure and measured reflectivity along the ΓB direction, where K is located on the edge of the Brillouin zone and B is located on the Bragg-plane between Γ and reciprocal lattice vector G_{11}. Two

significant broad measured reflectivity peaks are visible. The lowest-frequency peak between 5400 and 6900 cm^{-1} agrees well with a calculated stop gap marked by the yellow area. This peak is caused by multiple Bragg diffraction on the lattice planes indicated in the cartoon above the calculated stop gap, and is part of the two-dimensional band gap for TE-polarized light. The second reflectivity peak between 8100 and 10000 cm^{-1} agrees with a second calculated stop gap (orange area). The flat bands in the dispersion relation give an impedance mismatch for coupling light into the crystal [6, 36], which likely broadens the observed peak (hatched area). This is supported by FDTD simulations of the reflectivity of incident plane waves on a finite size structure (gray). The agreement between the simulated and measured reflectivity peak is gratifying. The measured peak is probably rounded-off as a result of the high-NA microscope objective. Note that band structure calculations and FDTD simulations neglect the dispersion of silicon. Scattering from surface imperfections becomes more important at higher frequencies, which could explain why the measured reflectivity peak is much lower near 10000 cm^{-1}. At any rate, the frequency ranges of the measured and simulated peaks agree very well.

This second stop gap is caused by simple Bragg diffraction on the lattice planes indicated in the cartoon above the calculated stop gap, corresponding to the red lattice planes in Fig. 2.1(a). The frequency of the simple Bragg diffraction condition based on an n_{eff} is inaccurate because a broad stop gap is already present at lower frequencies. The observation of a prominent diffraction peak caused by multiple Bragg diffraction at a much lower frequency than simple Bragg diffraction is our main observation. This result shows that even for high-symmetry directions such as the ΓK direction, there can be a diffraction condition below simple Bragg diffraction, which we address as *sub-Bragg* diffraction.[2]

We have performed reflectivity measurements on photonic crystals with a range of r/a. Figure 2.3 shows the width of the diffraction peaks for the $\Gamma M'$ (a) and ΓK directions (b). The areas correspond with calculated stop gaps, such as in Fig. 2.2. The dashed line is the approximated frequency of lowest-frequency simple Bragg diffraction assuming a constant n_{eff}. Note the very good agreement between the measured frequencies of the diffraction peaks and the calculated stop gaps. We observe for the ΓK direction that diffraction always appears at a lower frequency than simple Bragg diffraction. This observation confirms the robustness of sub-Bragg diffraction.

2.3. Origin and occurrence of sub-Bragg diffraction

The existence of sub-Bragg diffraction can be explained by considering the lattice in reciprocal space, see Fig. 2.1(b). For the ΓK direction we observe in reciprocal space two points of high symmetry: K and B. K is located on the Brillouin zone boundary, at the intersection of two Bragg planes corresponding to the

[2] The general behavior identified here for 2D and 3D crystals should not be confused with *sub-Bragg reflection* described for 1D Bragg gratings with multiple periodicities [A.A. Spikhal'skii, Opt. Commun. **57**, 84 (1986)]. The latter considers *higher-frequency* (lower-wavelength) diffraction, in contrast to our *lower-frequency* gaps.

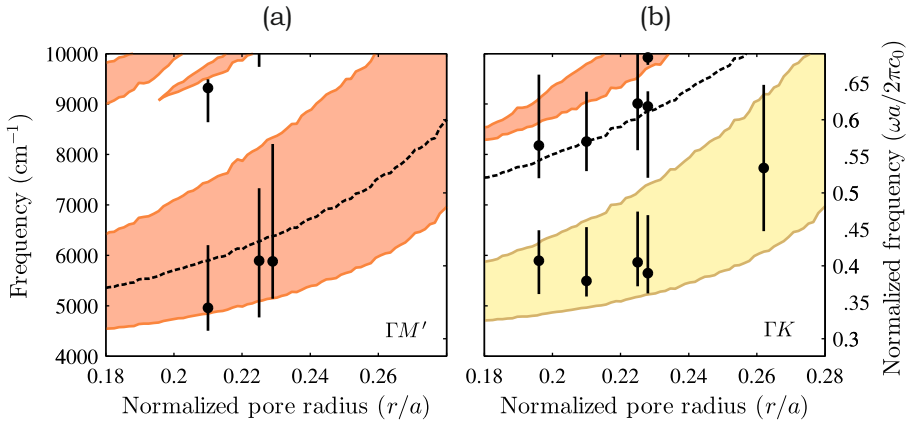

Figure 2.3. Observed diffraction peaks for 2D photonic crystals with different normalized pore radius. Determined normalized width of the diffraction peaks (bars) and frequency of the maximum reflectivity (circles) for different r/a. The filled areas are calculated stop gaps, color-coded as in Fig. 2.2. (a) Normalized frequency of the diffraction peaks for the $\Gamma M'$ direction. (b) Normalized frequency of the diffraction peaks for the ΓK direction.

von Laue conditions between Γ and G_{10}, Γ and G_{11}. Thus at K we have a multiple Bragg diffraction condition on both Bragg planes. B is located at the Bragg plane (dashed line) that satisfies the von Laue condition between $\Gamma = G_{00}$ and G_{11} resulting in simple Bragg diffraction. Since B is located outside the Brillouin zone, the simple Bragg condition occurs at higher frequency than the sub-Bragg condition. From this figure we derive three conditions for sub-Bragg diffraction: *(i)*. The diffraction condition corresponds to a point on a corner edge of the Brillouin zone, giving rise to multiple Bragg diffraction. *(ii)*. The incident wave vector should be along a high symmetry direction, which is satisfied by considering only reciprocal lattice vectors G_{khl}, for which $|h|, |k|, |l| \leq 1$ or equivalent. *(iii)*. Multiple Bragg diffraction has to occur at a lower frequency than the simple Bragg diffraction condition.

Using these three conditions, it becomes evident that diffraction conditions for M and M' correspond to simple Bragg diffraction for G_{10} and $G_{1\bar{1}}$ respectively. K' satisfies criteria *(i)* and *(iii)*, however, it does not satisfy criterion *(ii)*. This diffraction condition belongs to multiple Bragg diffraction in a direction of lower symmetry, similar to the observation in Ref. [38]. Therefore, sub-Bragg diffraction is only observed at K. In this case we have measured the reflectivity of photonic crystals that strongly interact with light. For our crystals, we find that for $r/a > 0.07$ a stop gap opens at K, and for $r/a \leq 0.07$ flat dispersion bands appear.

Up to now we have considered a centered rectangular lattice with long side a, short side c, and $a/c = \sqrt{2}$. However, sub-Bragg diffraction can be expected

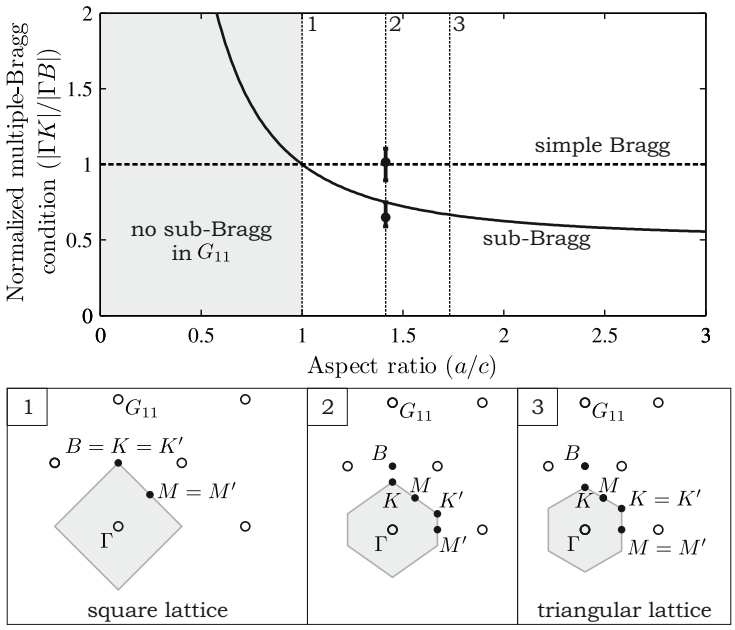

Figure 2.4. Sub-Bragg diffraction in different 2D Bravais lattices described by a centered rectangular unit cell. Normalized sub-Bragg diffraction condition (solid) and normalized simple Bragg diffraction condition (dashed) as a function of a/c. The symbols mark the reflectivity peaks of Fig. 2.2(b), assuming identical n_{eff} for both diffraction conditions. Sub-Bragg diffraction is satisfied for $a/c > 1$. Labels $1, 2, 3$ refer to r/a shown in the panels (bottom). Panel 1 shows the reciprocal lattice (circles) for $a/c = 1$, giving a square lattice and no sub-Bragg diffraction. Panel 2 shows the reciprocal lattice for $a/c = \sqrt{2}$, resulting in sub-Bragg diffraction at K. Panel 3 shows the reciprocal lattice for $a/c = \sqrt{3}$, resulting in sub-Bragg diffraction at K and K'.

for any $a/c > 1$.[3]. To illustrate this point we have made an analytical model to explain the sub-Bragg diffraction frequency. We calculate $|\Gamma K|$ and $|\Gamma B|$ as a function of a/c, where the frequency of the sub-Bragg condition is proportional to $(c_0/n_{\text{eff}})|\Gamma K|$ and the frequency of the simple Bragg condition is proportional to $(c_0/n_{\text{eff}})|\Gamma B|$, where c_0 is the vacuum velocity. The results are shown in Fig. 2.4. When $a/c \to \infty$, sub-Bragg diffraction occurs at $|\Gamma K|/|\Gamma B| = 1/2$. Panel 1 shows the reciprocal lattice for $a/c = 1$, corresponding to the square lattice. In this case $|\Gamma K| = |\Gamma B|$ and therefore sub-Bragg diffraction and simple Bragg diffraction occur at the same frequency, violating condition *(iii)*. Panel 2 shows the reciprocal lattice for $a/c = \sqrt{2}$, corresponding to the experimental

[3] When $a/c < 1$, sub-Bragg diffraction occurs in the direction perpendicular to the ΓK direction for $a/c > 1$. For $a/c < 1$ it is again a centered rectangular lattice with a 90^0 rotated unit cell compared to $a/c > 1$.

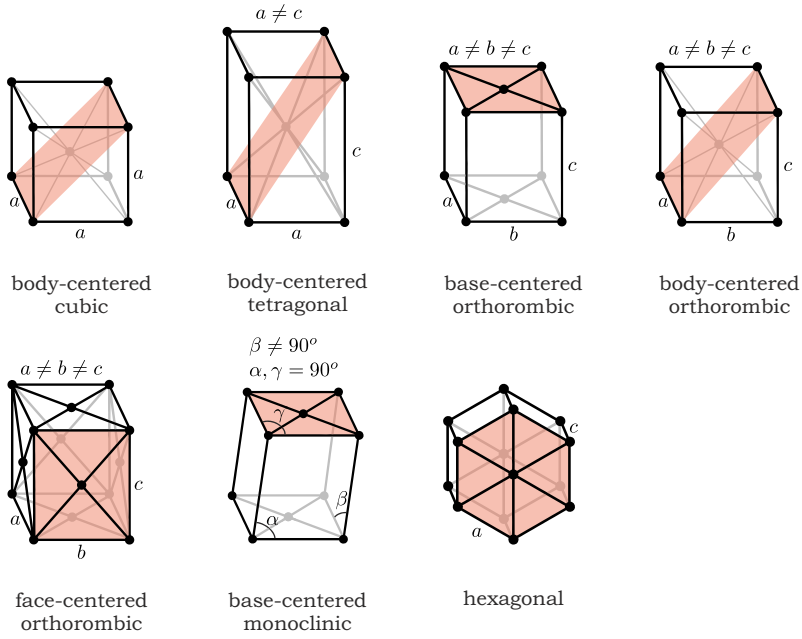

Figure 2.5. 3D Bravais lattices that support sub-Bragg diffraction. The orange planes mark planar cross sections that can be described by a centered rectangular lattice, which is required for sub-Bragg diffraction to occur.

conditions of the structures investigated by us. Panel 3 shows the reciprocal lattice for $a/c = \sqrt{3}$, corresponding to the triangular lattice. All three conditions for sub-Bragg diffraction at K are fulfilled. There is also a sub-Bragg diffraction condition for K'. It may seem that condition (ii) is violated because the $\Gamma K'$ direction corresponds to $G_{2\bar{1}}$. However, because of the rotational symmetry of the Brillouin zone, $K = K'$ and the diffraction conditions in the $G_{2\bar{1}}$ direction are identical to the G_{11} direction, and therefore condition (ii) is satisfied. In a similar experiment performed by Ref. [93] a diffraction peak was observed at K. However, these excellent experiments were compared with band structures between ΓK, since it was not recognized that there is also a diffraction condition at B. For the centered rectangular lattice, one must calculate band structures in the extended range ΓB to get accurately estimate the width of the stop gaps. This is evident from the band structures in Fig. 2.2(b) by comparing the width of the stop gaps when one would consider only ΓK instead of ΓB.

In the case of three-dimensional (3D) crystals, if a Bravais lattice has a planar cross-section that can be described by a centered rectangular lattice along a direction of high symmetry, sub-Bragg diffraction will occur. For 2D Bravais lattices sub-Bragg diffraction can occur for 2 out of 5 Bravais lattices; centered

rectangular and triangular (which is a special case of centered rectangular), see Fig. 2.4. There are 7 out of 14 3D Bravais lattices that have a planar cross-section that can be described by a centered rectangular lattice in a direction of high symmetry; body-centered cubic, body-centered tetragonal, base-centered orthorhombic, body-centered orthorhombic, face-centered orthorhombic, base-centered monoclinic and hexagonal. We predict that sub-Bragg diffraction can occur for these 7 Bravais lattices, which are illustrated in Fig. 2.5.

Sub-Bragg diffraction holds for any kind of wave-propagation in structures that fulfill the symmetry conditions. Therefore we predict that for X-ray diffraction on crystals a sub-Bragg diffraction peak can be observed. As multiple Bragg diffraction is required for photonic band gap formation, hence sub-Bragg diffraction can affect band gap formation [39]. Indeed, the sub-Bragg diffraction condition is part of the 2D TE-band gap in triangular lattices [6]. For elastic wave diffraction a propagation gap is formed at the sub-Bragg condition and therefore also for phonons and for relativistic electrons, such as the case of graphene, which has a triangular lattice.

2.4. Retrospective

Our work was highlighted by Cho in "Breaking the law or bending the terminology?" on ScienceNow (2012). Unfortunately this text suggests that sub-Bragg diffraction might be a new terminology for an already understood physical phenomenon. At the date of writing this dissertation, we have found no prior claims of multiple Bragg diffraction in a direction of high-symmetry below the simple Bragg condition, even after discussing with numerous eminent scientists. We strongly believe in the originality of our work, and I am proud to be co-inventor of the description of this phenomenon.

CHAPTER 3

Signature of a three-dimensional photonic band gap observed on silicon inverse woodpile photonic crystals

We have studied the reflectivity of CMOS-compatible three-dimensional silicon inverse woodpile photonic crystals at near-infrared frequencies. Polarization-resolved reflectivity spectra were obtained from two orthogonal crystal surfaces using an objective with a high numerical aperture. The spectra reveal broad peaks with maximum reflectivity of 67% that are independent of the spatial position on the crystals. The spectrally overlapping reflectivity peaks for all directions and polarizations form the signature of a broad photonic band gap with a relative bandwidth up to 16%. This signature is supported by stop gaps in plane wave band structure calculations and agrees with the frequency region of the expected band gap.

3.1. Introduction

Currently, many efforts are devoted to create an intricate class of three-dimensional meta-materials known as photonic crystals that radically control propagation and emission of light [4, 5, 10, 94–102]. Photonic crystals are ordered composite materials with a spatially varying dielectric constant that has a periodicity of the order of the wavelength of light [6]. As a result of the long-range periodic order, the photon dispersion relations are organized in bands, analogous to electron bands in solids [28]. Frequency ranges called stop gaps emerge in which light is forbidden to propagate in particular directions due to Bragg interference [34]. In specific three-dimensional crystals, a common stop gap is formed for all polarizations and directions, called the photonic band gap. Light cannot propagate inside the photonic band gap, allowing for ultimate control of light emission. Emission rates and directions can be manipulated [95, 97, 98, 102], which could lead to efficient micro-scale light sources [102, 103] and solar cells [104]. Additional interest is aroused by the possibility of Anderson localization of light by point defects added to photonic band gap crystals [5].

It is an outstanding challenge to experimentally demonstrate a photonic band gap; inside the photonic band gap the density of optical states equals zero. The density of states can be investigated with light emitters placed inside the crystal,

The content of this chapter has been published as: S.R. Huisman, R.V. Nair, L.A. Woldering, M.D. Leistikow, A.P. Mosk, and W.L. Vos, Phys. Rev. B **83**, 205313 (2011).

see, *e.g.*, Refs. [95, 97, 98]. These experiments are difficult to perform and to interpret, and are not always possible due to the limited availability of appropriate light sources and detection methods. However, one can obtain an indication of the band gap by observing a stop band in a directional experiment, such as a peak in reflectivity or a trough in transmission [105–110]. The frequency width of an experimentally observed stop band often corresponds to a stop gap in the dispersion relation, where light is forbidden to propagate. Interestingly however, a peak in reflectivity or a trough in transmission also occurs when an incident wave cannot couple to a field mode in the crystal [6, 36, 111]. Therefore, one typically compares observed stop bands with theory such as calculated band structures to indicate the presence of a band gap. Unfortunately, most theory is typically valid for ideal structures, for instance of infinite size. More compelling evidence of a photonic band gap could be obtained if one demonstrates that stop bands have a common overlap range independent of the measurement direction, since light is forbidden to propagate in a photonic band gap. Angle-resolved [39, 100, 107] and angle-averaged spectra [110] have been collected. However, due to experimental considerations it appears to be extremely difficult to measure over 4π sr solid angle. Stopbands are typically investigated on only one surface of the photonic crystal, and only few studies have investigated multiple surfaces, see, *e.g.*, Refs. [108, 112]. In addition, one needs to rule out spurious boundary effects by confirming that stop bands reproduce at different locations on the crystal, requiring position-dependent experiments. Furthermore, it can occur that field modes in the crystal can only couple to a specific polarization [41]. Polarization-resolved experiments are required to demonstrate that stop bands are present for all polarizations [113]. Therefore, a strong experimental signature for a photonic band gap is obtained if one can demonstrate that stop bands are position-independent and overlap for different directions and orthogonal polarizations. To the best of our knowledge, such a detailed analysis of stop bands for three-dimensional photonic band gap crystals has not yet been reported.

In this chapter we study silicon three-dimensional inverse woodpile photonic crystals [44, 114]. The inverse woodpile photonic crystal is a very interesting nanophotonic structure on account of its broad theoretical photonic band gap with more than 25% relative gap width. Schilling *et al.* were the first to investigate stop bands in inverse woodpile crystals [110]. They measured unpolarized reflectivity along one crystal direction using an objective with numerical aperture NA = 0.57. An indication for the photonic band gap was found by a stop band that agreed with the calculated band structure. Other groups have fabricated inverse woodpile photonic crystals of different materials using several methods, and also performed reflectivity measurements along one direction with unpolarized light [100, 115–120], resulting in similar indications of the band gap. Here, we present an extensive set of polarization-resolved reflectivity spectra of silicon inverse woodpile photonic crystals. We have collected spectra from two orthogonal crystal surfaces using an objective with a high numerical aperture NA = 0.65. The reflectivity spectra were obtained on different locations on the photonic crystal surfaces to confirm the reproducibility, to determine the optical size of the crystals, and to investigate boundary effects. We demonstrate position-

independent overlapping stop bands for orthogonal polarizations and crystal directions, which is a signature of a three-dimensional photonic band gap. This signature agrees with calculated stop gaps in plane wave band structure calculations and with the frequency region of the expected band gap.

3.2. Inverse woodpile photonic band gap crystals

Figure 3.1(a) illustrates the orthorhombic unit cell of an inverse woodpile photonic crystal (left), together with a crystal consisting of eight unit cells (right). The structure can be described by two identical sets of pores with radius r running in two orthogonal sides of a box, where each set represents a centered rectangular lattice with sides a and c. If the ratio a/c equals $\sqrt{2}$, the crystal symmetry is cubic and the crystal structure is diamond-like, see Refs. [44, 114, 121]. This type of inverse woodpile photonic crystals with $a/c = \sqrt{2}$ has a maximum band gap width of 25.4% for $r/a = 0.245$. The sets of pores are oriented perpendicular to each other and the centers of one set of pores are aligned exactly between columns of pores of the other set, resulting in the structure of Fig. 3.1(a). In Fig. 3.1(a) a coordinate system is introduced that is used in this chapter.

We have fabricated multiple inverse woodpile photonic crystals with different pore radii in monocrystalline silicon with a CMOS compatible method, as is described in detail in Refs. [122, 123]. Figure 3.1(b) shows a scanning electron microscope (SEM) image of one of these crystals from the same perspective as in Fig. 3.1(a). This crystal consists of more than 10^3 unit cells and is located on top of bulk silicon. The crystal is surrounded by a macroporous two-dimensional photonic crystal that forms the first set of pores used to fabricate inverse woodpile photonic crystals. A second set of pores is oriented perpendicular to this two-dimensional crystal to form the inverse woodpile photonic crystal. A part of the boundary of the inverse woodpile photonic crystal is marked with the red dashed line. The inverse woodpile photonic crystal has lattice parameters $a = 693 \pm 10$ nm, $c = 488 \pm 11$ nm, and a pore radius of $r = 145 \pm 9$ nm in both directions.[1] Typically eight different inverse woodpile photonic crystals are made on one two-dimensional photonic crystal that each extend over approximately 7 μm $\times$ 5 μm $\times$ 5 μm in size. Figure 3.1(c) shows a SEM image of a crystal viewed parallel with the second set of pores or parallel with the ΓX direction. In Ref. [122] it has been determined that the second set of pores are precisely centered to within $\Delta y = 17 \pm 12$ nm between columns of pores of the first etch direction, which is extremely close to the ideal structure of Fig. 3.1(a). One unit cell is marked in the right bottom corner of Fig. 3.1(c). Here, we describe an extensive set of reflectivity measurements collected from this inverse woodpile photonic crystal centered along the ΓX and ΓZ direction, which is representative for more than five other crystals that we have studied.

Figure 3.2 shows the band structure for light in a silicon inverse woodpile photonic crystal with $r/a = 0.190$ and $\epsilon_{\mathrm{si}} = 12.1$ for the irreducible Brillouin zone

[1] These parameters do not include possible calibration errors of the scanning electron microscope.

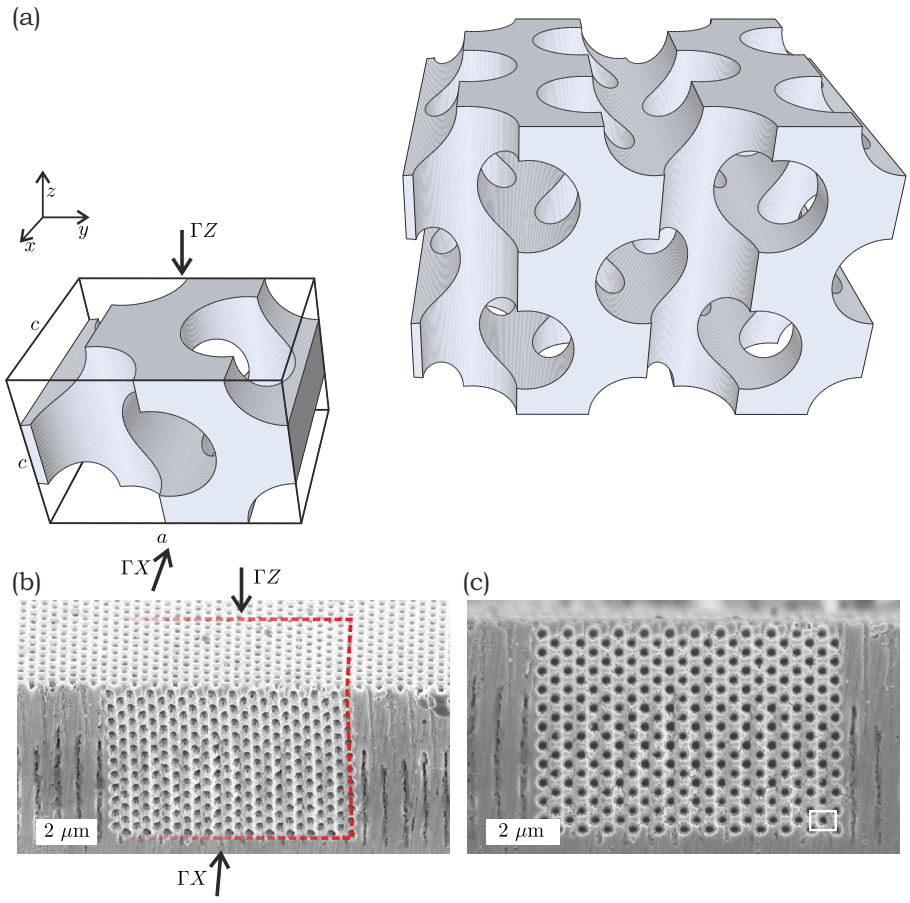

Figure 3.1. Structure of inverse woodpile photonic crystals. (*a*) Schematic representation of the orthorhombic unit cell of a cubic inverse woodpile photonic crystal (left) and a crystal consisting of eight unit cells (right). The structure can be described by two identical sets of pores running in two orthogonal sides of a box. (*b*) Scanning electron microscope image of a cubic inverse woodpile crystal with $a = 693 \pm 10$ nm, $c = 488 \pm 11$ nm ($a/c = \sqrt{2}$) and $r = 145 \pm 9$ nm, surrounded by a macroporous two-dimensional crystal. The dashed red line indicates a part of the boundary of the inverse woodpile photonic crystal. (*c*) Scanning electron microscope image viewed from the ΓX direction. The rectangle represents one face of the orthorhombic unit cell, compare with (*a*).

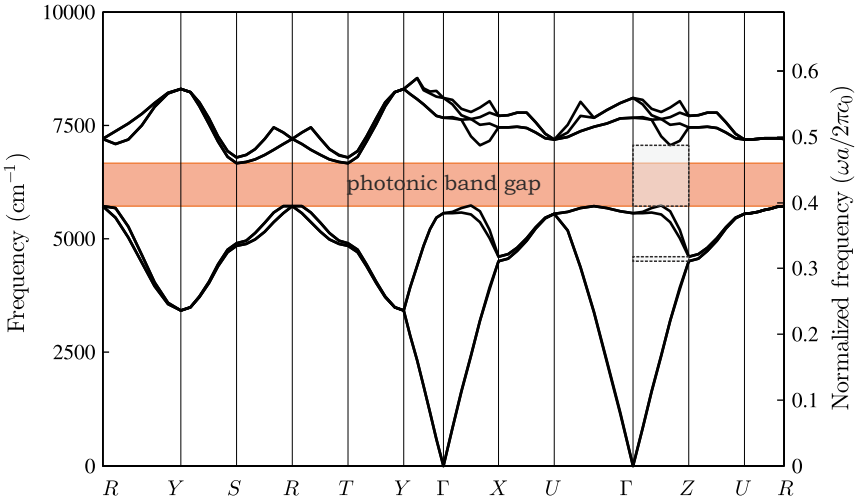

Figure 3.2. Band structure of an inverse woodpile photonic crystal. The dispersion relation for the eight lowest frequency Bloch modes are calculated for a structure with $a = 690$ nm, $c = 488$ nm and pore radius $r = 131$ nm ($r/a = 0.190$). The left axis represents the absolute frequency in cm^{-1}, the right axis shows the normalized frequency. The orange bar marks a photonic band gap with a relative gap width of $\Delta\omega/\omega_c = 15.1\%$. The gray bars mark stop gaps in the ΓZ direction.

of a simple orthorhombic lattice, calculated with the method of Ref. [91]. This band structure appears to be representative for the crystal of Fig 3.1(a). Between normalized frequency $\omega a/2\pi c_0 = 0.395$ (5727 cm^{-1}) and $\omega a/2\pi c_0 = 0.460$ (6668 cm^{-1}) a broad photonic band gap appears with 15.1% relative width. The band structure in both the ΓX and ΓZ direction is identical and shows two stop gaps, marked by the gray rectangles in the ΓZ direction. The lowest frequency stop gap between $\omega a/2\pi c_0 = 0.310$ (4505 cm^{-1}) and $\omega a/2\pi c_0 = 0.318$ (4611 cm^{-1}) is narrow and it is closed when going in the ZU direction. The broad second stop gap between normalized frequency $\omega a/2\pi c_0 = 0.395$ (5727 cm^{-1}) and $\omega a/2\pi c_0 = 0.488$ (7062 cm^{-1}) is part of the photonic band gap. The low frequency edge of the photonic band gap is bounded along the ΓX and ΓZ direction, which we access in our experiment. The high frequency edge of the band gap occurs at the S and T points, which are not accessible in our experiment. Deviations in the crystal geometry affect the dispersion relation and therefore the band gap [114, 121]. The band gap of this kind of structure is robust to most types of deviations, whose tolerances are well within reach of our fabrication methods [121].

3.3. Experimental setup

A supercontinuum white light source (Fianium SC-450-2) with a frequency range of 4000 to 22000 cm^{-1} is used to illuminate the photonic crystals. Light is polarized and focused on the crystal using a gold-coated reflecting objective to avoid dispersion (Ealing X74). The numerical aperture NA=0.65 of the objective results in a spectrum angle-averaged over approximately 0.44π sr $\pm 10\%$ solid angle in air. The diameter of the focused beam is estimated to be $2w_0 \approx 1$ μm from experiments on micropillars [124]. Reflectivity is measured for a broad range of wave vectors that are centered on the ΓX and ΓZ directions, which is expected to result in similar stop bands because of the symmetry of the crystal. Reflected light is collected by the same objective, and the polarization is analyzed. The spectrum is resolved using Fourier transform infrared spectroscopy (BioRad FTS-6000) in combination with an external InAs photodiode. The reflectivity of the crystals is collected between 4000 and 10000 cm^{-1} with a resolution of 32 cm^{-1}. The reflectivity spectra are normalized to the reflectance spectra of a gold mirror, which were collected before and after measuring on a crystal. The individual gold spectra show only minor differences due to the excellent stability of the setup, except between 9200 and 9600 cm^{-1}, close to the master frequency of the white light source, which is thus excluded. The reflectivity is measured for two orthogonal polarizations, where the orientation of the set of pores perpendicular to the measurement direction is used as reference; light is $\perp$-polarized when the electric field is perpendicular to the direction of this set, light is $\parallel$-polarized when it is parallel with the direction of this set. For example, when the reflectivity is measured centered on the ΓX direction (see Fig. 3.1(a)), light is $\parallel$-polarized when the electric field is parallel with the ΓZ direction. The samples are placed on a three-dimensional x-y-z-translation stage (precision ± 50 nm) to study the position-dependence of the reflectivity.

3.4. Experimental results

Position-dependent reflectivity experiments have been performed by scanning the photonic crystal through the focal spot. These scans were performed on two orthogonal surfaces of the crystal allowing for measurements along the ΓX and ΓZ direction, see Fig. 3.1(b). These scans provide insight in the reproducibility of the reflectivity, the optical size of the crystal, and boundary effects. We will first describe one specific scan for the reflectivity obtained, centered on the ΓX direction for $\perp$-polarized light. Next we will compare reflectivity spectra obtained from different scans to demonstrate position-independent overlapping stop bands for orthogonal polarizations and crystal directions that are the signature for the photonic band gap.

3.4.1. Position-dependent reflectivity.

Figure 3.3 shows the position-dependent reflectivity along the ΓX direction for $\perp$-polarized light, where the focal spot was moved in the y direction. Figure 3.3(a)

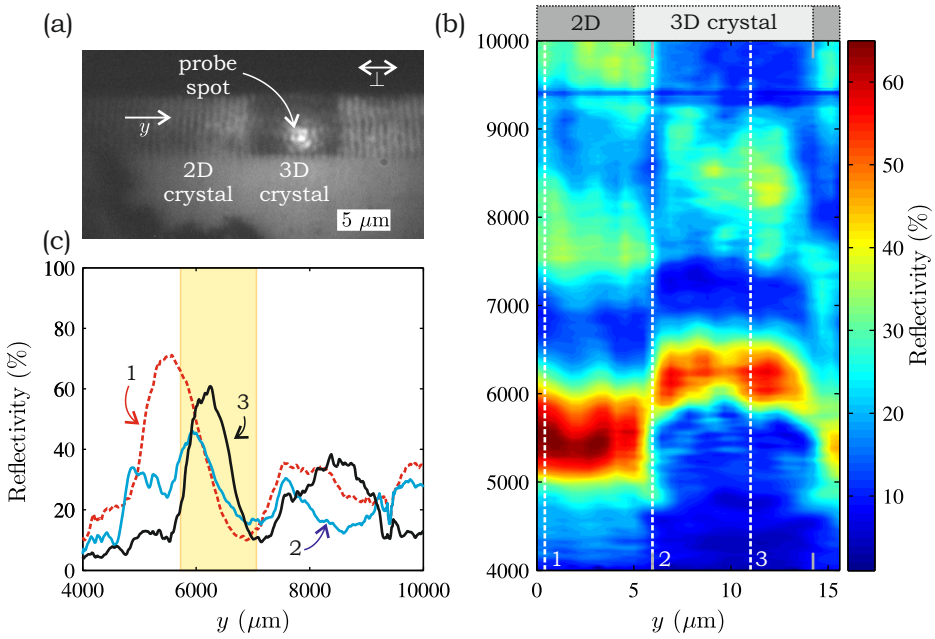

Figure 3.3. Position- and frequency-resolved reflectivity for an inverse woodpile photonic crystal. The reflectivity was measured parallel with the ΓX direction for $\perp$-polarized light. (*a*) Microscope picture of the crystal placed in the setup. The bright spot near the center of the crystal is reflected focussed light of the supercontinuum white light source. The spot was moved over the crystal surface along the y direction. (*b*) Reflectivity collected as a function of the y-position of the spot on the photonic crystal surface. The scan started on the surrounding two-dimensional crystal ($y = 0$ μm), continued over the inverse woodpile photonic crystal ($6 < y < 14$ μm) and ended on the two-dimensional crystal. The spot was moved in steps of 0.46 ± 0.05 μm. The gray lines on the horizontal axis indicate the boundaries of the crystal. The white dashed lines indicate positions for representative spectra displayed in (*c*). (*c*) Reflectivity spectra measured at the y-coordinates given by the white dashed lines in (*b*). The calculated stop gap in the ΓX direction for $r/a = 0.19$ is marked by the yellow bar.

shows an optical microscope image of the inverse woodpile photonic crystal (dark square in the middle) taken during the reflectivity scan, viewed along the same perspective as Fig. 3.1(c). The bright spot centered on the inverse woodpile photonic crystal is the focal spot of the supercontinuum white light source. The scan was started with the focal spot on the surrounding two-dimensional crystal to the left of the inverse woodpile photonic crystal, continued over the inverse woodpile photonic crystal, and finished on the two-dimensional crystal to right of the inverse woodpile photonic crystal. Figure 3.3(b) shows a contour-plot of the measured reflectivity as a function of position, Fig. 3.3(c) shows three cross-sections of the contour-plot of Fig. 3.3(b).

In Fig. 3.3(b) a broad reflectivity peak is observed for the inverse woodpile photonic crystal ($6 < y < 14$ μm) between 5600 and 6900 cm^{-1} with a high reflectivity of 60%. The spectrum taken at $y = 11$ μm is shown in Fig. 3.3(c). This distinct peak is observed in the same frequency range over the entire three-dimensional crystal surface. The stop band corresponds to the stop gap in the ΓX direction, which is marked by the yellow bar in Fig. 3.3(c), and which is part of the photonic band gap.

The maximum reflectivity is about 67% for our inverse woodpile photonic crystals, which is likely limited by surface roughness that scatters light in directions that are not collected by the objective. This assertion is supported by the observation of lower reflectivity on crystal surfaces that were less well polished. The finite thickness of the crystals could also lead to some reduction of the reflectivity. From the full width at half maximum of the peak, we derive a Bragg length equal to approximately $7d$, with d the spacing between lattice planes [9]. Therefore, we conclude that our crystals have a thickness of approximately 1.5 times the Bragg length. This corresponds to a maximum reflectivity of $1 - e^{-1.5} = 78\%$. Since the observed maximum reflectivity is consistent with surface roughness and finite size effects, it is reasonable that the crystal has a high reflectivity through all of the 0.44π sr probed solid angle. As is seen in the band structures in Fig. 3.2, the stop gap hardly shifts in frequency for different directions in the Brillouin zone, hence it is even more likely that the obtained angle-averaged reflectivity is representative for the full probed range.

From the scan in Fig. 3.3(b), we observe a clear distinction between the reflectivity of the three-dimensional inverse woodpile photonic crystal and the surrounding two-dimensional crystal. A reflectivity maximum of 70% is observed on the two-dimensional crystal at $y < 6$ μm and at $y > 14$ μm. The spectrum taken at $y = 0.42$ μm is shown in Fig. 3.3(c). This peak belongs to the ΓK stop gap between 4700 and 6300 cm^{-1} for TE polarized light. At the interfaces between the two-dimensional and inverse woodpile photonic crystal at $y = 6$ and at $y = 14$ μm, a peculiar double peak appears as shown in Fig. 3.3(c), which is only present at the two-dimensional crystal to three-dimensional crystal interface. The spectrum at $y = 6$ μm is shown in Fig. 3.3(c). This double peak consist of one component between approximately 4700 and 5500 cm^{-1}, and a second component between approximately 5500 and 6500 cm^{-1}. This double peak differs from a linear combination of two-dimensional crystal and three-dimensional crystal peaks (see Fig. 3.3(c)) that would be expected naively, since both of its components appear at

lower frequencies than the two-dimensional crystal and three-dimensional crystal peaks. While we have currently no interpretation for this intricate double peak, the observation of interface peaks calls for advanced theoretical interpretations outside the scope of the present chapter. In the long-wavelength limit below 5000 cm^{-1}, both the two-dimensional and inverse woodpile photonic crystals are transparent. As a result, their reflectivities are low. Since the silicon filling fraction is smaller for inverse woodpile photonic crystals than for two-dimensional crystals, they have a lower effective refractive index [125], resulting in a lower long-wavelength reflectivity for inverse woodpile photonic crystals.

By combining this y-scan with six other scans for orthogonal directions, crystal surfaces, and polarizations, we can measure the optical size of the crystal, in other words, the range over which the crystal has the same reflectivity. This is in the x direction approximately 3 μm, in the y direction 7 μm and in the z direction 4 μm. The optical size is smaller in the x direction than in the y direction, which is in agreement with detailed structural information derived in Ref. [122] for inverse woodpile photonic crystals.

3.4.2. Overlapping stop bands for orthogonal polarizations and crystal surfaces.

We have studied the position-dependent reflectivity spectra for two orthogonal crystal surfaces and two orthogonal polarizations, by taking scans similar to the one presented in Fig. 3.3. From these scans we have selected 4 ($= 2 \times 2$) spectra that are reproducible on several locations on the crystal, see Fig. 3.4($a-d$), black curves. Figure 3.4(a) shows the reflectivity centered in the ΓX direction for $\perp$-polarized light, and Fig. 3.4(b) for $\parallel$-polarized light. Figure 3.4(c) shows the reflectivity centered in the ΓZ direction for $\perp$-polarized light, and Fig. 3.4(d) for $\parallel$-polarized light. A broad reflectivity peak appears for both directions and polarizations with maxima up to 67%. The stop bands overlap between 5900 and 6900 cm^{-1} (blue bar), corresponding to a relative bandwidth of 16%. This position-independent overlapping stop band for orthogonal polarizations and crystal directions that are proved over large solid angles is a signature for the photonic band gap with a relative bandwidth up to 16%.

The reflectivity obtained from the ΓX direction is shown in Fig. 3.4($a-b$). Below 5000 cm^{-1}, the reflectivity behaves similarly for $\perp$- and $\parallel$-polarized waves. Based on Fresnel reflection and the filling fraction of this crystal determining the effective refractive index, one would expect a reflectivity of approximately 10%, which is in very good agreement with our observations. A major reflectivity peak is observed for both polarizations; for $\perp$-polarized light (Fig. 3.4(a)) the peak appears between 5800 and 7300 cm^{-1}, for $\parallel$-polarized waves the peak appears between 5300 and 7100 cm^{-1}. At higher frequencies the reflectivity varies around 20%. Reference spectra (gray) were collected on the silicon surface within 5 μm distance from the inverse woodpile photonic crystal. The reflectivity varies between about 20 and 30%, which agrees closely with 31% reflectivity based on Fresnel reflection and a refractive index of $n = 3.5$ for a flat silicon surface. The reference spectra confirm that the observed stop bands in the inverse woodpile

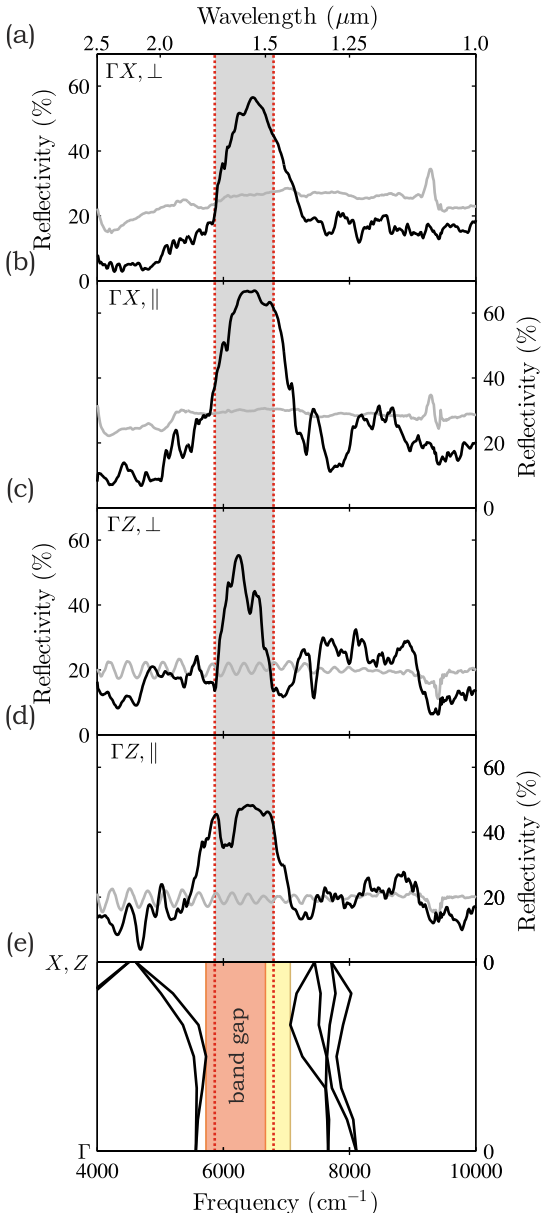

Figure 3.4. Measured reflectivity of an inverse woodpile photonic crystal. $(a-d)$ Measured reflectivity (black lines) along two orthogonal directions (centered on ΓX and ΓZ) and orthogonal polarizations (perpendicular $\perp$ and parallel $\parallel$ to the pores perpendicular to the measurement axes). The overlapping frequencies of the stop bands (gray bar) reveal the presence of a photonic band gap. Reference reflectivity (gray lines) are measured on non-photonic parts of the sample within 5 μm from the photonic crystal. (e) Calculated band structure for both ΓX and ΓZ reveal a stop gap (yellow bar), which is part of the band gap (orange).

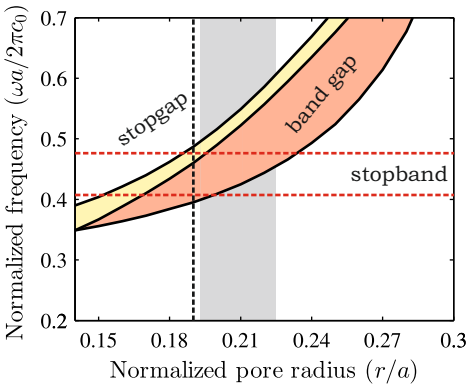

Figure 3.5. Calculated stop gap for the ΓX and ΓZ directions as a function of relative pore radius r/a. The band gap (orange) is part of the broad stop gap (yellow). The gray bar is the value of r/a based on parameters determined from SEM images. The band structures in Fig. 3.2 and 3.4(e) were calculated at $r/a = 0.19$ (vertical dashed line) that agree best with the experiments. The horizontal dashed lines mark the edges of the common stop band determined from Fig. 3.4($a - d$).

photonic crystal are indeed caused by the geometry of the nanostructure.

The reflectivity obtained from the ΓZ direction is shown in Fig. 3.4($c - d$). Below 5000 cm^{-1}, the reflectivity behaves similarly for $\perp$- and $\parallel$-polarized waves. For the ΓZ direction, fringes appear and the average reflectivity is higher than for the ΓX direction. These fringes are Fabry-Pérot interferences caused by internal reflections in the inverse woodpile photonic crystal between the air-crystal boundary and the crystal-silicon boundary. The fringes are also present on the reference spectra (gray) that are collected parallel to the first set of pores that form the surrounding two-dimensional crystal. Above 5000 cm^{-1} a major reflectivity peak is observed for both polarizations near the expected band gap. For $\perp$-polarized light (Fig. 3.4(c)) the peak appears between 5900 and 6900 cm^{-1}, for $\parallel$-polarized waves the peak appears between 5300 and 7200 cm^{-1}. The amplitude of the reflectivity peaks in the ΓZ direction are comparable with the reflectivity peaks of the ΓX direction. For the ΓZ direction, several troughs appear in the spectra, which are likely caused by surface contamination.

If one overlays the spectra for $\perp$-polarized light, compare Fig. 3.4(a, c), it appears that the peaks overlap at the low-frequency side. In addition, for both the ΓX and ΓZ directions, the stop band is broader for $\parallel$-polarized waves than for $\perp$-polarized waves. This is an experimental indication that the pore radii of both sets of pores are identical, as expected from the symmetry of the structure.

3.5. Discussion

In order to interpret our observations, notably of the overlapping stop bands for two orthogonal crystal directions and two orthogonal polarizations, we have performed photonic band structure calculations. In the course of the calculations, we have come to realize that pore radii determined from electron microscopy are an overestimate of the true pore radii by approximately 10 nm. This is reasonable, since parameters determined from electron microscopy have un uncertainty, typically near 2 to 3% [126]. Therefore, we have performed band structure calculations as a function of r/a. Figure 3.5 shows the calculated stop gap in the ΓX and ΓZ direction and the band gap versus r/a. The broad stop gap corresponds to the intense stop bands in our reflectivity spectra. The horizontal dashed lines mark the edges of the overlapping stop band observed in Fig. 3.4. The gray bar is the value of r/a based on parameters determined from SEM images. For a relative pore radius between $r/a = 0.19$ and $r/a = 0.20$, the observed stop band is in agreement with the calculated band gap and stop gap, which is close to the value of r/a based on SEM images. This indicates that the crystal has an r/a between 0.19 and 0.20. The corresponding band structure for $r/a = 0.190$ is shown in Fig. 3.2 and the band structure in the ΓX and ΓZ directions are shown in Fig. 3.4(e). A stop gap is predicted between 5727 and 7061 cm^{-1}, which is part of the calculated band gap between 5727 and 6668 cm^{-1}. The calculated band gap agrees well with the observed signature of the photonic band gap between 5900 and 6900 cm^{-1} (16% relative bandwidth), which thus provides further support for our assertion.

We have performed reflectivity measurements with an objective with NA= 0.65, resulting in a spectrum angle-averaged over 0.44π sr $\pm 10\%$ solid angle in air. We have measured the reflectivity from two orthogonal crystal surfaces and we observe intense peaks. Therefore, as argued above from the high reflectivity and the finite size of the photonic crystals, it is most likely that the observed stop bands extend over 0.88π sr $\pm 10\%$ solid angle. By invoking the symmetry of the crystal, the stop bands centered along the opposite $-\Gamma X$ and $-\Gamma Z$ directions are identical to the ΓX and ΓZ directions. Therefore, our observations would correspond to stop bands up to 1.76π sr $\pm 10\%$ external solid angle of the inverse woodpile photonic crystal, in other words nearly half of all directions. In previous experiments on inverse opals without bandgap [127], nearly half of all directions were found to be excluded for propagation for a vanishingly narrow frequency band. Therefore, the present result is to the best of our knowledge the largest solid angle for which a broad photonic stop band has been reported.

The observed common stop band between 5900 and 6900 cm^{-1} is well explained with band structure calculations. A limitation to our interpretation is that we invoke a theory for infinite crystals. Theoretical calculations of reflectivity for finite crystals could result into new insights in the obtained spectra, for instance how light propagates inside photonic band gap crystals, which is an extremely complex problem as described in Ref. [128]. A well known method for finite crystals are finite-difference time domain simulations [129]. Unfortunately, however, full three-dimensional simulations with reasonable parameters for our

experiments will require very extensive numerical calculations [130] that are outside the scope of our present experimental study. Scattering matrix methods [131, 132] provide a good description of three-dimensional crystals with finite thickness. However, the method assumes that a crystal is infinitely extended in both transverse dimensions which is not the case for our crystals. In future, we expect that discontinuous Galerkin methods may provide in new roads into calculating light propagation in three-dimensional photonic crystals of finite size [133]. Hence we conclude that a theory for three-dimensional finite crystals is currently being called for. It will be even more difficult to implement the experimental boundary conditions into such calculations, such as the shape of the pores and the NA of the microscope objective. At any rate, the agreement between our calculations and our experimental data is gratifying.

For good measure, the observed signature of the photonic band gap is not a complete experimental observation of such a gap. At this time, we can not experimentally exclude that there are crystal directions where the stop bands are either closed or shifted to different frequencies. While we consider these possibilities unlikely based on the theoretical study of our crystals and in view of the measured crystal parameters, a fully experimental observation of a photonic band gap must entail an experimental method where the local density of optical states is probed. An example would be the doping of the crystals with quantum dots [134] and measuring the emission rates [95, 97, 98].

3.6. Conclusions

In conclusion, we have studied the polarization-dependent reflectivity centered on the ΓX and ΓZ direction of three-dimensional silicon inverse woodpile photonic crystals. We have observed a position-independent overlapping stop band for different polarizations and directions, which are supported with calculated band structures. This is the signature of a photonic band gap with a bandwidth of up to 16%.

3.7. Retrospective

Within one year after observing the strong signature of a photonic band gap, we demonstrated the first inhibited spontaneous emission of embedded quantum dots in the same structures, confirming the presence of the photonic band gap [47].

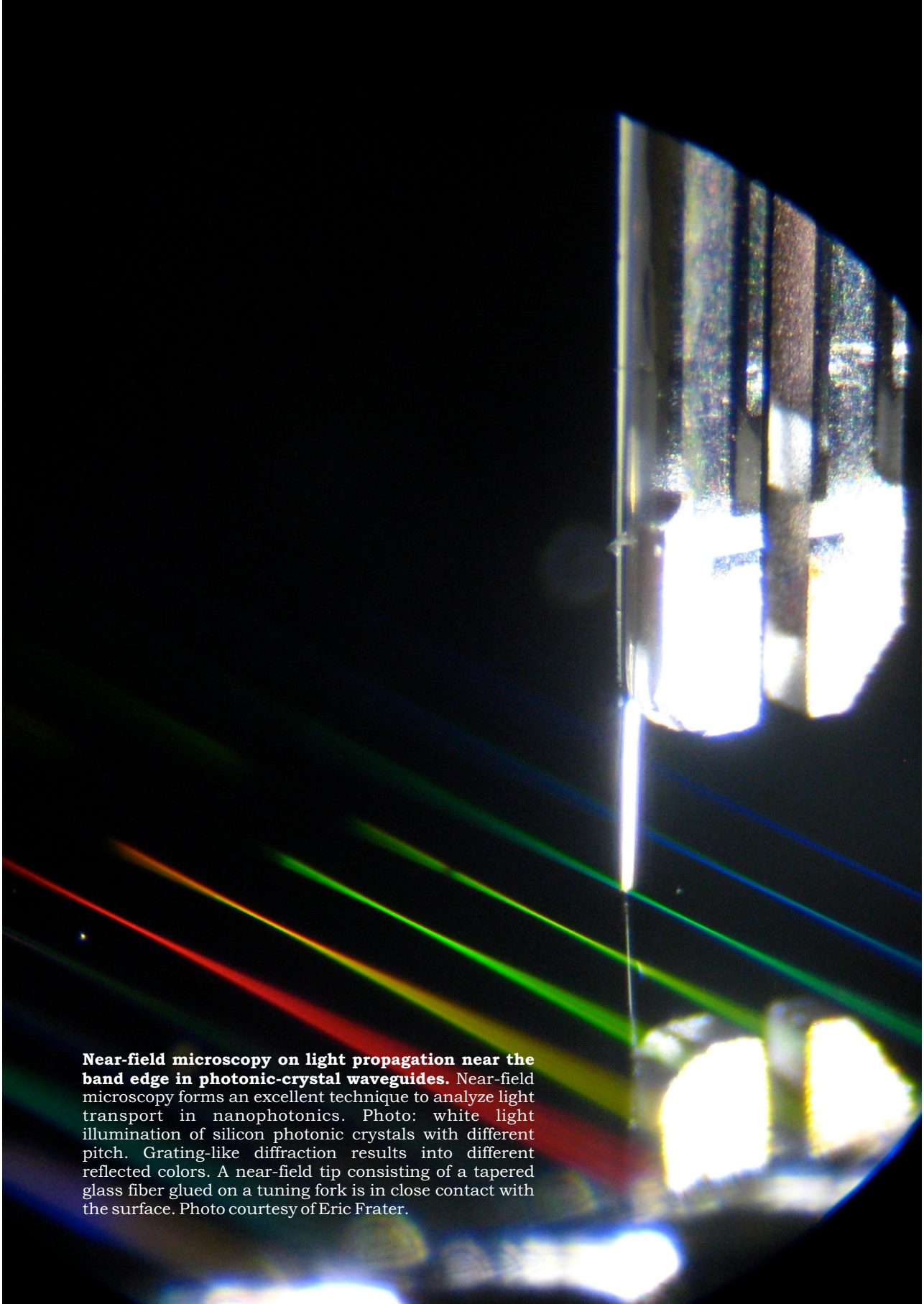

Near-field microscopy on light propagation near the band edge in photonic-crystal waveguides. Near-field microscopy forms an excellent technique to analyze light transport in nanophotonics. Photo: white light illumination of silicon photonic crystals with different pitch. Grating-like diffraction results into different reflected colors. A near-field tip consisting of a tapered glass fiber glued on a tuning fork is in close contact with the surface. Photo courtesy of Eric Frater.

Part II.

Light near the band edge in photonic-crystal waveguides

CHAPTER 4

Extraction of optical Bloch modes in a photonic-crystal waveguide

We perform phase-sensitive near-field scanning optical microscopy on photonic-crystal waveguides. The observed intricate field patterns are analyzed by spatial Fourier transformations, revealing several guided TE- and TM-like modes. Using the reconstruction algorithm proposed by Ha, *et al.* [Opt. Lett. 34 (2009)], we decompose the measured two-dimensional field pattern in a superposition of propagating Bloch modes. This opens new possibilities to study specific modes in near-field measurements. We apply the algorithm to study the transverse behavior of a guided TE-like mode, where the mode extends deeper in the surrounding photonic crystal when the band edge is approached.

4.1. Introduction

Near-field scanning optical microscopy (NSOM) is a powerful tool to study objects with a resolution below the diffraction limit [8]. A unique feature of NSOM is the ability to tap light from structures that are designed to confine light, such as integrated optical waveguides [51, 55] and cavities [57, 58, 135, 136]. Using the effect of frustrated total internal reflection, light that is invisible to other microscopy techniques can be detected. It is mainly for this reason that NSOM is so useful in the study of photonic-crystal waveguides. Photonic-crystal waveguides are two-dimensional (2D) photonic-crystal slabs with a line defect wherein light is guided [6]. They possess unique dispersion relations, supporting slow-light propagation and enhanced light-matter interactions [52, 137].

With NSOM, one can measure the dispersion relation in these waveguides, map light pulses spatially, and study slow-light propagation [51, 56, 138]. It is also possible to measure the field patterns, which can be complicated because of the multimodal nature of the structures. Spatial Fourier transforms are especially useful to analyze, *e.g.*, the dispersion [51] or individual mode contributions [139]. For light propagation in photonic-crystal waveguides the detected field pattern is a superposition of Bloch modes determined by the symmetry of the waveguide. Ha *et al.* [140] recently proposed an algorithm that uses these symmetry conditions to extract Bloch modes from arbitrary measured field patterns [141].

The content of this chapter has been published as: S.R. Huisman, G. Ctistis, S. Stobbe, J.L. Herek, P. Lodahl, W.L. Vos, and P.W.H. Pinkse, J. Appl. Phys. **111**, 033108 (2012).

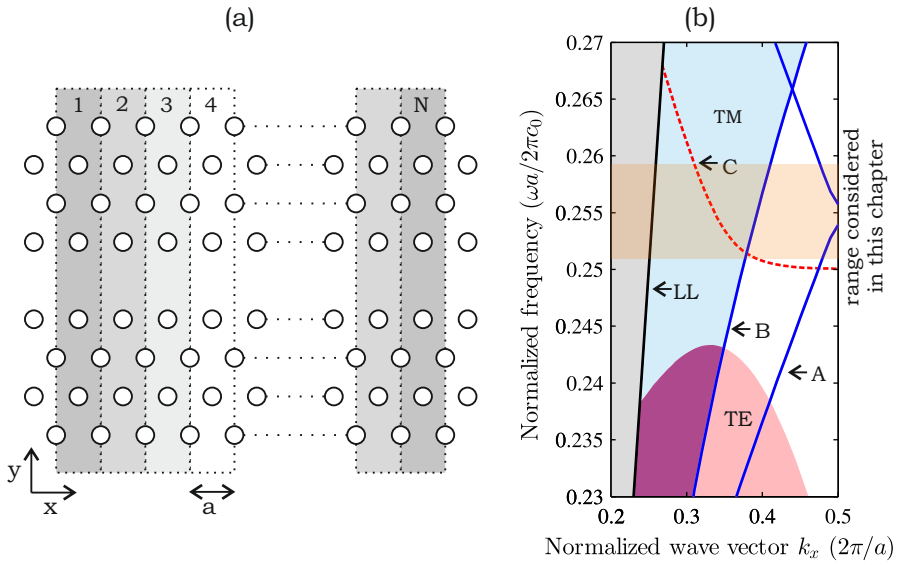

Figure 4.1. Light transport in photonic-crystal waveguides. (*a*) Schematic top view of a photonic-crystal waveguide that is divided in N unit cells (rectangles) for the reconstruction algorithm. (*b*) Calculated band structure for a GaAs photonic-crystal waveguide showing both TE-like (red curve) and TM-like (blue curves) guided modes. The gray area marks the light cone, LL is the light line, the blue area marks TM-like slab modes, the pink area marks TE-like slab modes, the purple area marks both TE- and TM-like slab modes. The labels A, B, C mark the different modes considered in this chapter. All measurements were conducted in the range marked by the orange bar.

In the optical domain the algorithm has so far been used to identify dispersion relations in photonic-crystal waveguides [59, 142]. To date, however, 2D spatial patterns of Bloch modes at optical frequencies have not been obtained with this method.

In this chapter, we show the power of the Bloch mode reconstruction algorithm by extracting individual 2D mode patterns from phase-sensitive NSOM measurements on a GaAs photonic-crystal waveguide. We discuss in detail a specifically measured field pattern for which the Bloch modes are reconstructed. We apply this algorithm to study the behavior of the spatial width of the lowest frequency TE-like guided mode in the 2D band gap for TE-polarized light as a function of the wave vector.

4.2. Waveguide description and Bloch mode reconstruction

Figure 4.1(a) illustrates the top view of the waveguide studied here. It consists of a GaAs photonic-crystal slab with holes forming a triangular lattice with pitch size $a = 240 \pm 10$ nm, normalized hole radius $r/a = 0.309 \pm 0.002$, waveguide length of approximately 1 mm and slab thickness $h = 160 \pm 10$ nm. A single row of missing holes forms a W1 waveguide. Light is guided in the $\hat{x}$ direction. Each numbered rectangle represents a unit cell. Fig. 4.1(b) shows the calculated band structure along $\hat{x}$ for the photonic-crystal waveguide surrounded by air using a plane wave expansion [91] (assuming a constant refractive index of $n_{\mathrm{GaAs}} = 3.56$ and thickness $h/a = 0.67$). The black diagonal line represents the light line, corresponding to light propagation in air. Modes above the light line couple to modes outside the waveguide, are therefore lossy [6] and are not considered here. The blue and pink areas mark a continuum of modes propagating in the surrounding photonic crystal for TM- and TE-polarized light, respectively. The blue and red curves describe modes for, respectively, TM- and TE-polarized light that are guided by the line defect. Here we concentrate on modes A and B that are TM-polarized, and mode C that is TE-polarized.

A continuous-wave diode laser (Toptica DL pro 940) is used with a linewidth of 100 kHz and an emission wavelength between $907 - 990$ nm, corresponding to a normalized frequency $\omega a/2\pi c_0$ in the range $0.24 \ldots 0.26$. Light is side-coupled on a cleaved end-facet of the 1 mm long waveguide with a high-NA glass objective (NA=0.55). The incident light is linearly polarized with an angle of about 45^o with respect to the normal of the waveguide to excite both TE- and TM-like modes. The field pattern is collected approximately 100 μm away from the coupling facet using an aluminum coated fiber tip with an aperture of 160 ± 10 nm. We perform phase-sensitive NSOM using heterodyne detection. Detailed descriptions of a similar setup are presented in Ref. [56].

The propagating modes considered here represent eigenmodes of the crystal and can therefore be represented by Bloch modes. A Bloch mode propagating in the $\hat{x}$ direction at position $\mathbf{r} = [x, y]$ and frequency ω is described by $\Psi_m(\mathbf{r}, \omega) = \psi_m(\mathbf{r}, \omega)\exp(\mathrm{i}k_m \frac{x}{a})$. Here $\psi_m(\mathbf{r}, \omega)$ is an envelope that is periodic with the lattice and satisfies $\psi_m(\mathbf{r}, \omega) = \psi_m(\mathbf{r} + a\hat{x}, \omega)$, m labels the Bloch mode, and k_m is the corresponding normalized Bloch vector with respect to a (we consider normalized wave vectors only) and $\exp(\mathrm{i}k_m \frac{x}{a})$ is a plane wave. We restrict ourselves to propagating modes ($k \in \mathbb{R}$). It is assumed that the measured field pattern $\Phi(\mathbf{r}, \omega)$ can be described by a superposition of M Bloch-modes $\Psi_m(\mathbf{r}, \omega)$ with amplitude a_m and one overall residual $\varepsilon(\mathbf{r}, \omega)$:

$$\Phi(\mathbf{r}, \omega) = \sum_{m=1}^{M} a_m \Psi_m(\mathbf{r}, \omega) + \varepsilon(\mathbf{r}, \omega). \tag{4.1}$$

The residual $\varepsilon(\mathbf{r}, \omega)$ describes measured field patterns that cannot be described by the M Bloch modes, such as modes that do not follow the periodicity of the lattice, such a defect states, but also accounts for experimental artifacts and

noise.

In the reconstruction algorithm [59, 140] a section of the waveguide is separated into N unit cells, see Fig. 4.1(a). The algorithm uses the property that each $\psi_m(\mathbf{r},\omega)$ is periodic in the photonic-crystal lattice, and requires us to analyze the measured field for each unit cell $U_n(\mathbf{r}',\omega)$, with $\mathbf{r}'$ the coordinate within one unit cell. The measured $\Phi(\mathbf{r},\omega)$ can be fitted with a sum of Bloch modes using a least squares optimization that minimizes the functional $W = \int |\varepsilon(\mathbf{r},\omega)|^2 d\mathbf{r} / \int |\Phi(\mathbf{r},\omega)|^2 d\mathbf{r}$. This procedure results in the field pattern $A_m = a_m \psi_m(\mathbf{r},\omega)$ and the Bloch vector k_m for $m = 1 \ldots M$. We compare the extracted k_m with wave vectors determined from spatial Fourier transforms to confirm the accuracy of the algorithm.

4.3. Near-field patterns decomposed in propagating Bloch modes

Figure 4.2(a) shows the measured field amplitude $|\Phi(\mathbf{r},\omega)|$ for a waveguide section of 30 unit cells (7.2 ± 0.5 μm) at a wavelength of $\lambda = 931.6 \pm 0.1$ nm, which is equivalent to $\omega a / 2\pi c_0 = 0.257$. A beating pattern with a period of 5.7 ± 0.2 unit cells, indicated by the meandering maximums, reveals that multiple modes are involved in the spatial pattern. To ensure that each $U_n(\mathbf{r}',\omega)$ describes precisely one unit cell, the original measurement was resampled on a different grid. Figure 4.2(b) shows the reconstructed amplitude $|\sum_{m=1}^{M} A_m(\mathbf{r},\omega)|$ with $M = 7$ Bloch modes, which is in excellent agreement with the measured field amplitude. We have chosen $M = 7$ because we expect from Fig. 4.1(b) a forward propagating mode corresponding to the light line (which can also be approximated by a Bloch mode [31]) and for modes A, B and C both forward and backward propagating components, hence $M = 1 + (2 \times 3) = 7$. The low values for the functional $W = 0.0133$ demonstrates that indeed $\Phi(\mathbf{r},\omega)$ is well described by the superposition of 7 Bloch modes. This conclusion is confirmed by the absolute residuals $|\varepsilon(r,\omega)|$ plotted in Fig. 4.2(c). The fitted k_m are presented in the second column of Tab. 4.1. The third column describes the relative contribution of each mode as $c_m = |\int A_m^*(\mathbf{r},\omega)\Phi(\mathbf{r},\omega) d\mathbf{r}| / \int |\Phi(\mathbf{r},\omega)|^2 d\mathbf{r}$. Note that the 7 contributions plus that of the residual add up to unity. The fifth column describes which modes of Fig. 4.1(b) correspond to k_m, the propagation direction and polarization. We observe mainly the forward propagating TE-like mode C ($m = 5$) and the forward propagating TM-like mode A ($m = 4$). The errors in k_m are estimated by varying the grid element size and allowing for a relative increase of ΔW by maximum 10%; within this range the mode patterns $A_4(\mathbf{r},\omega)$ and $A_5(\mathbf{r},\omega)$ do not change noticeably.

Next, the fitted k_m are compared with wave vectors determined from the spatial Fourier transforms (k_{SFT}) that are shown in Fig. 4.2(d). A Fourier transform in the $\hat{x}$ direction was made for each line parallel to the waveguide over a range of 35.4 ± 0.9 μm, which includes the range shown in Fig. 4.2(a). For comparison k_m and k_{SFT} are listed in Tab. 4.1, showing an excellent agreement. The spatial

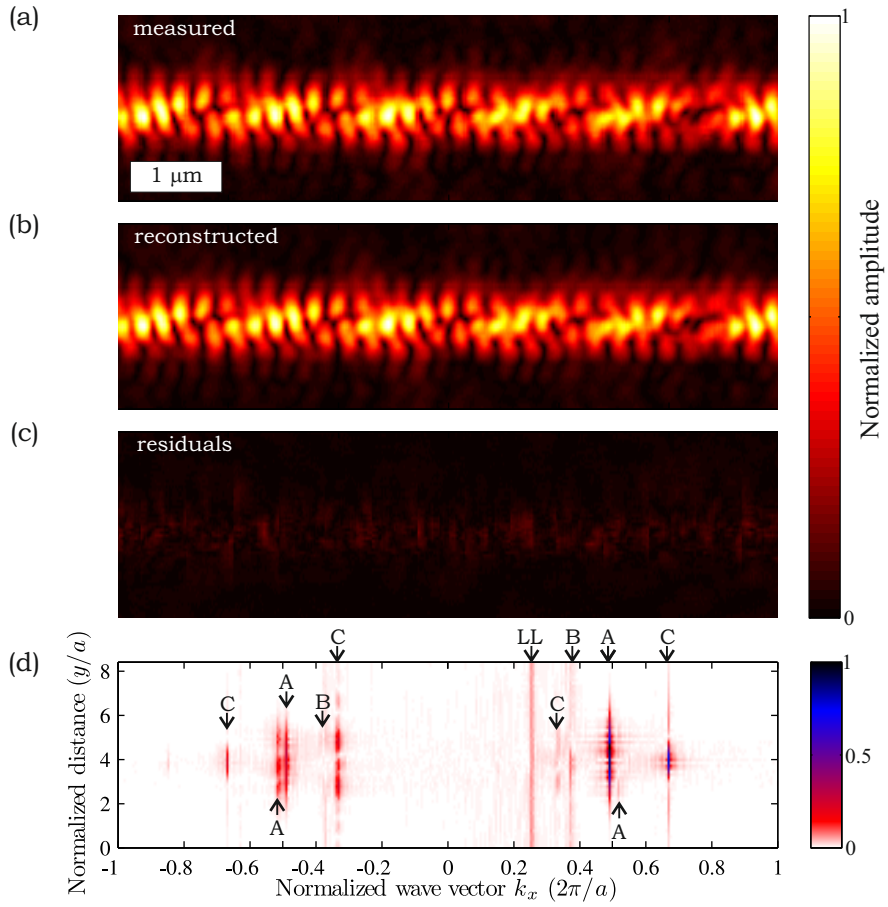

Figure 4.2. Reconstructed Bloch modes of a measured near-field pattern on a photonic-crystal waveguide. (*a*) Measured amplitude for a photonic-crystal waveguide at 931.6 ± 0.1 nm. (*b*) Fitted amplitude using 7 reconstructed Bloch modes over 30 unit cells. (*c*) Residual amplitude. (*d*) Amplitude coefficients of the spatial Fourier transforms of the measured near-field pattern. Labels correspond to those in Fig. 6.1(*b*).

Table 4.1. Comparison between fitted wave vectors from Bloch-mode reconstruction (k_m), and obtained wave vectors from spatial Fourier transforms (k_{SFT}). The first column labels the Bloch modes. The second column gives the fitted k_m. The third column gives a measure how strongly present a mode is. The fourth column gives the k_{SFT}, where the superscript F marks the fundamental wave vector. In the fifth column we identify the modes from the calculated band structure in Fig. 4.1(b), the propagation direction, where $+(-)$ corresponds to the positive(negative) $\hat{x}$ direction, and polarization.

m	k_m $(\frac{2\pi}{a})$	c_m	k_{SFT} $(\frac{2\pi}{a})$	Label
1	0.251(1)	0.0073	0.251(3)	$+LL$
2	0.330(3)	0.0117	$-0.668(3)^F$, 0.331(3)	-C, TE
3	0.379(2)	0.0086	0.370(3)	+B, TM
4	0.488(2)	0.6714	$-0.516(3)$, $0.489(3)^F$	+A, TM
5	$-0.331(2)$	0.2202	$-0.332(3)$, $0.668(3)^F$	+C, TE
6	$-0.367(6)$	0.0014	$-0.370(3)$	-B, TM
7	$-0.486(2)$	0.0681	$-0.489(3)^F$, 0.516(3)	-A, TM

Fourier transforms show for modes A and C higher Bloch harmonics. Both the fundamental k_{SFT} and the observed higher Bloch harmonics are listed in the table. In Fig. 4.2(d) the modes from Fig. 6.1(b) are identified. The amplitude coefficients confirm that we detect mainly the forward propagating TE-like mode C ($k_{\mathrm{SFT}} = -0.332 \pm 0.003, 0.668 \pm 0.003$) and the forward propagating TM-like mode A ($k_{\mathrm{SFT}} = -0.516 \pm 0.003, 0.489 \pm 0.003$).

We have demonstrated that the forward propagating TE-like mode C and the forward propagating TM-like mode A are the most prominent Bloch modes present in the data of Fig. 4.2. Figure 4.3(a) shows the amplitude when only these two modes are taken into account for the reconstruction. A very good agreement is observed with $\Phi(\mathbf{r}, \omega)$ of Fig. 4.2(a). Especially the diagonal beats are well reproduced. The difference wave vector of the two modes corresponds to a beating period of $(5.5 \pm 0.2)a$. The beating pattern of two orthogonal modes is the result of quasi-interference; the NSOM tip thereby projects both orthogonal modes on a detection basis where these modes interfere [143]. Figure 4.3(b) shows the amplitude, the real part and the imaginary part of the reconstructed TE-like Bloch mode C with $k_5 = -0.331 \pm 0.002$. The mode profile is symmetric in the $\hat{y}$ direction about the center of the waveguide. Figure 4.3(d) shows the calculated [91] time-averaged amplitude $\langle |E| \rangle$ for the TE-like mode (left) and the measured amplitude $|A|$ for approximately 3 unit cells. Both show a similar pattern. Figure 4.3(c) shows the amplitude, the real part and the imaginary part of the reconstructed TM-like Bloch mode A with $k_4 = 0.487 \pm 0.003$. Figure 5.3(e) shows the calculated $\langle |E| \rangle$ for the TM-like mode (left) and the measured amplitude $|A|$ for approximately 3 unit cells (right). For mode A the agreement is poor, likely because the near-field tip has a low response to E_z and a non-trivial

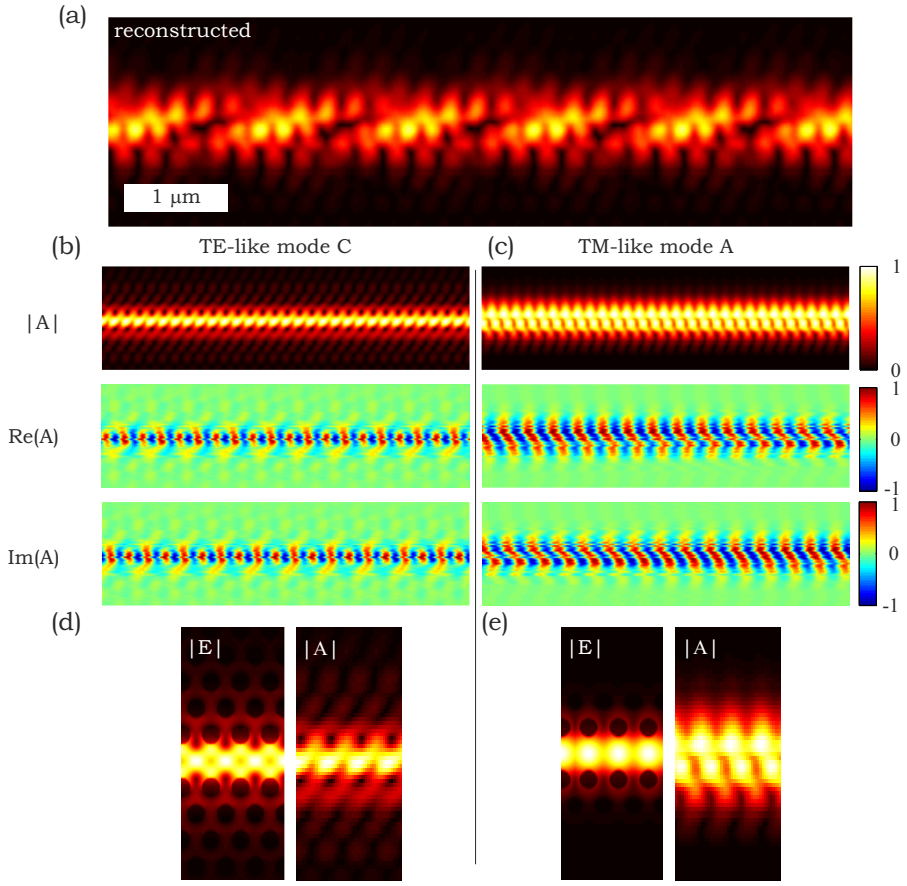

Figure 4.3. Measured near-field pattern decomposed in two Bloch modes. (a) Reconstructed amplitude for Fig. 4.2(a) using Bloch modes $m = 4$ and $m = 5$ only. $(b - c)$ Reconstructed amplitude, imaginary part and real part for both Bloch modes. $(d - e)$ Comparison between calculated $|E|$ (left) and reconstructed $|A|$ (right).

response to E_x and E_y, see Ref. [139], in addition to its finite resolution. The reconstructed field patterns are an approximation of the Bloch modes propagating in the system and moreover, they are not necessarily orthogonal because of quasi-interference. Although the effect of the tip is far from straightforward ([58, 144, 145]), we anticipate that the comparison between calculated modes of an optical system and reconstructed modes could lead to methods to deduce the response function of a near-field tip.

4.4. Reconstructed width of the TE-like guided mode

Next, we demonstrate the power of the reconstruction algorithm by studying the transverse behavior of TE-like mode C versus wave vector. We consider the forward propagating TE-like mode ($k_5 = -0.331, 0.669$ in Fig. 4.3) and take its reduced wave vector ($0 < k_x < 0.5$) to compare directly with the folded band structure of Fig. 4.1(b). We have measured field patterns in the wavelength range of $\lambda = 907 - 944$ nm, and apply the reconstruction algorithm to determine $A(\mathbf{r}, \omega)$ and k_x for this mode at each λ. We have selected $\Phi(\mathbf{r}, \omega)$ where this TE-like mode is prominently present in spatial Fourier transforms. The inset in Fig. 4.4(c) shows the fitted k_x versus normalized frequency $\omega a/2\pi c_0$.

In order to concentrate on the transverse behavior, we define the transverse mode profile $\int_0^a |A(\mathbf{r}, \omega)| dx$. Figure 4.4($a$) shows the measured normalized transverse mode profile for three different wave vectors. At $k_x = 0.285$ (black curve) a transverse mode profile is apparent that can be mainly described by one prominent maximum at $y/a = 0$ that is slightly asymmetric, describing light guided in the line defect. Additional side lobes are observed at $y/a = -0.9$ and at $y/a = 1.4$, representing light extending into the surrounding photonic crystal. At $k_x = 0.332$ (red dashed curve) we observe a central maximum at $y/a = 0$, and the contributions of the side lobes become stronger. Also note the new peaks observed at $y/a = -3.2, -2.2, -1.5$, and 2.8. When the wave vector is increased, the relative contributions of these additional peaks increase. At $k_x = 0.375$ (blue dashed curve) the central peak is still present, and the contributions of the surrounding peaks have grown. Qualitatively, the measured transverse mode profiles correspond with the calculated ones shown in Fig. 4.4(b), which were obtained from the time-averaged amplitude of the total electric field $\int_0^a |E(\mathbf{r}, \omega)| dx$. The maxima and minima occur at approximately the same locations and the width w of the central maximum is growing with increasing k_x. Not all features are resolved of the calculated transverse mode profile in our measurements. For example, the measured relative amplitude of the central maximum compared with the additional maxima differs from the calculations.

The central maxima of the transverse mode profiles are fitted with a Gaussian with width w. Figure 4.4(c) shows the normalized width w/a versus wave vector (black symbols, bars represent 95% convergence intervals). The red symbols

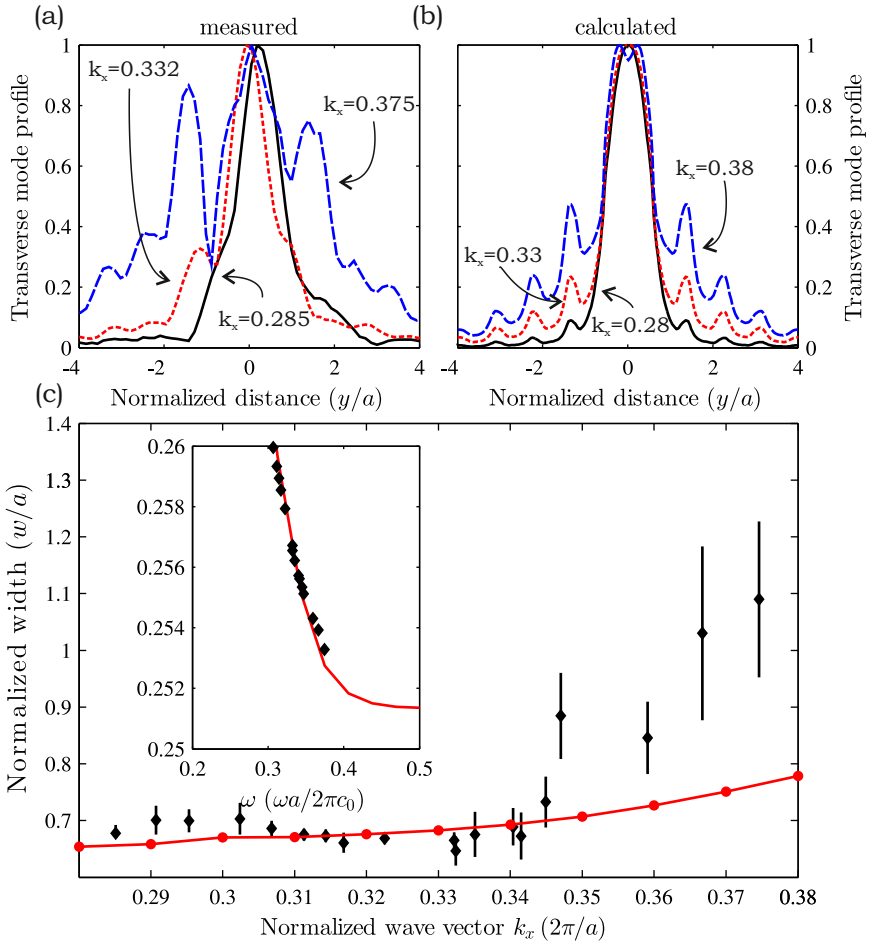

Figure 4.4. Extracted mode width as a function of wave vector. (*a*) Measured normalized transverse mode profile for $k_x = 0.285$ (black), $k_x = 0.332$ (red dashed), and $k_x = 0.375$ (blue dashed). (*b*) Calculated normalized transverse mode profile for $k_x = 0.280$ (black), $k_x = 0.330$ (red dashed), and $k_x = 0.380$ (blue dashed). (*c*) Determined (black) and calculated width w (red) versus longitudinal wave vector k_x for the TE-like guided mode. Inset: measured (symbols) and calculated dispersion (red).

interpolated by the dashed curve represent w/a determined from the calculated transverse mode profile. The measured w increases with k_x. For $k_x < 0.34$ the measured w matches the calculated w well. For $k_x > 0.34$ the measured w becomes larger than the calculated w. We attribute this to the finite resolution of the near-field tip and to its response function. For most considered k_x-values, however, the measured w/a matches the calculated with a 10% accuracy.

4.5. Summary and outlook

In conclusion, we have implemented an algorithm proposed by Ha *et al.* to extract Bloch modes from near-field measurements on a photonic-crystal waveguide. The extracted wave vectors are in very good agreement with the wave vectors determined from spatial Fourier transforms. We have studied two extracted Bloch modes to explain the observed near-field pattern. We also have studied how the width of a selected mode changes with wave vector and find good agreement with calculations. This algorithm seems excellently suited to study individual modes in multi-mode periodic systems. We anticipate that this algorithm can be used to filter states that cannot be described by propagating Bloch modes, such as Anderson-localized states observed in the slow-light regime [15, 18, 54, 146], as is demonstrated in appendix A.

CHAPTER 5

Measurement of a band-edge tail in the density of states of a photonic-crystal waveguide

We investigate light transport near the band edge of slow-light photonic-crystal waveguides using phase-sensitive near-field microscopy. We obtain and interpret high-resolution band structures, allowing the retrieval of the optical density of states for a one-dimensional periodic system with weak intrinsic disorder. Because of this disorder, the band edge is smeared and the van Hove singularity is removed. The density of states shows a decaying tail in the band gap corresponding to Anderson-localized modes, as predicted by Lifshitz for solid-state systems.

5.1. Introduction

Band gaps and accompanying band-edge effects are among the most intriguing phenomena in solid-state physics [28]. Unavoidable disorder in periodic media strongly alters the transport of electrons, phonons or photons, ultimately resulting in the breakdown of transport, known as Anderson localization [13, 48, 49, 147, 148]. Electromagnetic waves form an excellent platform to study the effects of disorder on bosonic propagation because of the availability of strong scatterers, a high energy and wave vector resolution, polarization- and phase control, and subwavelength fabrication precision. For many years, microwave experiments have improved our understanding of disorder, such as the demonstration of localized modes near the band edge [149, 150]. However, with current nanofabrication methods, nanophotonic structures have become excellent alternatives for performing experiments at optical energies. This allows us to study the influence of disorder with a direct impact on applied nanophotonics.

Photonic-crystal waveguides are commonly used for strong light confinement with unique dispersion essential for slow light propagation and enhanced light-matter interactions [6, 52, 137, 151]. Light propagation in these waveguides can be approximated by one-dimensional transport. Intrinsic disorder results in Anderson-localized modes [5], smearing of the band edge and removal of the Van Hove singularity. The localized modes in the band gap contribute to the

The content of this chapter has been published as: S.R. Huisman, G. Ctistis, S. Stobbe, A.P. Mosk, J.L. Herek, A. Lagendijk, P. Lodahl, W.L. Vos, and P.W.H. Pinkse, Phys. Rev. B. **86**, 155154 (2012).

formation of the optical equivalent of a Lifshitz tail in the density of states (DOS) [152]. For doped semiconductors and superconductors, the Lifshitz tail is known as a tail in the DOS that decays away from the band edge caused by the ensemble of localized states [153–157]. Indeed, Anderson-localized modes in photonic-crystal waveguides have been demonstrated near the band edge [15, 18, 146, 158–160]. Furthermore, recent optical experiments demonstrate that the effects of strong scattering can be observed in the DOS [18, 161–164]. However, no experiments near the band edge have been conducted to reveal the optical Lifshitz tail in the DOS. Band-edge phenomena in the DOS have been studied with scanning tunneling microscopy (STM) and spectroscopy (STS) for many years. Surprisingly, to our knowledge, a clear identification of a Lifshitz tail is missing, possibly caused by complicated band structures, fabrication control, temperature broadening, and the available energy resolution.

In this chapter, we combine the optical analog of STM, near-field scanning optical microscopy (NSOM) [8], with photonic-crystal waveguides. NSOM offers unique opportunities to measure the wavefunction and the band structure [51, 57–59, 160, 165, 166]. We observe, near the band edge for transverse electric (TE)-like waveguide modes, Anderson-localized modes that weakly couple to ballistic transverse magnetic (TM)-like modes that extend over the entire waveguide. The localized modes are seen to explicitly smear out the band edge in the band structure, an observation most relevant for disordered quantum systems [167]. From the band structure the DOS is reconstructed, demonstrating the absence of the Van Hove singularity and yielding a direct observation of an optical Lifshitz tail in a one-dimensional (1D) system.

5.2. Experimental setup and waveguide properties

Figure 6.1(a) illustrates our experiment. A continuous-wave laser (Toptica DL Pro 940) with a tunable wavelength λ between 907 and 990 nm, and a linewidth of 0.1 MHz is side-coupled on a cleaved end facet of a GaAs photonic-crystal waveguide (right SEM image) with an objective (NA=0.55). The incident light is polarized with an angle of approximately 45^o with respect to the normal of the waveguide to excite both TE-like (polarization is oriented in the crystal plane, $E \parallel y$) and TM-like modes (polarization is oriented perpendicular to the crystal plane, $E \parallel z$). The field pattern is collected approximately 200 μm away from the coupling facet using an aluminum coated near-field tip with an aperture of 160 ± 10 nm (left SEM image). We perform phase-sensitive NSOM using heterodyne detection [143].

The photonic-crystal waveguide consists of a 1-mm-long photonic-crystal slab with holes forming a triangular lattice with pitch $a = 240$ nm, a normalized hole radius of $r/a = 0.309$, and a slab thickness $h = 160$ nm. A row of missing holes forms the W1 waveguide. Details on sample fabrication can be found in Refs. [18] and [146], where Anderson localization was demonstrated for waveguides fabricated under identical conditions. Figure 6.1(b) shows the calculated band structure along the propagation axis for such a photonic-crystal waveguide [91].

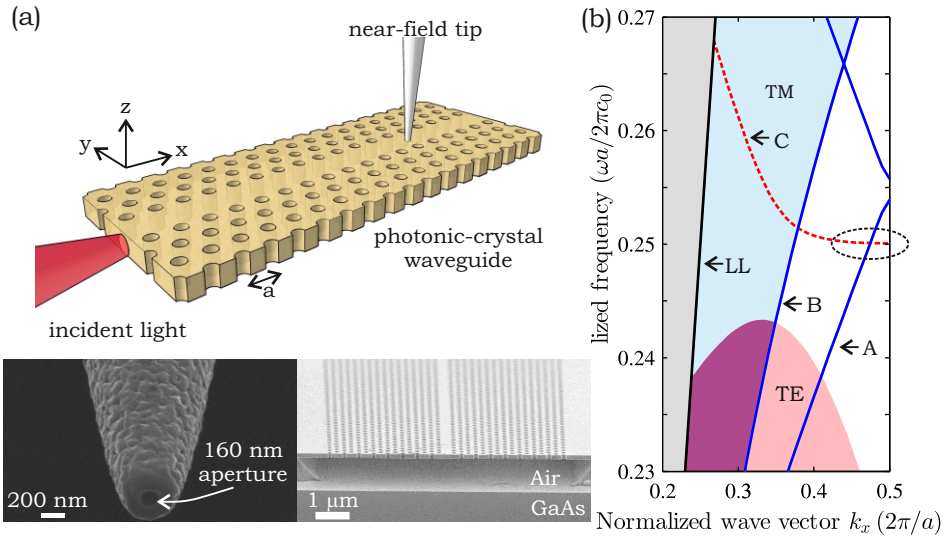

Figure 5.1. Experimental scheme for studying light transport in photonic-crystal waveguides. (*a*) Laser light is side-coupled on a GaAs photonic-crystal waveguide. Light propagation is studied with a near-field tip. SEM images are shown of the coated near-field tip (left) and the waveguide (right). (*b*) Calculated band structure showing both TE-like (red dashed) and TM-like (blue) guided modes in the 2D band gap for TE-like modes for ($r/a = 0.303$, $h/a = 0.67$). The encircled area is the main focus of this chapter. Here, the TE-like waveguide mode C becomes flat at the band edge, leading to a Van Hove divergence in the DOS. The black diagonal line represents the light line (LL).

The blue solid curves and red dashed curve describe modes that are guided by the line defect for TM- and TE-polarized light, respectively. The blue and pink areas mark continua of modes propagating in the surrounding photonic crystal for TM- and TE-polarized light, respectively, which overlap at the purple area. We concentrate on modes A and B, which are TM-like, and mode C, which is TE-like. Intrinsic disorder causes Anderson localization in the slow-light regime of mode C (encircled area near $k_x = 0.5$) [15, 146, 159], where the dispersion relation flattens and the optical DOS ideally diverges, known as a Van Hove singularity.

5.3. Near-field observation of Anderson-localized modes

Figure 5.2 presents measured near-field amplitudes at different excitation frequencies. Periodic beating patterns are observed above and below the band edge of

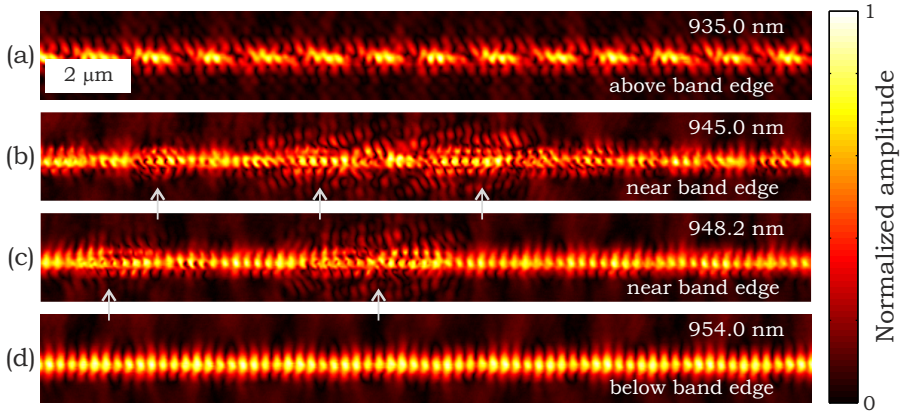

Figure 5.2. Measured near-field amplitude for a photonic-crystal waveguide at different frequencies near the band edge. Propagating extended Bloch modes are observed in (a) and (d), Anderson-localized modes are found in (b, c). The arrows mark localized states.

TE-like mode C. Spatial Fourier transforms [51] and Bloch-mode reconstruction [140] confirm that these patterns are completely described by a superposition of propagating Bloch modes [165]. Since these propagating modes are unperturbed by intrinsic disorder and extend over the entire waveguide, they are considered not to be localized and are therefore referred to as propagating. For $907 \leqslant \lambda \leqslant 942.4$ and $954.9 \leqslant \lambda \leqslant 990\,\text{nm}$ patterns of propagating Bloch modes similar to that of Fig. 5.2(a) and Fig. 5.2(d), respectively, were observed.

Figures 5.2(b) and (c) are measured near the band edge, corresponding to frequencies in the range where the periodic patterns are perturbed by standing-wave field patterns (marked by arrows) that extend up to approximately $3a$ into the surrounding crystal. These perturbations are the Anderson-localized modes that are expected at the band edge. We have verified that these localized modes occur at random locations along the waveguide only within a wavelength range of $942.4 - 954.9\,\text{nm}$ near the band edge of mode C.

The extended field patterns in the surrounding photonic crystal indicate high field amplitudes in the center of the waveguide. The observed maximum amplitude is likely quenched by the presence of the near-field tip. From spatial Fourier transforms we know that the periodic background is formed by TM-like modes A and B, which contain most of the field energy [165]. The observed localized modes agree well with calculated profiles of localized modes [152, 168]. Moreover, from Bloch-mode reconstruction [140] we know that these are not a superposition of Bloch modes, as is demonstrated in appendix A. Clearly, from Figs. 5.2(b) and (c) it can be deduced that the presence of the localized modes is strongly wavelength dependent.

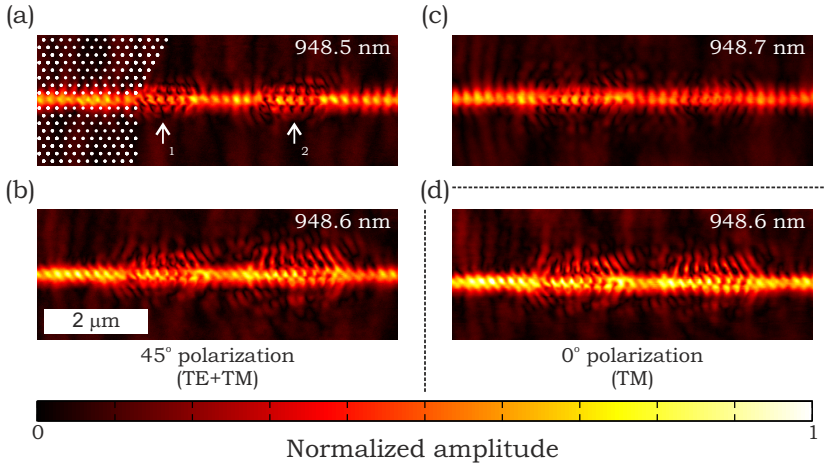

Figure 5.3. Coupling between ballistic and Anderson-localized modes. Amplitude for two coupled localized modes (arrow 1 and 2) for 3 wavelengths separated by 0.1 nm for two incident polarizations with respect to the pores ($(a-c) \approx 45^o$; (d) 0^o). Amplitudes are normalized to the amplitude of light propagating along the surface of the structure. White circles in (a) indicate the location of the holes.

Localized modes in photonic-crystal waveguides are known to be narrowband [15, 18, 146, 152, 158, 159, 168]. In Fig. 5.3 we show the wavelength dependence of two such modes (1 and 2) with a resolution of $\Delta\lambda = 0.1$ nm. In Fig. 5.3(a) we observe that the periodic pattern is perturbed at the locations of the arrows at $\lambda = 948.5$ nm. In Fig. 5.3(b) we observe the localized mode at $\lambda = 948.6$ nm, where the perturbations develop maximally in the surrounding photonic crystal. In Fig. 5.3(c) at $\lambda = 948.7$ nm, the localized modes vanish. At $\lambda = 948.9$ nm the localized modes have completely vanished (not shown). This demonstrates that these localized modes have a linewidth of $\Delta\lambda \approx 0.2$ nm, corresponding to a quality factor of $Q \simeq 10^3 - 10^4$. We have observed $\sim 10^2$ of such localized modes and they fully extend within a range of typically $\Delta\lambda < 0.5$ nm. The observed linewidths should be considered as an upper limit for the true resonance widths, since near-field tips are known to shift and broaden resonances [58, 144, 145].

We observe Anderson-localized modes far along the waveguide, where the intensity should naively be vanishingly small. Therefore we explain how the modes are excited. The near-field patterns in Fig. 5.3$(a-c)$ were obtained with an incident polarization angle of approximately 45^o with respect to the normal of the photonic-crystal waveguide to excite both TE- and TM-like modes. Figure 5.3(d) shows the near-field pattern at $\lambda = 948.6$ nm when the incident polarization angle is 0^o to excite only TM-like modes. We observe a field pattern identical to that in Fig. 5.3(b). From spatial Fourier transforms, only TM-like Bloch modes

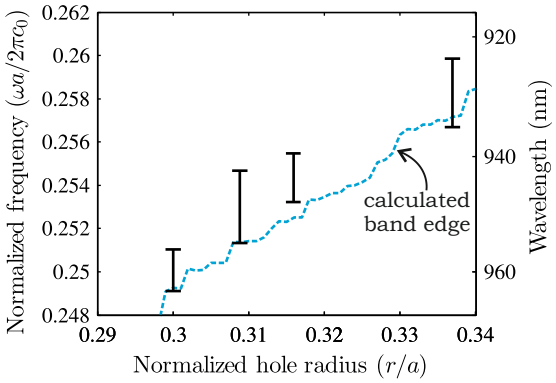

Figure 5.4. Observed frequency range for localized modes in photonic-crystal waveguides with different pore radii. All photonic-crystal waveguides have a pitch of $a = 240$ nm and a thickness of $h = 160$ nm. The blue dashed curve corresponds to the calculated band edge.

were identified, but the localized modes remained observed. We conclude that we are detecting a subset of localized modes at the band edge for the TE-like mode C that are excited by the TM-like propagating mode A, consistent with previous interpretations [158]. We anticipate that the weak coupling between localized modes and ballistic light offers an opportunity to address, manipulate, and read out light-matter interactions with localized modes.

In previous work localized modes were found to appear near the band edge of mode C [15]. In Fig. 5.4 we show the measured frequency range where localized modes occur as a function of normalized hole radius for four photonic-crystal waveguides with different hole radii. A gratifying agreement is observed with the calculated band edge. The frequency ranges are determined from near-field images when perturbation like in Fig. 5.2 appear. We estimate an error of 1 nm for the wavelength ranges (not shown). The r/a is determined from SEM images with a systematic error of 5% (not shown).

5.4. Band structure reconstruction and extraction of the Lifshitz tail

We have collected near-field patterns over the wide spatial range of $x = 73$ μm and $y = 2.5$ μm for a whole range of normalized laser frequencies ω[1] and obtained their spatial Fourier transform $S_{\text{int}}(k_x, y, \omega)$. We have calculated the spatial Fourier transform $S(k, y, \omega)$ for each line parallel with the line defect. We define $S_{\text{int}}(k, \omega) = \int |S(k, y, \omega)| dy$. All $S_{\text{int}}(k, \omega)$ are normalized to have the same average value for $-3.5 < k_x < -1.8$, which is dominated by $1/f$ noise. This

[1]Every frequency in this subsection is normalized as $\omega a/2\pi c_0$.

procedure resulted in the experimentally reconstructed band structure shown in Fig. 5.5(a) [51]. At $0 < k_x < 0.5$ the calculated folded band structure in Fig. 6.1(b) is overlapped as symbols, showing good agreement with the maxima in $S_{\rm int}(k_x, \omega)$. One expects that Bloch harmonics repeat every Brillouin zone ($k_x = k_0 + na$, $n \in \mathbb{Z}$) and are symmetric around the Bragg conditions ($k_x = n + 0.5$, $n \in \mathbb{Z}$). The identification of the modes as TE-like (circles) and TM-like (triangles) modes was confirmed by rotating the polarization of the incident light. We identify a narrow stopgap for mode A at $\omega_s = 0.2555$ ($k = -0.5, 0.5$). As a consequence, the overlap with the excitation beam changes and hence the spatial Fourier transform amplitudes of the modes change abruptly around $\omega \approx \omega_s$. The band edge for TE-polarized mode C is located at $\omega = 0.250$ ($k = -0.5, 0.5$).

In Fig. 5.5(b) a zoom-in of the band structure is shown near the band edge of mode C in the range $-1 < k_x < -0.5$. A most intriguing feature is that our measurements do not show a sharp band edge, but a softened cutoff, in agreement with predictions of Ref. [152]. The smearing-out of the cutoff in the range $0.247 < \omega < 0.251$ is caused by localized states, and starts to appear at a fitted group index of $n_g(\omega = 0.251) = 37$. No localized modes are observed outside this cutoff region. The width of the blurred cutoff $\Delta\omega = 0.004$ is a measure for the amount of disorder. If variations in the hole size and position are the dominant source of disorder [152], this would indicate a standard deviation of $\sigma = 0.015a$ in the hole positioning and hole radius, in reasonable agreement with sample characterization. The group index at which we first observe localized modes is consistent with our previous estimate [18]. Mode (D) is not a Bloch mode, but likely the result of a third-order scattering process, since its wave vector is given by $2k_C - k_A$ (one has to take mode A in the range $-0.5 < k_x < 0$ and mode C in the range $-1.0 < k_x < -0.5$). Also, higher-order modes like $3k_A$ are observed (not shown here). We suspect that these additional modes are caused by the χ^3 nonlinearity of GaAs. This therefore is a potential system for study of the relation between nonlinear transport and disorder.

Figure 5.5(c) shows the main result of this chapter: We have reconstructed the DOS from the bands in Fig. 5.5(b). For each ω we have calculated the number of k_x-bins that satisfy $|S_{\rm int}(k_x, \omega)| > q$, with $\Delta k_x = 0.0033$ and threshold $q = 0.08$. This measure for the DOS is shown in Fig. 5.5(c) (black curve). The extra mode (D) is excluded. The shape of the reconstructed DOS is not very sensitive to the exact value of q, as indicated by the gray area behind the curve, indicating the reconstructed DOS in the range $0.06 < q < 0.1$. We have applied a similar sampling method to the calculated band structure of Fig. 6.1(b) to modes A, B and C, representing the calculated DOS of an ideal periodic waveguide (red curve). This DOS is scaled to have the same value as the experimental DOS in the range $0.255 > \omega > 0.254$. Both the experimental and calculated DOS are approximately constant in the range $0.255 > \omega > 0.251$ and for $0.247 > \omega$. For these frequency ranges no localized modes are observed. Note the contribution of the TM-like modes, which lead to a finite DOS for $0.247 > \omega$. In the range $0.251 > \omega > 0.250$ both the experimental and the calculated DOS increase rapidly. The DOS of an ideal periodic system diverges to infinity at the gap frequency $\omega_{\rm gap}$ as $\rho(\omega) \propto (\omega - \omega_{\rm gap})^{-1/2}$, forming the Van Hove singularity [169,

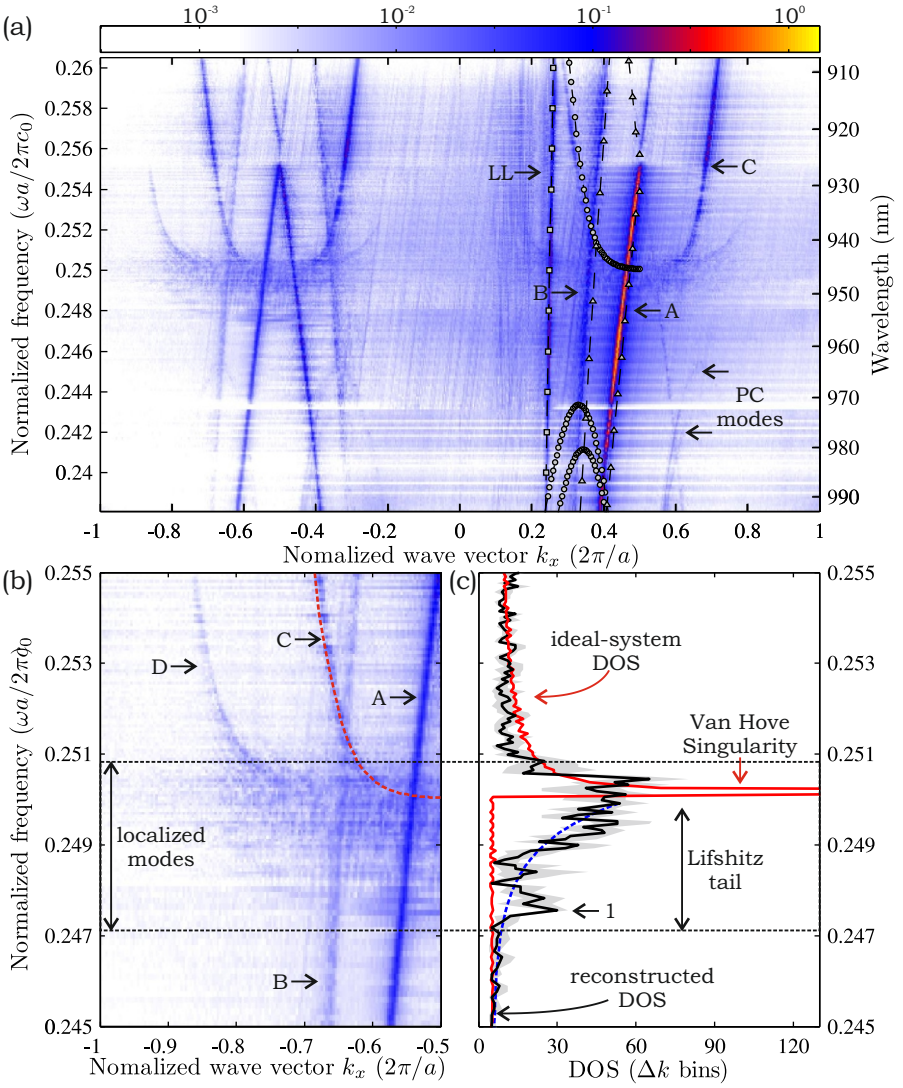

Figure 5.5. Band structure and reconstructed density of states. (*a*) Experimentally reconstructed band structure. The color represents the amplitude of the spatial Fourier coefficients $|S_{\text{int}}(k_x, \omega)|$. Black curves are fitted modes of Fig. 6.1(*b*). The dashed rectangle is highlighted in (*b*), where localized modes are represented by the smeared-out band edge. The dashed red curve approximates mode *C* for the ideal system. (*c*) Experimentally reconstructed DOS (black curve) compared with a fitted DOS (red curve) for an ideal non-disordered waveguide. The single-exponential fit (dashed blue curve) is a guide for the eye for the Lifshitz tail.

170]. The experimental DOS follows this increase, until it saturates at $\omega = 0.2505$. In this range the first localized modes are observed. Although the single peak at $\omega = 0.2476$ (arrow 1) belongs to a single localized mode, it is unclear whether the sharp features in the reconstructed DOS are dominated by individual localized states, since localized states are present at every ω in this range. In future this could be answered by reconstructing band structures with a smaller $\Delta\omega$. It is clear, though, that the Van Hove divergence is absent, in agreement with computations by Savona [152]. In the band gap for $0.250 > \omega > 0.247$ the experimental and the calculated DOS differ significantly: the calculated DOS is constant, whereas the experimental DOS slowly decays away from the band edge, forming the Lifshitz tail known from solid-state systems [153–157]. Our present data do not allow us to draw conclusions about the exact shape of the tail, which is debated in the literature [153–157], but show the possibility of addressing this issue in future experiments.

5.5. Summary and outlook

We have reported near-field measurements of localized modes using phase-sensitive NSOM; the experimentally obtained band structure reveals how the localized states perturb the band edge. Ensemble averaging by measuring band structures of different parts of the sample should smoothen the envelope of the reconstructed DOS and will afford the possibility of quantitatively studying the shape of the Lifshitz tail. Ensemble averaging for several degrees of disorder will allow us to study the scaling properties of localized states near the band edge [171]. We also predict that the Lifshitz tail should appear when the DOS is directly probed by studying the emission of embedded quantum dots [47, 137, 172]. Recently García *et al.* demonstrated in emission experiments that the Lifshitz tail increases with the amount of disorder [173].

Adaptive quantum optics: combining quantum light with wavefront shaping. Incident light on a multiple-scattering material generates speckles. The speckle pattern contains correlations dictated by the interference of the many scattered modes in the material. By modulation of the incident wavefront one can program the correlations. This makes it possible to program quantum interference with opaque scattering media. Photo: a sugar cube illuminated with two HeNe beams.

Part III.

Adaptive quantum optics

CHAPTER 6

Controlling single-photon Fock-state propagation through opaque scattering media

The control of light scattering is essential in many quantum optical experiments. Wavefront shaping is a technique used for ultimate control over wave propagation in multiple-scattering media by adaptive manipulation of incident waves. We control the propagation of single-photon Fock states in opaque scattering media by spatial phase modulation of the incident wavefront. We enhance the probability that a single photon arrives in a target output mode with a factor 30. Our proof-of-principle experiment shows that wavefront shaping can be applied to non-classical light, with prospective applications in quantum communication and quantum cryptography.

6.1. Introduction

Wavefront shaping is an adaptive technique for classical light that transforms random multiple scattering media to a versatile platform for creating programmable speckle patterns with correlations similar to transport in linear optical circuits [26, 27, 60]. Although adaptive techniques have been introduced to quantum light [72, 174–177], such a versatile platform as wavefront shaping is still missing for quantum light.

Light transport in a multiple-scattering medium can be considered as a linear transformation of a multi-mode system by a scattering matrix, which results generally in a speckle pattern [49, 148, 178]. Each far-field speckle spot represents a single output mode of the system. In wavefront shaping the incident wavefront is spatially phase modulated, controlling the degree of mode-mixing of all scattered waves that contribute to the target speckle spots. Recent wavefront-shaping experiments have transformed opaque media in equivalents of waveguides and lenses [26] and optical pulse compressors [63, 64] that are inherently flexible in performance.

Multiple scattering is also an exciting platform for quantum optical experiments [17–19, 21, 74, 75]. Non-classical correlations are observed, even for opaque scattering media [16, 17, 20, 74]. We have started a series of experiments to control quantum interference in multiple-scattering materials by wavefront shaping. Controlling single-photon propagation opens unique opportunities for quantum

The content of this chapter is available on ArXiv:1210.8388 (2012).

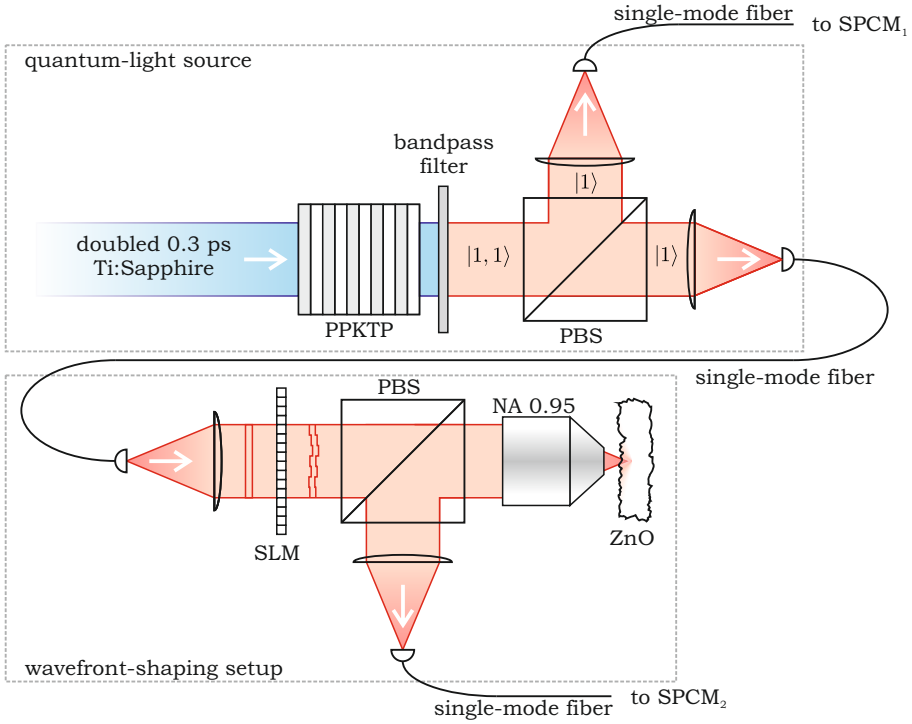

Figure 6.1. Setup for single-photon wavefront shaping. Entangled photon pairs generated in the PPKTP-crystal are separated by a polarizing beam splitter cube (PBS). One photon is fiber-coupled to a single-photon counting module ($SPCM_1$). The conjugate photon is phase-modulated with a spatial light modulator (SLM). The phase-modulated single photon is focused on a layer of white paint (ZnO). Only multiple-scattering events are selected by fiber-coupling the reflection of the PBS to $SPCM_2$.

patterning [179], secure key generation [180], or addressing quantum transport through disordered media [20].

In this chapter we report the first experimental demonstration of wavefront shaping of quantum light. We control light propagation of single-photon Fock states $|1\rangle$ through a layer of white paint. We enhance the probability that a single photon arrives in a target output mode, consisting of a single speckle spot, with a factor 30.

6.2. Experimental setup for single-photon wavefront shaping

A schematic of our setup is shown in Fig. 6.1 and consists of two parts: a quantum-light source (top half) and a wavefront-shaping setup (bottom half).

The quantum-light source is based on earlier work reported by Refs. [181, 182], which gives the opportunity to engineer quantum states up to the two-photon level. A mode-locked Ti:Sapphire laser (Spectra-Physics, Tsunami) emits transform-limited pulses at a repetition rate of 80 MHz with a pulse duration of 0.30 ± 0.02 ps (FWHM of the optical power versus time) and a center wavelength of 790.0 nm. Typically 600 mW is incident on a 5-mm-long BBO nonlinear crystal cut for Type-I frequency doubling. After spectral and spatial filtering, about 70 mW of the frequency-doubled light pulses are focused in a 2-mm-long periodically-poled KTP (PPKTP) crystal cut for type-II spontaneous parametric down-conversion (SPDC) in a single-pass configuration. The polarization-entangled output state can be approximated by:

$$|\Psi\rangle \approx \sqrt{(1-\gamma^2)}|0,0\rangle + \gamma|1,1\rangle, \tag{6.1}$$

where states beyond the single-photon level are omitted. The kets are labeled by the photon numbers in the separate polarization modes, and the constant $\gamma \ll 1$ is proportional to the pump field and the effective nonlinear susceptibility of the PPKTP crystal. The produced light generated by SPDC is filtered with a bandpass filter with a bandwith of approximately 1.5 nm. The modes are separated with a polarizing beam splitter cube (PBS) from which the reflection is used as trigger mode and the transmission as signal mode. Both modes are coupled into single-mode fibers, and the fiber of the trigger mode is connected to a single-photon counting module ($SPCM_1$). Click rates were detected up to $8 \cdot 10^5$ s^{-1}. Coincidence measurements with two detectors in one of the output arms confirmed that a detection event corresponds to a detection of state $|1\rangle$ with a probability of $98 \pm 1\%$. A Hong-Ou-Mandel dip was observed with a visibility of 38%. The dip visibility was independent of the incident pump power, indicating that states beyond the single-photon level can indeed be ignored in our experiment. Further characterization of the source can be found in Ref. [183]. The fiber-coupled signal mode is directed to the wavefront-shaping setup.

The wavefront-shaping setup is based on the configuration described in Ref. [26], with the main difference that we use a reflection configuration. The reflection configuration is expected to give a higher collection efficiency of the scattered modes [180]. The results presented in this chapter have been reproduced by us in a transmission configuration, similar to the experiment described in chapter 7. The signal mode is incident on a spatial light modulator (SLM, Hamamatsu LCOS-SLM) and focused on a layer of white paint with an objective (NA=0.95). The layer of white paint consists of ZnO powder with a scattering mean free path of 0.7 ± 0.2 μm. The reflected speckle pattern is collected with the same objective and polarization filtered with a polarizing beam splitter cube to select multiple-scattered light. One of the speckle spots is coupled to a single-mode fiber that is connected to $SPCM_2$. For convenience we align the setup by wavefront shaping transform-limited laser pulses to extract the phase pattern that is subsequently applied to the signal photons. Calculations based on the dispersion of PPKTP [184] indicate that the expected spectral width of the photons is narrower than 2 times that of the laser pulses (3 nm FWHM, before spectral filtering). After optimization with coherent light, the same phase pattern is used for the single

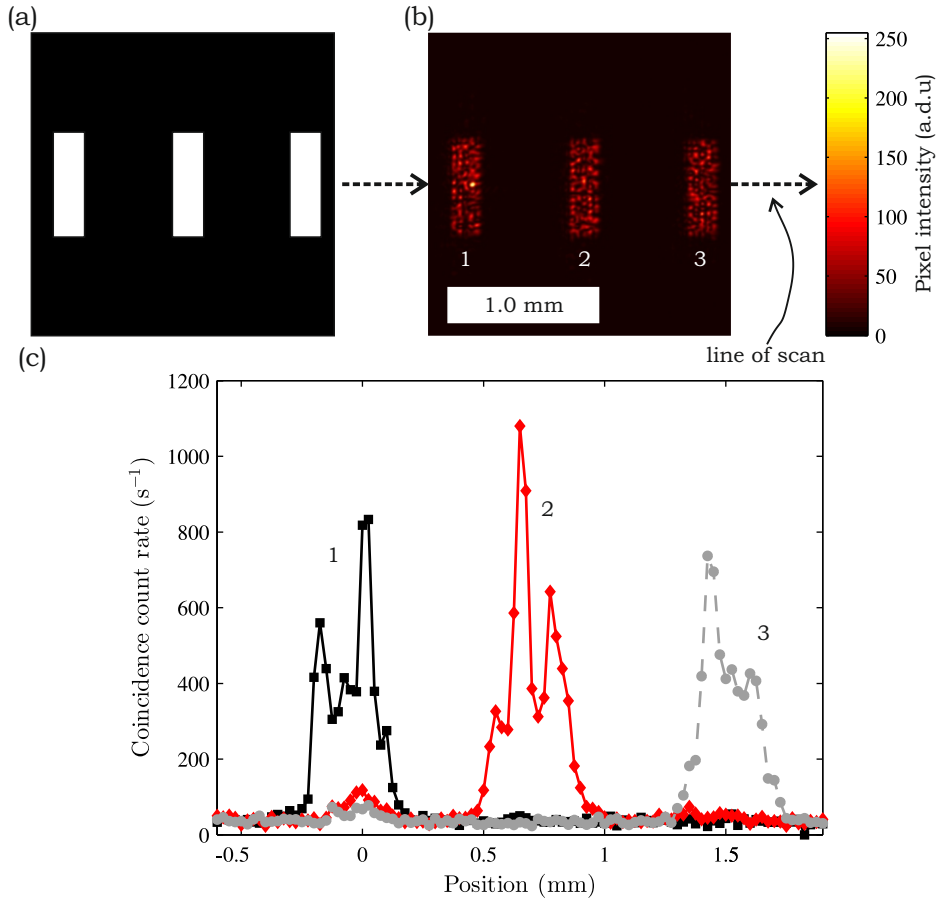

Figure 6.2. Programmable single-photon diffraction patterns. (*a*) Target diffraction pattern consisting of 3 bars. (*b*) Measured diffraction pattern imaged on a CCD camera for laser pulses. (*c*) Measured coincidence count rate for single-photon diffraction when a multi-mode fiber is scanned over the line indicated in (*b*). Each bar is imaged separately (black, red, gray dashed).

photons.

6.3. Wavefront shaping of single-photon Fock states

We first demonstrate in Fig. 6.2 the capability of programming the wavefront of single photons using spatial phase modulation. Figure 6.2(*a*) shows the intended diffraction pattern, consisting of three bright bars. Figure 6.2(*b*) shows the pattern directly behind the SLM imaged with a lens on a CCD camera for incident laser pulses that act as an alignment field for the single photons. The three

bars are clearly visible, where the hologram software (Holoeye) gives a spatially fluctuating intensity distribution of the bars. After we stored the corresponding phase pattern on the SLM, the incident classical laser pulses are replaced with single photons, and the CCD camera is replaced with a multi-mode fiber with a 62.5 μm core diameter connected with $SPCM_2$. The fiber is scanned over the line indicated in Fig. 6.2(b) to detect the coincidence count rate as a function of position. The results are shown in Fig. 6.2(c). Each bar is imaged separately, in order to demonstrate the ability to program the pattern, and to improve the observed coincidence count rate per bar by roughly a factor three. The coincidence count rate is clearly highest in the intended regions, and shows similar spatial intensity fluctuations as observed for laser light.

Figure 6.3 shows the main result of this chapter: a wavefront-shaped single-photon speckle pattern. We first use laser pulses to create an optimized classical speckle pattern with a single enhanced speckle spot. $SPCM_2$ is replaced with a Si-pin photodiode to optimize the reflected pattern for classical laser light. The beam is phase modulated by approximately 500 segments consisting of 20x20 pixels. Each segment is sequentially addressed with a random phase. Only if the intensity increased, this new phase was accepted. This algorithm was repeated approximately 5 times for all segments to obtain a single enhanced speckle spot. Figure 6.3(a) shows the speckle pattern for a constant phase pattern and Fig. 6.3(b) shows the pattern after optimization. A clear enhanced speckle spot is visible in the center of the image. The speckle patterns are measured with a CCD camera.

Figure 6.3(c) shows the result with incident single photons for the same realization. The camera was removed and the target mode is coupled in a single-mode fiber that is connected with $SPCM_2$. Figure 6.3(c) presents the coincidence count rate for different phase patterns; optimized (red), random (white) and constant (gray). 20 subsequent measurements of 1 second integration time were performed for each bar. From the optimized phase pattern we obtain a coincidence count rate which is 33 ± 13 times higher than the average coincidence count rate for random phase patterns. The optimized phase pattern provides a reproducible coincidence rate as indicated by the second red bar in Fig. 6.3(c). We have, hence, increased the probability for a single photon to appear in a desired mode 30-fold, demonstrating the capability of wavefront shaping quantum light. This corresponds to an overall mode transmission of the order of 1%, based on the total number of speckle spots of order 10^3 and the 30-fold enhancement. Based on energy conservation and the high purity of our photon source, the detected coincidences occur when the incident wavefront and the optimized target speckle spot contained a single photon.

6.4. Discussion

We have increased the probability that a single photon arrives at a desired speckle spot by using a phase mask optimized for classical light. Our experiment demonstrates that this method works. The intensity enhancement for the incident laser

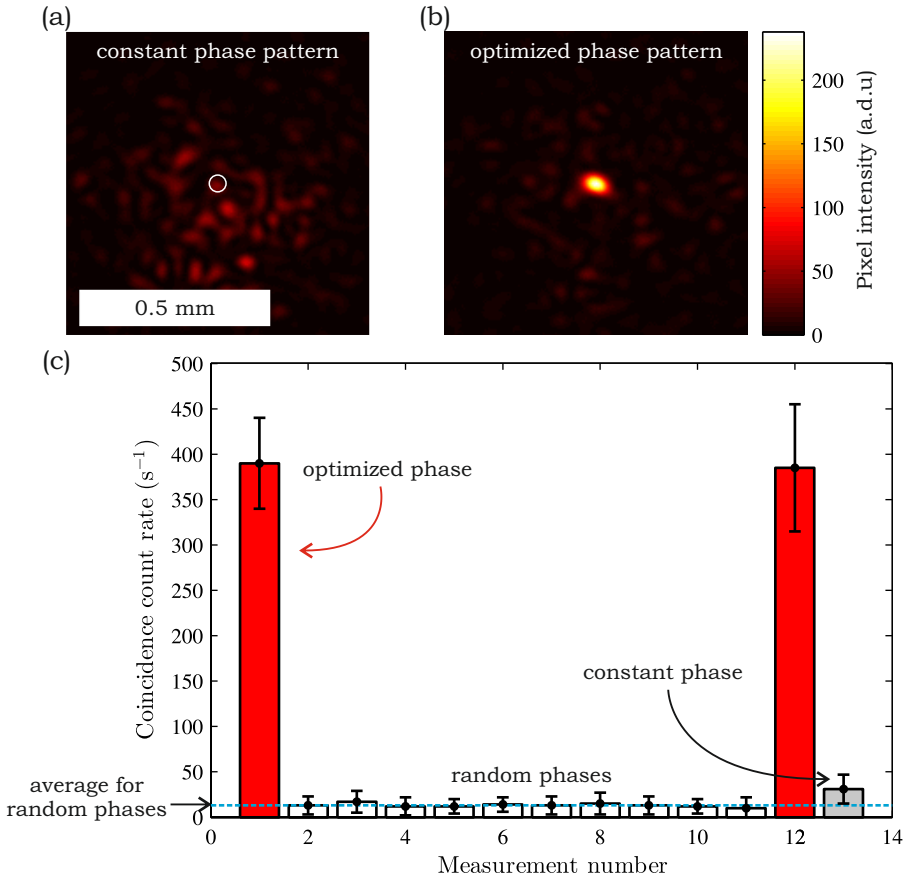

Figure 6.3. Wavefront-shaped single-photon speckle. (*a*) Speckle pattern imaged on a CCD camera for classical laser pulses with a random phase pattern. The circle indicates the target for optimization. (*b*) Speckle pattern with a single enhanced mode for an optimized phase pattern. (*c*) Measured coincidence count rate at the position of the bright speckle spot in (*b*) for an optimized (red), constant (gray) and random phase patterns (white). The blue dashed line represents the average coincidence rate measured for random phase patterns. The error bars are taken as 2 times the standard deviations.

pulses, which is in the order of $\eta = 30$, is mainly limited by the optimization algorithm we have implemented. There are algorithms that work faster and more efficiently resulting in optimized speckles of higher intensity [185]. At the moment of writing this dissertation, these algorithms are being modified, already showing preliminary intensity enhancements that are improved by an order of magnitude.

In addition, the enhancement is reduced by the broad spectrum of the laser that

restricts the path lengths that can constructively interfere to the optimized speckles [63]. Wavefront-shaping experiments with continuous-wave classical light have shown intensity enhancements $\eta > 10^3$ [26]. In principle, SPDC could be pumped by continuous-wave light, resulting in photons with a longer coherence length. We expect that the enhancement can be improved by increasing the temporal width of the photons by using, *e.g.*, 2-5 ps-pulses for the pump light, without sacrificing the possibility of creating quantum states on the two-photon level.

The spectrum of the alignment laser pulses and the prepared photons can be better matched using narrowband spectral filters, although this reduces the count rate by extinction losses. Instead of using the laser pulses for alignment of the single-photon wavefronts, one could seed the PPKTP crystal with the laser light to produce parametric amplification instead of SPDC, to find accurately the spatio-temporal mode of single photons in wavefront shaping [186].

If one can reduce the extinction losses of the system by at least an order of magnitude, by choosing, *e.g.*, a different disordered structure like a thinner layer of paint, the initial coincidence count rate for unoptimized speckles would already be in the order of 10^2 s^{-1}, making it in principle possible to directly wavefront shape single photons. On the other hand, our results demonstrate that the phase mask obtained for classical light is adequate for the single photons. Optimization with classical light simplifies addressing more advanced correlations for quantum interference, which have inherently a smaller intensity enhancement, see for example appendices B and C, or Ref. [81].

6.5. Conclusions

In summary, we have controlled single-photon propagation in opaque scattering media with phase-modulation of the incident light. This opens new opportunities to address elements of the scattering matrix to obtain desired quantum interference. Our findings are not limited to single-photon Fock states, but can be applied to non-classical light in general.

CHAPTER 7

Programming optical beam splitters in opaque scattering media

Wavefront shaping allows for ultimate control of light propagation in multiple-scattering media by adaptive manipulation of incident waves. Two orthogonal wavefront-shaped modes are incident on a layer of white paint to create two enhanced output speckle spots of equal intensity. We experimentally confirm by interference measurements that the output speckle spots are correlated like the two outputs of a balanced beam splitter. The observed deviations from the phase behavior of an ideal beam splitter are analyzed with a transmission matrix model. Our experiments demonstrate that wavefront shaping in multiple-scattering media can be used to program linear optical devices with multiple inputs and outputs.

7.1. Introduction

Linear optical components like lenses, mirrors, polarizers and wave plates are the essential building blocks of optical experiments [187, 188]. One has often little freedom to modify the linear optical circuit, besides rearranging components or including adaptive elements. For computational applications and on-chip light processing [24, 68, 189, 190], it would be fantastic to have a programmable linear optical circuit that can be controlled during operation. Randomness provides an excellent platform to accomplish this [60]. In wavefront shaping [26, 27] incident light is modulated by a spatial light modulator to obtain a desired speckle pattern for functionality. Although one has to tolerate high losses, this technique makes it possible to transform opaque scattering media in linear optical elements that are flexible in performance [62–65, 191, 192]. If one controls light propagation inside strongly scattering media, one can make the most exotic linear optical circuits within a fraction of a mm^3.

In earlier reported wavefront-shaping experiments, multiple target speckle spots have been simultaneously optimized with a single incident wavefront [26, 65, 81]. These experiments essentially demonstrate $1 \times m$ linear optical circuits with 1 incident mode projected to m output modes. If one is capable to manipulate n incident modes with wavefront shaping, it becomes possible to program $n \times m$ optical circuits with a desired transmission matrix $\mathbf{T}$. To our knowledge, no experiment demonstrating this capability has been reported.

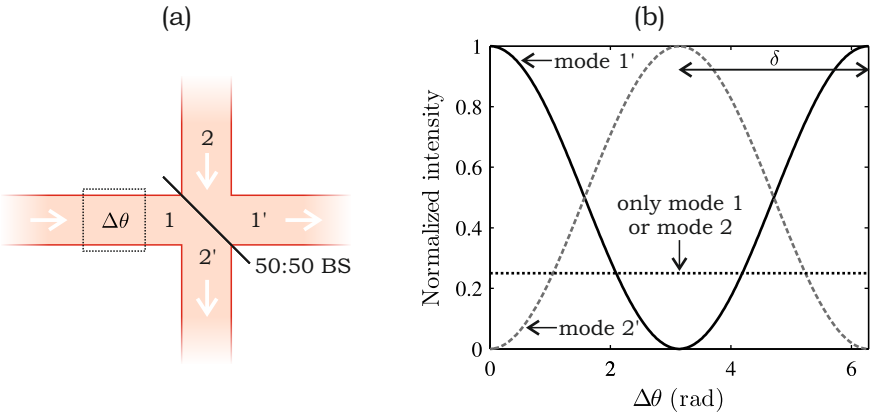

Figure 7.1. Interference at an ideal lossless 50:50 beam splitter. (*a*) Two incident modes $(1, 2)$ with equal intensity interfere at a 50:50 beam splitter (BS) resulting in two output modes $(1', 2')$. (*b*) Normalized intensity in the output modes as a function of relative phase shift $\Delta\theta$ applied to incident mode 1. All intensities are normalized to the total input intensity $I_1 + I_2$.

In this chapter we describe an experiment in which a layer of white paint is made to behave as an optical beam splitter. We apply wavefront shaping to optimize 2 output speckle spots for 2 separate incident modes, forming a 2×2 optical circuit. The optimized speckles are correlated like the outputs of a 50:50 beam splitter. This behavior is verified by an optical interference experiment. Our measurements indicate that the speckles become more correlated like a beam splitter when the intensity enhancement η increases. This surprisingly suggests that one can program beam splitters without prior measurement of the transmission matrix $\mathbf{T}$. We explain this with random matrix calculations. Our experiment demonstrates that wavefront shaping can be extended to multiple incident modes that can interfere in a controlled manner, allowing for programmable linear optical circuits.

7.2. Interference on a beam splitter

The scattering matrix of a lossless beam splitter represents a unitary transformation that can be written in its most general form as the product of three matrices [193]:

$$\mathbf{S} = \begin{bmatrix} e^{i\frac{\Psi}{2}} & 0 \\ 0 & e^{-i\frac{\Psi}{2}} \end{bmatrix} \begin{bmatrix} \cos\frac{\Theta}{2} & \sin\frac{\Theta}{2} \\ -\sin\frac{\Theta}{2} & \cos\frac{\Theta}{2} \end{bmatrix} \begin{bmatrix} e^{i\frac{\Phi}{2}} & 0 \\ 0 & e^{-i\frac{\Phi}{2}} \end{bmatrix}. \tag{7.1}$$

The nonzero terms in the first and last matrix are phase differences Ψ and Φ applied by the beam splitter on the incident and outgoing modes[1] respectively.

[1] In this chapter we use the term input mode for an incident wave that describes a single input of the normal beam splitter or wavefront-shaped beam splitter.

The phase angle Θ in the center matrix determines the splitting ratio, which has to be $\Theta = (2n+1)\pi/2$ for a 50:50 beam splitter, with n an integer value.

Now consider the experiment in Fig. 7.1(a) in which two modes $(1, 2)$, containing coherent light of equal intensity, are incident on a 50:50 beam splitter giving two output modes $(1', 2')$. The relative phase difference $\Delta\theta$ between mode 1 and 2 can be controlled; this is the same as controlling $\Phi = \Delta\theta$ in Eq. (7.1). The intensity $I_{1'}, I_{2'}$ as a function of $\Delta\theta$ is shown in Fig. 7.1(b). $I_{1'}$ and $I_{2'}$ will oscillate with a phase difference of $\delta = \pi$ for the ideal lossless beam splitter, independent of phases Φ and Ψ in Eq. (7.1). For this graph we have set $\Psi = 0$ and used $\Delta\theta = \Phi$. Any nonzero value for Ψ will provide a phase offset to both the output modes, essentially shifting both $I_{1'}$ and $I_{2'}$ along the horizontal axes by the same amount. Note that energy is conserved: $I_{1'} + I_{2'} = I_1 + I_2$, and a fringe visibility of 100% is observed. If one of the incident modes is blocked, a constant intensity is detected in both output modes that is 4 times lower than the maximum intensity in one of the output modes when both inputs are present.

Modelling lossy beam splitters is an interesting subject on its own with a wide variety of approaches [194–198]. We describe the effective transmission matrix $\mathbf{T}$ as a non-unitary version of Eq. (7.1). The phase difference $\delta = \pi$ will still hold if there are losses in any of the input or output modes. In such a case, the damping can be modelled in the left or right matrix in Eq. (7.1) by making them non-unitary with a determinant smaller than 1. This is valid for the typical beam splitter one uses. However, when the scattering in the beam splitter does not conserve energy (the damping is in the center matrix in Eq. (7.1) dictating that not all energy goes to the output modes), δ could in principle take on any value as long as the total output intensity does not exceed the total input intensity. To model the most general form of a lossy beam splitter we make the following assumptions:

Assumption 1 *The system is described by an effective transmission matrix* $\mathbf{T}$ *consisting of* 2×2 *elements.*

Assumption 2 $\mathbf{T}$ *provides an equal intensity splitting ratio.*

Assumption 3 *The intensity losses for both input modes are identical.*

The system behaves as a lossy beam splitter with equal splitting ratio. For convenience to compare to the ideal beam splitter, we consider that a single input mode is reflected with intensity reflectance $|r|^2$ and transmitted with transmission $|t|^2$. For a lossy beam splitter this means $|r| = |t|$ and $|r|^2 + |t|^2 \leq 1$. We relate the input amplitudes to the output amplitudes as $A_1 \rightarrow |r|(A_{1'} + e^{i\phi_1}A_{2'})$ and $A_2 \rightarrow |r|(e^{i\phi_2}A_{1'} + A_{2'})$, with phase terms ϕ_1 and ϕ_2. Now we set $|r|^2 = 1/N$, with splitting factor N and $N \geq 2$. This leads to the following transmission matrix:

$$\mathbf{T} = \frac{1}{\sqrt{N}} \begin{bmatrix} 1 & e^{i\phi_1} \\ e^{i\phi_2} & 1 \end{bmatrix}. \tag{7.2}$$

For the ideal lossless 50:50 beam splitter, $\mathbf{T}$ is only unitary when $N = 2$, with for example $\phi_1 = \phi_2 = \pi/2$, and would always result to interference as shown in

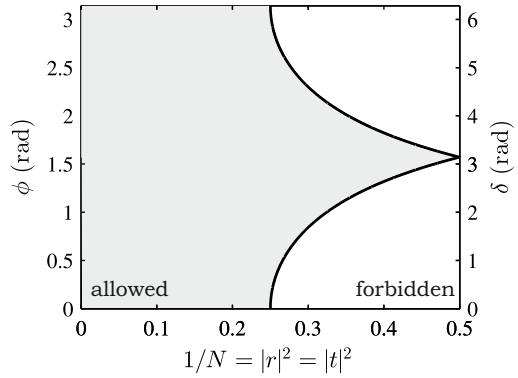

Figure 7.2. The allowed phase difference ϕ and δ as a function of reflectivity $|r|^2$ for the balanced beam splitter.

Fig. 7.1(*b*). The eigenvalues λ_1 and λ_2 of Eq. (7.2) are:

$$\lambda_1 = \frac{1 + e^{i\frac{\phi_1+\phi_2}{2}}}{\sqrt{N}}, \quad \lambda_2 = \frac{1 - e^{i\frac{\phi_1+\phi_2}{2}}}{\sqrt{N}}. \tag{7.3}$$

Next we make the substitution $\phi = (\phi_1 + \phi_2)/2$. The observed phase difference in an interference experiment is given by $\delta = \phi_1 + \phi_2 = 2\phi$. Since $\mathbf{T}$ is a square matrix, from the singular values of Eq. (7.2) $\tau_1^2 = |\lambda_1|^2 = (2 + 2\cos(\phi))/N$ and $\tau_2^2 = |\lambda_2|^2 = (2 - 2\cos(\phi))/N$ we obtain:

$$\tau_1^2 + \tau_2^2 = \frac{4}{N}. \tag{7.4}$$

If this relation is fulfilled, one guarantees that $|r|^2 = |t|^2$. In addition $\tau_1, \tau_2 \leq 1$ to guarantee a transmission not exceeding 1. This restricts the possible ϕ to be in the range between $\cos^{-1}(N/2 - 1) \leq \phi \leq \cos^{-1}(1 - N/2)$ for $2 \leq N \leq 4$, as marked by the gray area in Fig. 7.2.

With wavefront shaping it is possible to use a multiple-scattering material as a balanced beam splitter, which is inherently lossy. In our experiment we are working with $N \gg 10^2$ and therefore any ϕ and θ are allowed. The scattering statistics of the sample, such as the the singular value distribution, and the intensity enhancement defining N in Eq. (7.4), determine the combination of τ_1 and τ_2 that satisfy Eq. (7.4). Therefore one would not expect in general a constant probability distribution for δ in the gray marked area in Fig. 7.2. We would like to approximate the behaviour of a beam splitter where $\delta \to \pi$ since this mimics the beam splitter one normally uses.

7.3. Optimization algorithm

The optimization procedure for wavefront-shaped balanced beam splitters is illustrated in Fig. 7.3. We start with a single incident mode. All segments of a

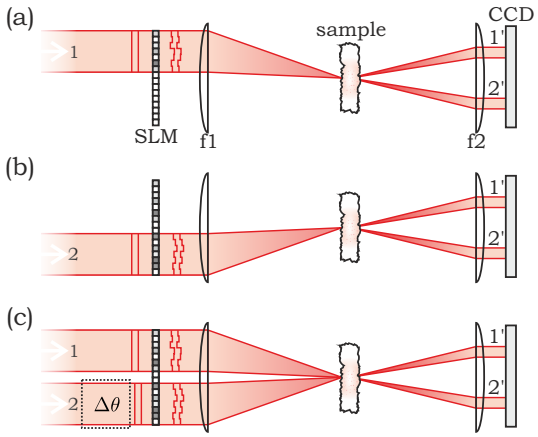

Figure 7.3. Optimization procedure for wavefront-shaped balanced beam splitters. A single SLM is divided in two sections to phase modulate incident modes 1 and 2 that are spatially separated. (*a*) Only mode 1 is incident and mode 2 is blocked. Two target speckles $1'$ and $2'$ are optimized on a CCD camera. (*b*) Only mode 2 is incident and mode 1 is blocked, and the same target speckles $1'$ and $2'$ are optimized. (*c*) Both modes 1 and 2 are incident on the SLM, using both optimized phase patterns. A relative phase differenced $\Delta\theta$ between mode 1 and 2 is applied with the SLM to confirm optical interference like in Fig. 7.1(*b*).

phase-only SLM are subsequently addressed. The phase $\phi_n \subset [0, 2\pi)$ of the n^{th} segment is randomly chosen and the output intensities $I_{1'}$ and $I_{2'}$ are monitored. ϕ_n is accepted and kept on the SLM if the summed output intensities of both spots has increased and the difference intensity has decreased:

1. $I_{1',\text{new}} + I_{2',\text{new}} > I_{1',\text{old}} + I_{2',\text{old}} + \epsilon_1$
2. $|I_{1',\text{new}} - I_{2',\text{new}}| < |I_{1',\text{old}} - I_{2',\text{old}}| + \epsilon_2$

with positive tolerances $\epsilon_1, \epsilon_2 \to 0$ to compensate for noise. Otherwise the previous ϕ_n was restored. Next the $(n+1)^{\text{th}}$ segment is addressed, etc. After the final segment has been addressed, the entire optimization is repeated until the desired convergence is reached.

The same procedure is repeated for the second incident mode for the same two target spots. Finally both modes are incident to perform an interference experiment as described in Fig. 7.1, where the relative phase $\Delta\theta$ is controlled with the SLM.

We have decided to select this optimization algorithm because of ease of implementation and the guaranteed convergence to spots of equal intensity. There are algorithms that work faster and more efficiently resulting in speckles of higher

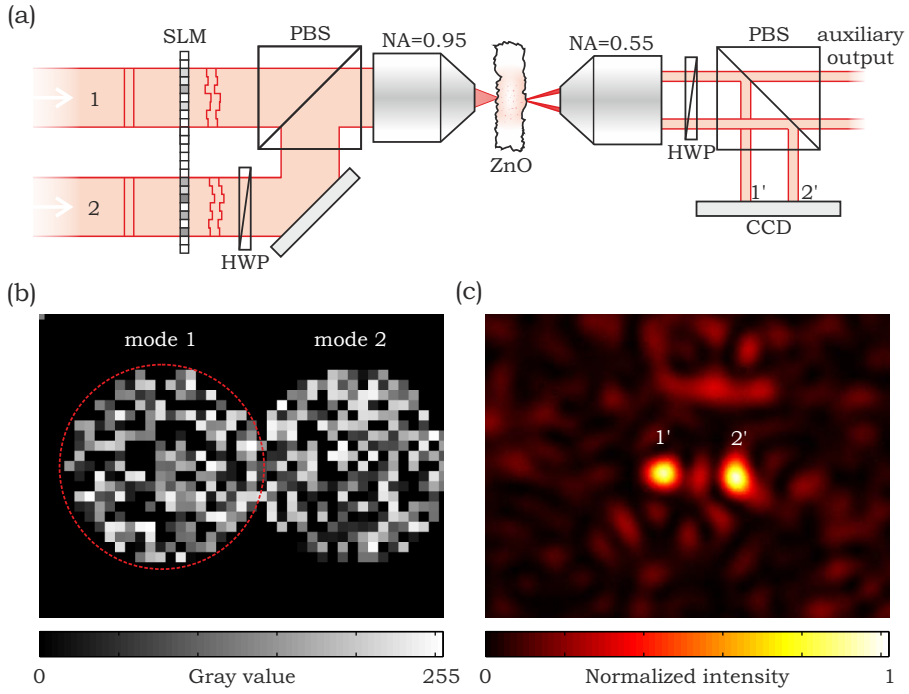

Figure 7.4. Setup for wavefront-shaped balanced beam splitters. (a) Two incident modes $(1, 2)$ are phase-modulated with a spatial light modulator (SLM). Both modes are spatially overlapped with a polarizing beam splitter cube (PBS). The modes are focussed on a layer of white paint (ZnO particles) that has been spray coated on a 1 mm thick microscope slide. The transmitted light is projected on a CCD camera. Two output modes $1'$ and $2'$ are selected. (b) Optimized phase pattern on the SLM. (c) Camera image for two optimized speckles when mode 1 is blocked.

intensity enhancement [185], see also appendix B and C. At any rate, in the next sections we demonstrate that our algorithm is adequate for this experiment.

7.4. Experimental setup

The setup is illustrated in Fig. 7.4(a). The light source is a mode-locked Ti:Sapphire laser (Spectra-Physics, Tsunami) emitting transform-limited pulses at a repetition rate of 80 MHz with a pulse width of approximately 0.3 ps and a center wavelength of 790.0 nm. The pulses are spectrally filtered by a Fabry-Perot cavity with a linewidth of 1.5 nm. The beam is split and coupled into two separate single-mode fibers. The output modes have identical polarization and

waist and form the input modes 1 and 2. The two modes are phase-modulated with a SLM (Hamamatsu, LCOS-SLM). The two modes are spatially overlapped with a half-wave plate (HWP) and polarizing beam splitter (PBS) cube, resulting in co-linear propagation of modes with orthogonal polarization. This allows us to completely fill the aperture of the objective (NA=0.95, Zeiss) that focusses the light on a layer of white paint. Both pulses arrive simultaneously at the sample to within 20 fs. We make sure that the intensity of both incident modes on the objective are identical (input power of approximately 0.5 mW per mode). The layer of white paint consists of ZnO powder with a scattering mean free path of 0.7 ± 0.2 μm. The layer is approximately 30 μm thick and spray painted on a glass microscope slide of 1 mm thickness. The transmitted speckle pattern is collected with a second objective (NA=0.55, Nikon) and imaged on a CCD camera after reflection on a PBS, see for example Fig. 7.4(c). The optimized speckles can be transmitted through the PBS, towards a different part of the setup for applications, by rotating the HWP.

The SLM was divided into segments of 20x20 pixels. Each segment was sequentially addressed with a random phase as described in the optimization algorithm. The phase is applied by writing a gray value between 0 and 255. This corresponds to a phase modulation depth of $(2.0 \pm 0.1)\pi$ rad. This algorithm was repeated approximately 15 times for all segments to obtain two enhanced speckles of equal intensity at $1'$ and $2'$, see Fig. 7.4(c). The total optimization procedure for both incident modes takes about 3 hours. We confirm interference between the output modes by adding a phase offset to the encircled area in Fig 7.4(b).

7.5. Experimental results

Fig. 7.5 presents the main result of this chapter: optical interference with a wavefront-shaped nearly balanced beam splitter. Fig. 7.5(a) shows a series of camera images when on incident mode 1 a phase offset is applied. The number in the left top corners represent the phase offset $\Delta\theta$ in gray values. All pictures are subsequently taken with the same integration time. The intensity clearly oscillates between the two target spots.

Fig. 7.5(b) shows the intensity $I_{1'}$ (red squares) and $I_{2'}$ (blue diamonds) as a function of the applied phase difference $\Delta\theta$. Both curves show sinusoidal behaviour and are approximately out-of-phase, mimicking the behaviour of an ideal beam splitter as is shown in Fig. 7.1(b). We expect an error in the phase of about $\Delta(\Delta\theta) = 0.1$ rad due to interferometric stability during data collection and an additional systematic error of 0.1 rad due to phase calibration (both not shown). We have fitted two functions of the form $A\sin(\Delta\theta + b) + c$ to the measured intensity, which is in good agreement with the data points. From b we determined the phase difference $|\delta| = 2.30 \pm 0.14$ rad, close to but significantly different from the value of $\delta = \pi$ of an ideal beam splitter. Both $I_{1'}$ and $I_{2'}$ show a fringe visibility of approximately 100%, which indicates a near-perfect mode matching between the output modes for the two seperate incident modes. The maximum measured intensity in both spots is approximately the same to within 5%. When one of

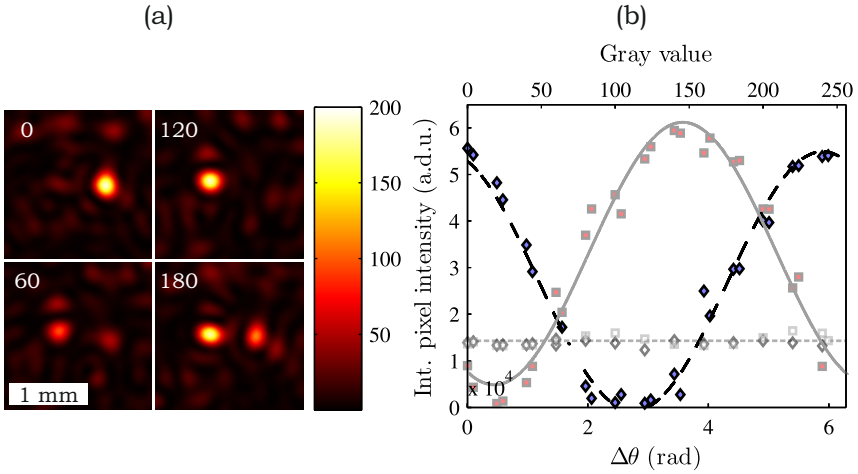

Figure 7.5. Interference between two optimized speckles of a wavefront-shaped beam splitter. A phase shift is applied on one of the incident modes by applying an offset to the phase pattern of the SLM. (*a*) Camera images for different phase offsets $\Delta\theta$ expressed as gray values. (*b*) Intensity in the two optimized speckles (red squares and blue diamonds) as a function of gray value offset. The solid and dashed lines are sinusoidal fits. When only one incident mode is present, a constant intensity in both target speckles is observed (white diamonds and white squares).

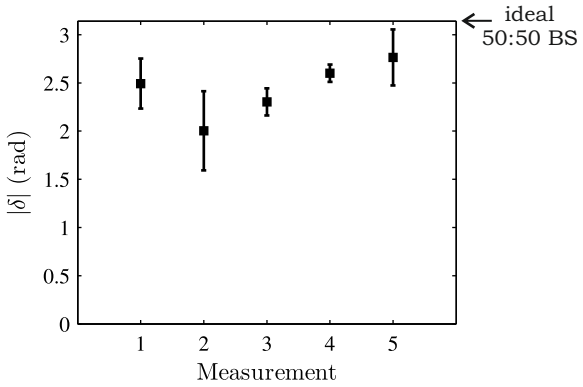

Figure 7.6. Measured phase difference $|\delta|$ for different realizations of the wavefront-shaped balanced beam splitter.

the incident modes is blocked in the interference experiment, the output intensity is approximately constant (white diamonds and squares). The small spatial separation between mode 1 and 2 on the SLM gives a small crosstalk, causing fluctuations within 10%. The output intensity is approximately 4 times lower as the maximum intensity when both modes are incident, in excellent agreement with Fig. 7.1(b).

We have repeated this interference experiment 5 times for different target speckle spots and determined $|\delta|$. The result is shown in Fig. 7.6. All measurements were performed under comparable circumstances. Although the number of measurements are not sufficient for any statistical relevant conclusion, our measurements suggest a tendency for $|\delta|$ to cluster close to π. In the next section we present a model that simulates this behavior.

7.6. Model for the phase difference

In this section we model the observed phase difference δ in the interference experiment based on random matrix theory. Light undergoes isotropic multiple scattering in a sample with a thickness much larger than the scattering mean free path l and $kl \gg 1$. We therefore expect the transmission matrix to follow the statistics of a random matrix, as was demonstrated experimentally for ZnO by Popoff *et al.* [81]. One could argue that $\mathbf{T}$ is a subset of the scattering matrix $\mathbf{S}$, and therefore ϕ_1 and ϕ_2 can take in principle any value between $[0, 2\pi)$ with equal probability. This would naively result in a constant probability distribution for δ, which is not observed.

The scattering matrix $\mathbf{S}$ has to be unitary, which sets restrictions on the allowed values for each element $s_{a,b}$. Consider a random $\mathbf{S}$ in a basis where one input mode is one element of the input vector and one target output speckle spot is one element of the output vector. If $\mathbf{S}$ contains a beam splitter of equal splitting ratio, there have to be 2 rows and 2 columns in $\mathbf{S}$ with corner elements of approximately

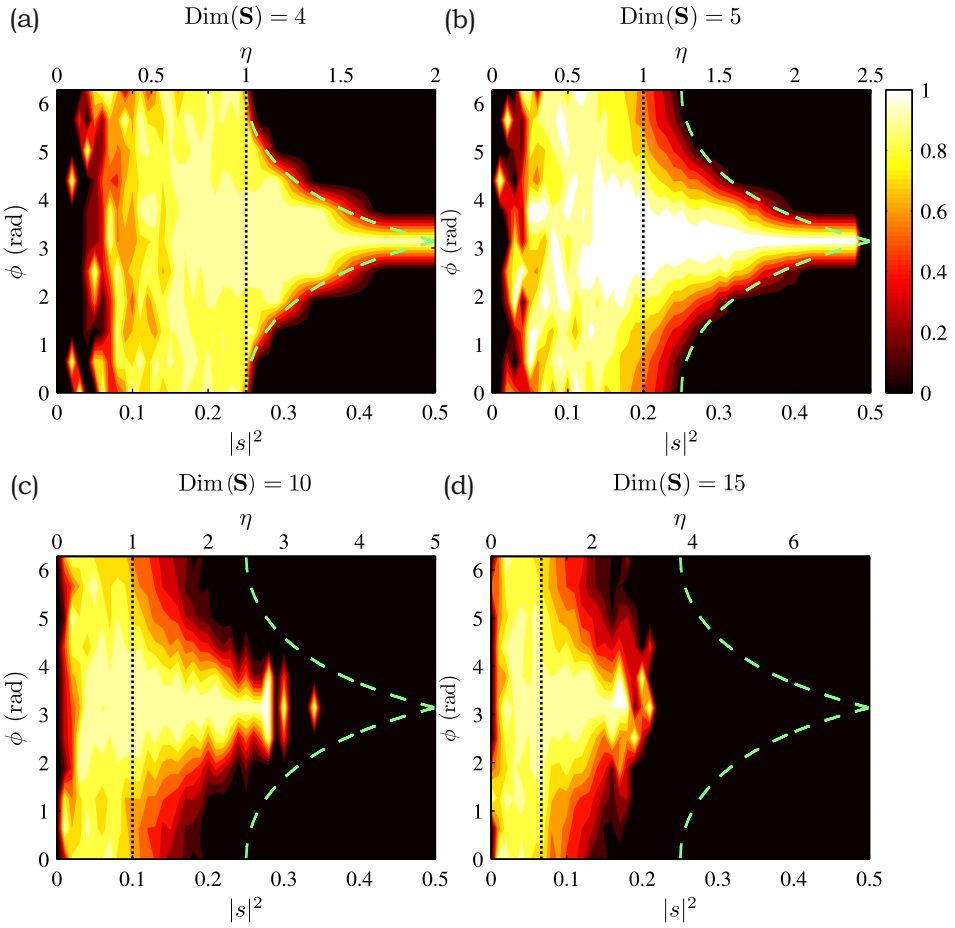

Figure 7.7. Calculated normalized probability distribution for the phase difference δ for random scattering matrices S with different Dim(**S**) **containing balanced lossy beam splitters.** All 4 elements in the scattering matrix that form the beam splitter have an equal amplitude within 1% to be accepted. The green dashed line represents the boundary of allowed and forbidden phases as in Fig. 7.2. The black vertical dashed line represents $\langle |s_{a,b}|^2 \rangle$.

the same amplitude:

$$|s_{i,j}| = c_1 \, |s_{i+n,j}| = c_2 \, |s_{i,j+m}| = c_3 \, |s_{i+n,j+m}| \tag{7.5}$$

with i, j, m, n positive integers and $c \approx 1$. For a random scattering matrix with dimension Dim(**S**) = 2, the only possibility for a balanced beam splitter is that $\delta = \pi$. From matrix algebra it follows that for Dim(**S**) = 3, δ can only lie on the boundary lines of the gray area of Fig. 7.2 and the amplitude coefficients of **S** should satisfy $|s_{a,b}|^2 \geq 1/4$. For Dim(**S**) ≥ 4 any phase becomes accessible within

the gray marked area of Fig. 7.2. However, the corresponding phase distribution is strongly dependent on Dim(**S**), as illustrated in Fig. 7.7. There we have generated many random scattering matrices with different dimension that contain a balanced beam splitter. The corresponding intensity enhancement is given by $\eta = |s|^2 / \left\langle |s_{a,b}|^2 \right\rangle$, with $|s|^2 = (1/4)(|s_{i,j}|^2 + |s_{i+n,j}|^2 + |s_{i,j+m}|^2 + |s_{i+n,j+m}|^2)$, and $\left\langle |s_{a,b}|^2 \right\rangle = 1/\mathrm{Dim}(\mathbf{S})$. An increased probability for $\delta = \pi$ is observed with higher η. The probability distribution becomes flat for small η. How this scales depends strongly on Dim(**S**). It becomes extremely difficult to observe $\eta > 4$ for $\left\langle |s_{a,b}|^2 \right\rangle < 0.01$, because the probability to get these realizations out of random unitary matrices becomes astronomically small. Our experiment is described by this situation.

Therefore we have simulated our experiment by applying our optimization algorithm on large random **S**. Fig 7.8 shows the observed distribution for $|\delta|$ as a function of intensity enhancement η. The main observation is that $\mathrm{P}(|\delta|)$ has a global maximum at $|\delta| = \pi$ that increases with η.

The simulations in Fig. 7.8 are performed for $\mathrm{Dim}(\mathbf{S}) = 300$. We control the phase of 40 input elements representing incident mode 1, and 40 input elements representing incident mode 2. Each controlled input element has a normalized input intensity of 1. We have set $\epsilon_1 = 0$ and $\epsilon_2 = 0.001$. We apply the optimization algorithm 2500 times per mode to guarantee convergence. We select output elements for which the total intensity of the optimization for mode 1 is within 10% of the optimization for mode 2, approximating our experiment. The intensity enhancement η is given by the observed intensity in a target speckle, divided by $\left\langle |s_{a,b}|^2 \right\rangle = 40/\mathrm{Dim}(\mathbf{S})$, where the factor 40 comes from the number of channels that are controlled per incident mode.

It is beyond the scope of this model to match experimental conditions. In particular the large number of channels is difficult to implement. We have repeated our simulations for several Dim(**S**) and several amounts of controlled input channels, always demonstrating a global maximum at a $|\delta| = \pi$ that increases with η. This demonstrates that the two optimized speckle spots approximate better the behavior of a balanced beam splitter with increasing enhancement, using our optimization algorithm. Based on the model with large unitary matrices, it is likely that this is independent of the type of optimization algorithm used.

7.7. Discussion

We have experimentally created two optimized speckle spots that are correlated like the output of a lossy balanced beam splitter. The interference experiment suggests that $|\delta| \to \pi$ with increasing η, which is indicated by a computational model. The model could not match the dimension of our experiment, nevertheless, the agreement is gratifying. Our model demonstrates that the probability distribution for ϕ depends on the number of modes in the system. It would be intriguing to perform these kind of experiments with systems of lower dimension, such as, multi-mode fibers with embedded disorder to confirm this scaling [199].

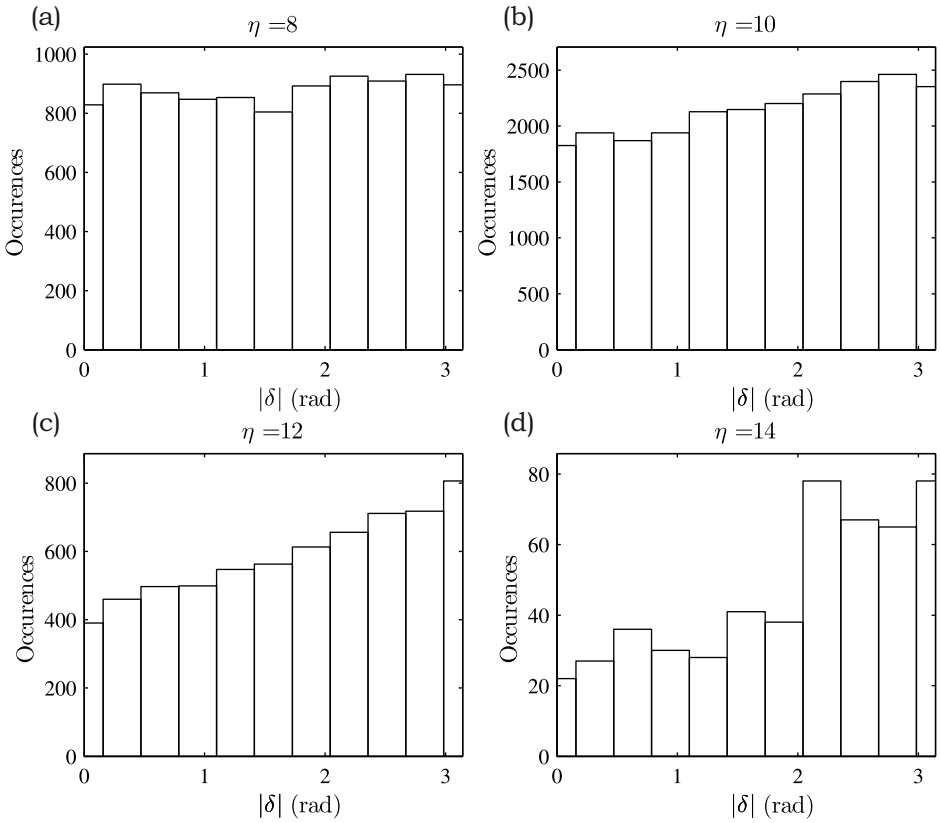

Figure 7.8. Simulated phase difference $|\delta|$ for the balanced beam splitter for different intensity enhancements η. The probability that $\delta \to \pi$ increases with η. (*a*) Realizations with $7.5 \leq \eta < 8.5$. (*b*) Realizations with $9.5 \leq \eta < 10.5$. (*c*) Realizations with $11.5 \leq \eta < 12.5$. (*d*) Realizations with $13.5 \leq \eta < 14.5$.

It would be fascinating to measure the transmission matrix of the sample prior to optimization. This allows for an experimental study on the influence of the optimization algorithm and η on the observed δ. In addition this would also allow to address speckle patterns with more complicated correlations.

The loss in our experiment can be reduced by several orders of magnitude by implementing more efficient wavefront-shaping procedures and using continuous wave lasers. On the other hand, our pulsed experiment reveals the opportunity to apply this beam splitter on incident light produced in nonlinear processes, such as entangled photon pairs or higher order quantum states produced with spontaneous parametric down-conversion [181]. This makes it possible to program linear optical circuits for incident quantum states to exploit quantum correlations in disordered media [16, 17, 19–21, 72, 74, 75].

7.8. Conclusions and outlook

In summary, we have controlled light propagation in opaque scattering media with phase modulation of the two incident light modes. We have optimized two speckles that show interference like a 50:50 beam splitter.

Advanced optimization algorithms make it possible to create more complicated linear circuits out of multiple-scattering media. In appendix B we present an algorithm that allows making arbitrary $n \times m$ linear optical circuits without the need of measuring a transmission matrix of the multiple-scattering medium. Based on this algorithm, we find an upper limit for the average energy transmission of the wavefront-shaped beam splitter, which is on average 17:17, instead of 50:50 for the ideal beam splitter. The calculations are presented in appendix C.

CHAPTER 8

Summary and outlook

In this dissertation experimental results are presented on controlling light with photonic systems. The first part describes research on forbidden zones of light: frequency gaps in photonic crystals. Polarization-resolved and position-dependent reflectance spectroscopy on silicon two- and three-dimensional photonic crystals revealed broad stop bands with record-high reflectivity exceeding 60%, indicating the excellent quality of these structures. It would be intriguing to modify these photonic structures with defects to form, *e.g.*, waveguides and cavities, which could be studied with the described methods. Polarization-resolved measurements in a different polarization basis, such as circular polarized light, could be used to investigate if the current geometry sustains chirality, or can be modified to address specific polarization states.

A general diffraction phenomenon, called sub-Bragg diffraction, has been discovered and explained. In sub-Bragg diffraction, gap formation occurs in a high-symmetry direction by multiple-Bragg diffraction at a lower frequency than the well-known simple Bragg diffraction. Sub-Bragg diffraction is essential for the formation of the two-dimensional band gap for TE-polarized light in triangular photonic crystal slabs. Sub-Bragg diffraction occurs for general wave propagation in 2 out of the 5 two-dimensional Bravais lattices and 7 out of 14 three-dimensional Bravais lattices. It would be intriguing to investigate sub-Bragg diffraction for lattices with controlled photonic strength with, *e.g.*, reflectance spectroscopy or phase-sensitive near-field microscopy. Sub-Bragg diffraction is predicted to give rise to stop gaps for phonons and electrons, and therefore it would be interesting to investigate its influence on, *e.g.*, the specific heat of materials, the melting temperature of ice, or relativistic electron propagation in graphene.

Angle-averaged, polarization-resolved and position-dependent spectra reveal a common stop band of up to 16% gap-to-midgap frequency ratio for inverse woodpile photonic crystals, forming a strong experimental signature of the presence of a complete photonic band gap. The presence of the band gap was confirmed with the observation of inhibited emission rates of embedded quantum dots [47]. Novel experiments on controlling vacuum fluctuations in photonic band gap crystals are expected in the near-future to study, *e.g.*, light emission near the band edge and inside the gap, investigate the influence of the finite crystal size, control black body radiation, manipulate Förster energy transfer [200], and study the impact of ordered and disordered defect states on propagation.

It would be fascinating if photonic crystals could be fabricated of GaAs or GaP, which have a refractive index comparable to silicon. This would bring

gaps to visible wavelengths and gives the opportunity to grow, and interact with, quantum dots inside the structures. This opens experiments with high efficiency silicon single-photon detectors. If the three-dimensional crystals could be created with layer-by-layer methods, such as has been done for woodpile crystals [201], it becomes possible to position defects and emitters, and increase the size of the structure.

The second part of this dissertation presents experiments on light propagation near the band edge in GaAs photonic-crystal waveguides. Phase-sensitive near-field microscopy (NSOM) was used to map light propagation with sub-wavelength resolution, revealing periodic field patterns consisting of superpositions of optical Bloch modes. A Bloch mode reconstruction algorithm was tested to extract and study individual Bloch modes. It is expected that this algorithm can be extended to general wave diffraction in any planar periodic structure.

In the slow-light regime, the periodic field patterns are perturbed by Anderson-localized modes that form due to random multiple-scattering on intrinsic disorder. A detailed dispersion relation has been measured for a specific photonic-crystal waveguide, where the localized modes smear out the band edge starting from a group index of 37. The observed localized modes are excited by TM-like propagating modes, allowing detection of localized modes far away from the excitation facet. A method was introduced to reconstruct the density of optical states (DOS), constituting to the first experimental demonstration of an optical Lifshitz tail. Ensemble averaging allows for a quantitative study of the Lifshitz tail.

The Lifshitz tail has been recently observed by probing the DOS with embedded quantum dots [173]. Embedded quantum dots only probe the field inside GaAs at fixed locations, which makes the DOS reconstruction with NSOM a powerful alternative since its ability to pick up the evanescent light everywhere. Since both propagating and localized modes can be observed with NSOM, it would be intriguing to map these modes on embedded quantum dots. Important properties of the field modes that interact with the emitter can be extracted, like the mode volume and polarization.

Polarization-resolved phase-sensitive NSOM would allow for a better understanding of the observed field pattern and a more accurate reconstruction of the DOS. Since the presence of the near-field tip is known to alter especially linewidths of resonances, it would be intriguing to use non-invasive measurements to study these localized modes, with for example phase-sensitive angle-resolved far-field imaging [202].

Cathodoluminescence has been used to reconstruct far-field radiation patterns and the local density of states in nanophotonic structures [203]. Although this method does not yet provide phase-information, and gives little control of the excited polarization states, it seems suitable to map the Anderson-localized modes. One would not need to rely anymore on a weak coupling with the propagating TM-like modes, or to measure close to the sample edge, to observe the localized modes. In addition, this would give direct access to permanently modify the structure with electron or ion beam milling. The imaging quality of the topog-

raphy with an electron or ion beam is in practice better than with NSOM, since one does not rely on shear-force feedback of a tip in contact. This technique could be suitable to point out the source of disorder.

The refractive index of GaAs can be reversibly controlled by light via the intensity dependent refractive index, and therefore in principle an intensity pattern can be written on top of the structure to locally modify the refractive index to, *e.g.*, compensate for disorder. The presence of a near-field tip would significantly hamper the accessibility for projecting this intensity pattern, but far-field imaging techniques such as transmission measurements, out-of-plane scattering, and cathodoluminescence, provide better access to the structure.

The third part of this dissertation describes experiments towards adaptive quantum optics. A high-rate entangled-photon source was developed based on type-II spontaneous parametric down conversion. Single-photon propagation in multiple-scattering media has been controlled with wavefront shaping. The probability that a photon arrives at a target output speckle spot after propagation through a layer of white paint has been increased 30-fold. This number can be improved by increasing the temporal width of the pump laser driving the spontaneous parametric down-conversion (SPDC), and using more advanced wavefront-shaping algorithms. In the experiments the signal arm of SPDC has been phase-modulated. Fewer losses in the signal arm are expected if one modulates the conjugate arm, or the pump laser driving the SPDC [204]. It would be intriguing to analyze the optimized output speckle spot with, *e.g.*, Hong-Ou-Mandel interferometry to learn more about the spectral shape of the output photons, or to measure how long a photon travels through a disordered medium.

The phase patterns in the experiments were obtained by wavefront shaping classical light to simulate the field modes of the single-photon states. In principle, wavefront shaping could also be applied directly on the single-photon source if the amount of optical losses caused by uncontrolled and undetected channels is reduced. On the other hand, simulation of the spatiotemporal mode with classical light has proven to be suitable, allows for an interferometric measurement of the transmission matrix, and it is applicable on states with a higher photon number.

Wavefront shaping techniques on classical light have been successfully implemented to use opaque scattering media as a balanced optical beam splitter. This is the first demonstration of a multiple input and output wavefront shaping optimization. Our experiment could be extended to incident single-photon states to observe a Hong-Ou-Mandel dip with the wavefront-shaped beam splitter, which is planned for the near future. This work will be extended to program quantum interference in disordered photonic media in general, forming the essence of adaptive quantum optics.

Using random scattering media described by scattering matrices of lower dimension, such as disordered multi-mode fibers, would reduce optical losses caused by uncontrolled and undetected channels. If these systems support the desired linear optical circuit, one can attach a phase mask directly on the incoupling facet to have a permanent integrated linear optical circuit optimized for the target correlation. This would be an optical multi-mode interference device based

on disorder.

It would be intriguing to exploit two-dimensional planar disordered structures for wavefront shaping optical circuits, such as a slab with randomly placed holes. With polarization- and phase-sensitive NSOM it becomes possible to measure the complex field anywhere in the structure, allowing for a mapping of the optical transfer function, resulting in, *e.g.*, wavelength-dependent transfer matrices. In addition, planar structures improve local accessibility via the out-of-plane dimension, enhancing local control of, *e.g.*, the refractive index, add or remove perturbations, and simplify structure design for coupling to other platforms like plasmonics or acoustics.

APPENDIX A

Extraction of individual Anderson-localized modes

In chapter 4 we have applied the Bloch mode reconstruction algorithm [140, 165] to decompose near-field patterns in propagating optical Bloch modes. Here we show a proof-of-principle result that one can apply this algorithm to extract individual localized modes. Localized modes are confined to a certain spatial region and therefore cannot be superpositions of propagating Bloch modes with real wave vectors. Figure A.1 shows a near-field pattern measured for a photonic-crystal waveguide with $r/a = 0.316 \pm 0.001$ and a near-field tip with an aperture of 170 nm. Figure A.1(a) shows the topography. One can easily identify the individual holes and the line defect. Figure A.1(b) shows the near-field pattern at $\lambda = 941.20 \pm 0.02$ nm. A localized mode (arrow) is observed that has higher amplitude than the propagating modes forming the background. The best fit consisting of propagating Bloch-modes is shown in Fig. A.1(c). When this best fit is subtracted from the original data set, the residual clearly highlights the localized mode in Fig. A.1(d).

Most of the near-field measurements contain many localized modes, hampering the algorithm to fit Bloch modes for decent subtraction. Nevertheless, we have repeated this procedure for 8 other near-field patterns consisting of a clear periodic background pattern with a localized mode, similar to Fig. A.1. We define the effective mode area[1] as $A = \int I(x,y)\mathrm{d}x\mathrm{d}y/\max(I(x,y))$, with $I(x,y)$ the intensity distribution in the waveguide. We find an upper limit for the average effective mode area of $A = (10 \pm 5)a^2$. The localized mode in Fig. A.1 has a mode area of approximately $10a^2$.

The amplitudes of the localized modes show the periodicity of the lattice within its confined region. It would be interesting to use a more advanced version of the Bloch mode extraction algorithm to fit the localized modes with Bloch modes that have complex wave vectors to include evanescent damping [140].

[1] This is a two-dimensional version of the *mode volume* defined by Ref. [205].

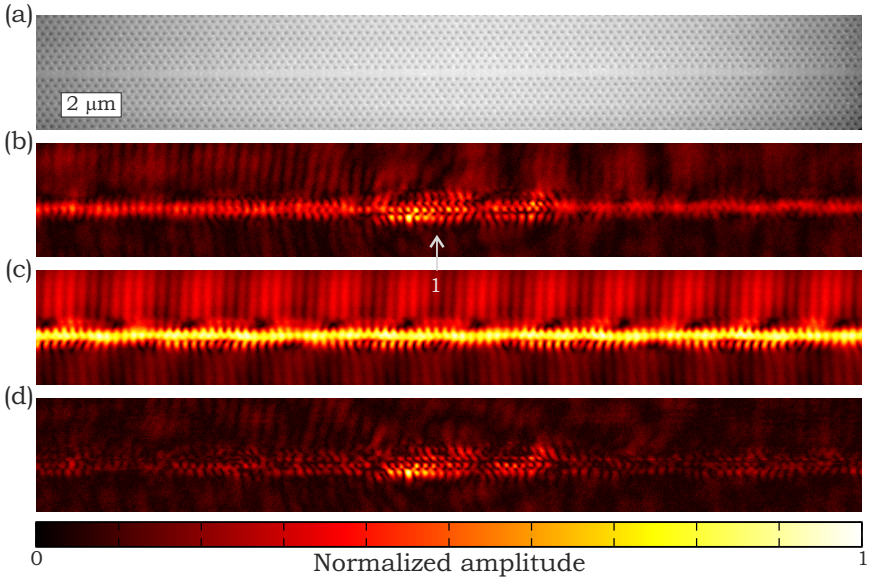

Figure A.1. Extracted Anderson-localized mode. (*a*) Topography of a photonic-crystal waveguide. (*b*) Measured amplitude at $\lambda = 941.20 \pm 0.02$ nm. (*c*) Reconstructed propagating Bloch modes. (*d*) Measured amplitude minus the reconstructed Bloch modes ((*b*)−(*c*)), revealing the localized mode. Amplitudes are normalized to the maximum amplitude in each figure.

APPENDIX B

Programmable linear optical circuits: the TomTom for light propagation in opaque scattering media

Random multiple-scattering media, such as white paint, contain correlations for light propagation that are very similar to correlations in complicated linear optical circuits with many input and output modes [60]. These correlations can be addressed by phase-modulation of the incident wavefronts [26, 27], which has led to the realization of many optical components out of disordered materials [62–65, 191, 192]. In principle one should be able to program the most exotic linear optical circuits within a fraction of a mm^3.

We propose and test an algorithm that allows for programming the effective transmission matrix $\mathbf{T}$ of a $n \times m$ linear optical circuit in a multiple-scattering material with phase-modulation of the incident light. The great advantage of our algorithm is that it can be directly applied to existing wavefront-shaping setups without the need of measuring a transmission matrix. One simply requires a phase-only spatial light modulator (SLM) and a CCD camera.

B.1. Algorithm

We propose an algorithm that is based on the linearity of the scattering process in a thick random scattering material. The algorithm is illustrated for a 2×2 linear optical circuit in Fig. B.1 and explained for the general $n \times m$ system below:

1. Start with an incident stationary wavefront on the SLM. The SLM is divided in n spatial segments to form the basis of the input modes. For simplicity we have illustrated in Fig. B.1 a single incident planar wavefront that is divided in incident modes by the SLM. Experiments presented in this appendix are performed in this manner. In principle the modes could already be separated before arrival on the SLM, as illustrated in Fig. 7.3. This will work if the phase difference between the incident modes is constant.

2. Optimize a target output speckle spot by phase modulation of the complete incident wavefront (all n modes are incident and have a fixed phase relation before arriving at the SLM). The complex field amplitude E_i' in the target

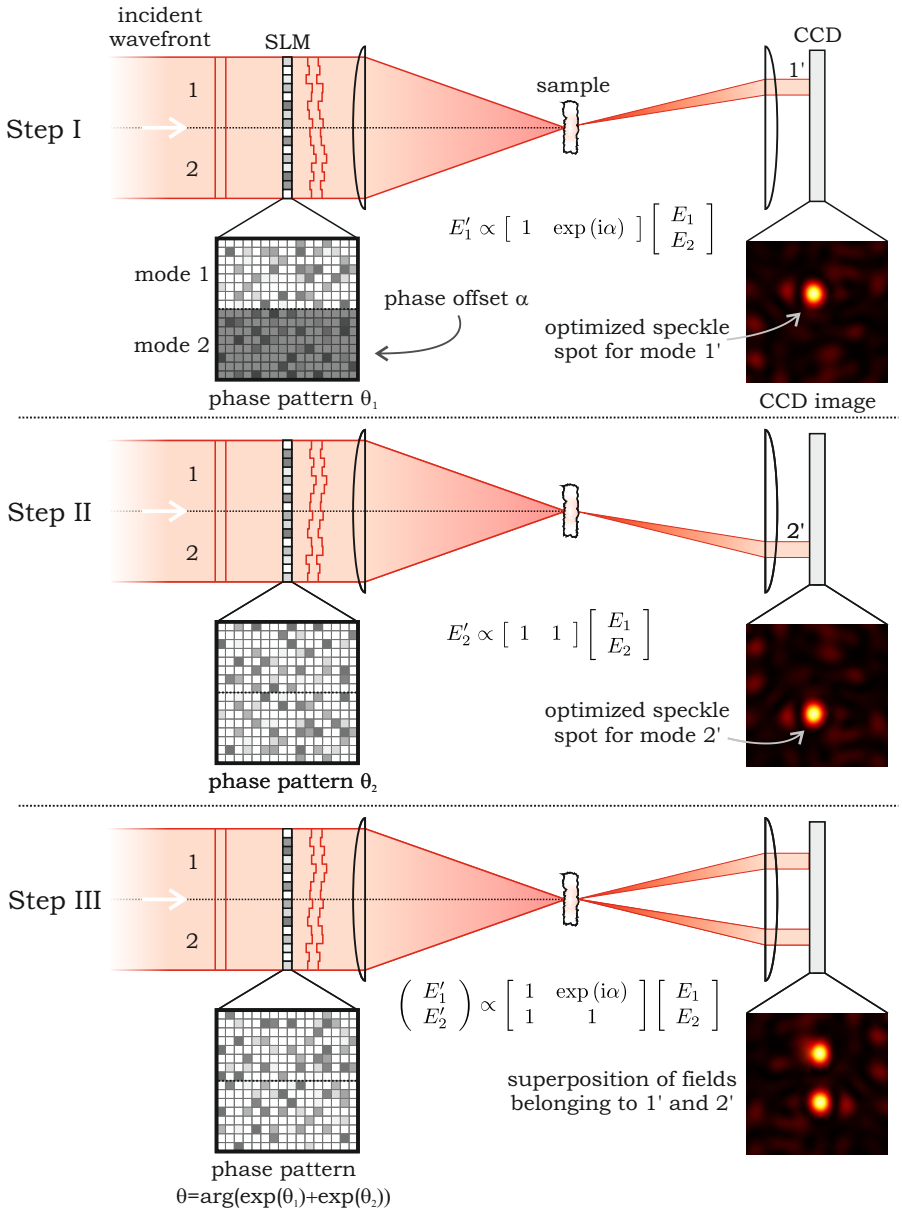

Figure B.1. Schematic illustration for programming a 2×2 linear optical circuit. The incident modes 1 and 2 are spatially separated on the SLM. (I) For optimization of output mode 1, one creates an optimized speckle spot with both modes incident. A permanent phase offset α is added to one of the incident modes to get a desired target field at the optimized speckle. (II) For optimization of output mode 2, one creates an optimized speckle spot that is orthogonal to the output speckle spot corresponding to mode 1. (III) Finally one writes phase pattern $\boldsymbol{\theta} = \arg\left(e^{i\boldsymbol{\theta}_1} + e^{i\boldsymbol{\theta}_2}\right)$ to obtain a superposition of the fields in steps I and II.

speckle spot is given by:[1]

$$E_i' = e^{\mathrm{i}\phi_i} \begin{bmatrix} a_{i,1} & a_{i,2} & \dots & a_{i,n} \end{bmatrix} \begin{bmatrix} E_1 \\ E_2 \\ \vdots \\ E_n \end{bmatrix}, \tag{B.1}$$

where ϕ_i is an overall phase factor with respect to a fixed reference, $a_{i,j}$ are real-valued transfer amplitudes, and E_j is the complex field amplitude of the j^{th} incident mode.[2] The transfer amplitudes $a_{i,j}$ are expected to be approximately equal for random isotropic scattering. The overall phase ϕ_i is often random and unknown in a standard wavefront-shaping setup, since only the intensity is monitored.[3]

3. A controlled phase offset $\phi_{i,j}$ is applied to each field mode E_j by writing a phase offset on the corresponding segment on the SLM. This gives a desired correlation for the row matrix that describes the transmission to E_i':

$$E_i' = e^{\mathrm{i}\phi_\mathrm{i}} \begin{bmatrix} a_{i,1}e^{\mathrm{i}\phi_{\mathrm{i},1}} & a_{i,2}e^{\mathrm{i}\phi_{\mathrm{i},2}} & \dots & a_{i,n}e^{\mathrm{i}\phi_{\mathrm{i,n}}} \end{bmatrix} \begin{bmatrix} E_1 \\ E_2 \\ \vdots \\ E_n \end{bmatrix}. \tag{B.2}$$

This row matrix forms a programmed $n \times 1$ transmission matrix. In principle each $a_{i,j}$ could be controlled by amplitude modulation of E_j, or by decorrelating the optimized phase pattern in the j^{th} segment. The complete phase pattern on the SLM, including all the phase offsets for each mode, are stored as phase pattern $\boldsymbol{\theta}_i$.

4. Repeat steps 2 and 3 $(m-1)$ times for $(m-1)$ optimized orthogonal target speckle spots to obtain different rows of the desired transmission matrix and store each corresponding $\boldsymbol{\theta}_i$.

5. Since the scattering process is linear and random,[4] one obtains the phase pattern $\boldsymbol{\Theta}$ for the desired transmission matrix by creating the superposition

[1] The subscript i is a label that is 1 for the first target speckle spot, with $i \leq m$.

[2] The subscript j is a label that is 1 for the first incident mode, with $j \leq n$.

[3] If the modes are already separated before arrival on the SLM, as shown in Fig. 7.3, small phase fluctuations between the incident modes are expected due to the stability of the setup, which can hamper the optimization of a target output speckle spot as described in step 2. This can be circumvented by first optimizing the target output speckle spot for incident mode 1 while all other incident modes are blocked. Next optimize the same speckle spot for incident mode 2, etcetera. Afterwards take the complete phase pattern for all incident modes and apply phase offsets to each incident mode to maximize the intensity of the target output speckle spot. This gives the same result as described by Eq. (B.1).

[4] The random scattering makes the phase patterns $\boldsymbol{\theta}_i$ approximately orthogonal. This requires the wavefront-shaping process to be efficient: ideally only one optimized speckle spot should be visible in step 2.

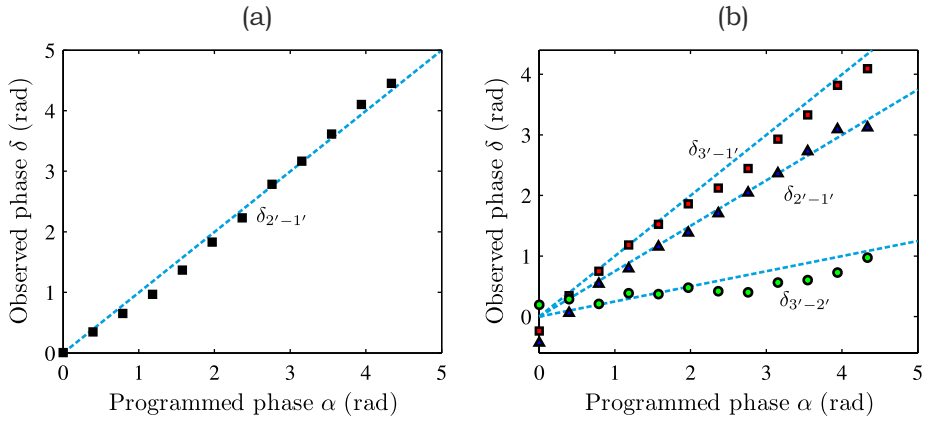

Figure B.2. Measured phase differences between target speckle spots in programmable 2×2 (*a*) and 2×3 (*b*) linear optical circuits. The symbols correspond to the observed phase difference $\delta_{s'-t'}$ between output modes s' and t', as a function of the programmed phase difference α. The blue dashed diagonal line corresponds to the expected target phase difference.

of the stored phase arrays $\boldsymbol{\theta}_i$:

$$\boldsymbol{\Theta} = \arg\left(\sum_{j=1}^{m}(c_j e^{i\boldsymbol{\theta}_j})\right), \tag{B.3}$$

with scaling factors $|c_j|$. One obtains a transmission matrix[5] of the form:

$$\mathbf{T} = \begin{bmatrix} c_1 & 0 & \dots & 0 \\ 0 & c_2 & & 0 \\ \vdots & & \ddots & \vdots \\ 0 & 0 & \dots & c_m \end{bmatrix} \begin{bmatrix} a_{1,1}e^{\mathrm{i}\phi_{1,1}} & a_{1,2}e^{\mathrm{i}\phi_{1,2}} & \dots & a_{1,n}e^{\mathrm{i}\phi_{\mathrm{i},\mathrm{n}}} \\ a_{2,1}e^{\mathrm{i}\phi_{\mathrm{i},2}} & & & a_{2,n}e^{\mathrm{i}\phi_{2,\mathrm{n}}} \\ \vdots & & & \vdots \\ a_{m,1}e^{\mathrm{i}\phi_{\mathrm{m},1}} & a_{m,2}e^{\mathrm{i}\phi_{\mathrm{m},2}} & \dots & a_{m,n}e^{\mathrm{i}\phi_{\mathrm{m},\mathrm{n}}} \end{bmatrix} \boldsymbol{\Phi}, \tag{B.4}$$

where the center matrix consists of the row elements that were programmed in steps 3 and 4, and contains the correlations of the desired $m \times n$ linear optical circuit. The right diagonal matrix $\boldsymbol{\Phi}$ contains the uncontrolled overall phase contribution of each incident mode, and can therefore be omitted.

[5] For convenience we have omitted the normalization constant for every transmission matrix in this appendix.

B.2. The programmable 2×2 and 2×3 transmission matrix

We first demonstrate the power of our algorithm by wavefront shaping a programmable 2×2 transmission matrix of the form:

$$\mathbf{T}_{2\times2} = \begin{bmatrix} 1 & e^{\mathrm{i}\alpha} \\ 1 & 1 \end{bmatrix}, \tag{B.5}$$

with controllable phase difference α. We use incident continuous-wave HeNe light (632.8 nm) on a ≈ 10 μm thick layer of white paint, spray painted on a glass microscope cover slide. An existing wavefront-shaping setup [61] was used for this experiment. An intensity enhancement η over 100 was observed for each individual speckle spot. We have performed identical experiments as described in Sec. 7.5 where the relative phase between the incident modes is controlled to perform an interferometric measurement of the effective transmission matrix. The results are shown in Fig. C.2(a) where the phase difference between the output modes is plotted as a function of the programmed phase difference α. An excellent agreement between the programmed target phase α and observed phase difference δ is obtained.

We have repeated the same experiment for a 2×3 transmission matrix of the form:

$$\mathbf{T}_{2\times3} = \begin{bmatrix} 1 & e^{\mathrm{i}\alpha} \\ 1 & e^{\mathrm{i}\beta} \\ 1 & 1 \end{bmatrix}, \tag{B.6}$$

with controllable phase differences α and β. We take in our experiment $\beta = \alpha/4$. The results are shown in Fig C.2(b). The blue dashed lines are the expected phase differences between the output modes as a function of the programmed phase α. Again an excellent agreement between the programmed phases and observed phase differences δ are obtained.

Many parameters have to be explored to identify the restrictions of our algorithm. It would be fascinating to explore the influence of the scattering properties of the material, *e.g.*, the sample geometry, the sample thickness, and scattering mean free path. The performance of our algorithm is expected to be affected by the efficiency of the wavefront shaping process, determining the intensity enhancement and the amount of light that gets focused in a target speckle spot.

At any rate, our proof-of-principle experiments demonstrate an excellent agreement with theory. We anticipate that our algorithm can be implemented to create more advanced linear optical circuits.

APPENDIX C

How good is the wavefront-shaped beam splitter?

In adaptive quantum optics random multiple-scattering media are used as a platform for experiments. It is therefore essential to understand how efficiently one can shape a speckle pattern with a programmed correlation to achieve a desired interference. In this appendix we estimate an upper limit for the efficiency of a wavefront-shaped balanced beam splitter. We extract two parameters that describe the performance of the wavefront-shaped balanced beam splitter: (*i*) the phase difference δ one would observe in interference experiments as described in Sec. 7.5 and Sec. B.2. (*ii*) The energy coupling efficiency C_{eff} that defines the amount of energy of the light field that would undergo the transmission matrix of the ideal lossless beam splitter. This quantity is illustrated in Fig. C.1 by two additional beam splitters with energy transmission $T = |t|^2 = C_{\text{eff}}$.

C.1. Explanation of the simulation

Definitions and approximations

In our simulations we describe random isotropic multiple-scattering media by randomly generated scattering matrices $\mathbf{S}$ of different size. We call each element of the input vector of $\mathbf{S}$ an input channel, and each element of the output vector an output channel. The number of input channels and the number of output channels is equal to the dimension of $\mathbf{S}$: $\text{Dim}(\mathbf{S})$. A number of input channels together form a separate input mode. The phase of each input channel within a mode is controlled; one input mode describes a wavefront-shaped incident beam. We define the input control ratio R_s as the number of controlled input channels divided by the total number of input channels. We define the mode control ratio r_s as the number of input channels in one input mode divided by the total number of channels. In our simulations the number of input channels is the same for every mode, and therefore $R_s = nr_s$ with $n = 2$ input modes. Two output channels form the two target output modes of the wavefront-shaped beam splitter. The simulations describe a continuous-wave experiment where every input channel can contribute to the output channels by optical interference. The results are valid for situations where the coherence length of the light source is much longer than the average path length that light propagates through the random scattering medium.

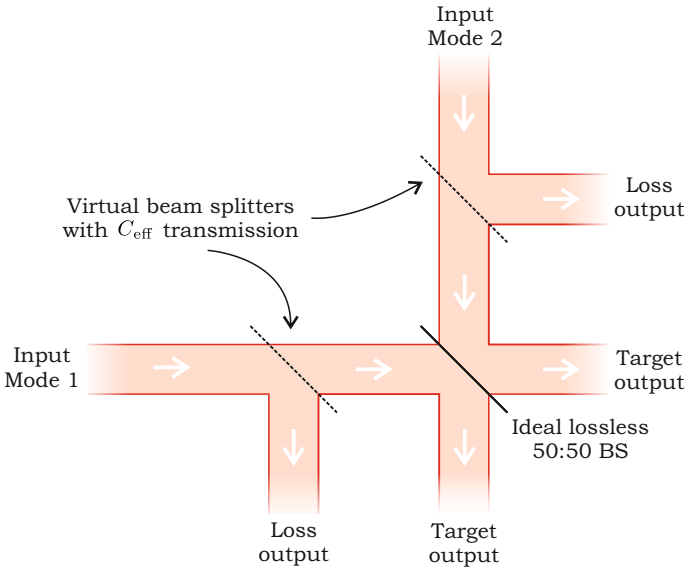

Figure C.1. Explanation of the energy coupling efficiency C_{eff}. The wavefront-shaped beam splitter will be a lossy device. To quantify the fraction of the incident energy that undergoes the desired beam splitting transmission matrix, we approximate the device by an ideal lossless balanced beam splitter and two additional 'virtual' beam splitters that give an energy loss. These 'virtual' beam splitters have an energy transmission of C_{eff}.

We want to program a target transmission matrix described by:

$$\mathbf{T}_{\text{target}} = \frac{1}{\sqrt{2}} \begin{bmatrix} 1 & -1 \\ 1 & 1 \end{bmatrix}. \tag{C.1}$$

Simulation for given Dim(S) and R_s

Here we describe the simulation steps required to program $\mathbf{T}_{\text{target}}$:

1. Generate a random $\mathbf{S}$ with a given $\text{Dim}(\mathbf{S}) = D$.

2. Select two random output channels i'_1 and i'_2 of $\mathbf{S}$, these will form the two target output speckles. From now on one only has to consider rows i'_1 and i'_2 of $\mathbf{S}$. The output channels i'_1 and i'_2 are chosen randomly for ensemble averaging.

3. We define the number of input channels $p = r_s D$. Input mode 1 is formed by input channels $j = 1 \cdots p$. Input mode 2 is formed by input channels $j = p + 1 \cdots 2p$. From now on one only has to consider columns $1 \cdots 2p$ of $\mathbf{S}$. This relates the field amplitudes in the output channels to the field amplitudes of the input channels as:

$$\begin{bmatrix} E'_1 \\ E'_2 \end{bmatrix} = \mathbf{T}' \begin{bmatrix} E_1 \\ E_2 \\ \vdots \\ E_{2p} \end{bmatrix}, \tag{C.2}$$

   with transfer matrix $\mathbf{T}'$ given by:

$$\mathbf{T}' = \begin{bmatrix} S_{i'_1,1} & S_{i'_1,2} & \cdots & S_{i'_1,2p} \\ S_{i'_2,1} & S_{i'_2,2} & \cdots & S_{i'_2,2p} \end{bmatrix}. \tag{C.3}$$

4. The algorithm of Sec. B.2. is applied to obtain a beam splitter. We first start with output mode 1. Therefore we only consider row 1 of $\mathbf{T}'$. Suppose the medium is illuminated with an incident plane wave. A maximum field amplitude for E'_1 is obtained if all elements $S_{i'_1,1} \cdots S_{i'_1,2p}$ have the same phase. Therefore we set the controlled phase ϕ_j for each input channel equal to $-\arg\left(S_{i'_1,j}\right)$, which is a direct application of phase conjugation and gives the highest possible enhancement for a single output channel.

5. We set $E_1 \cdots E_p = 1$ and $E_{p+1} \cdots E_{2p} = 0$. The corresponding field $A_{1,1} = \sum E_j \phi_j$ is calculated, which is a real number because of phase conjugation in the previous step. The same is done for $E_1 \cdots E_p = 0$ and $E_{p+1} \cdots E_{2p} = 1$ to obtain $A_{1,2}$.

6. One aims for $A_{1,1} = A_{1,2}$ to get a balanced beam splitter. Suppose one of the two output amplitudes is significantly smaller, *e.g.*, $A_{1,1} < A_{1,2}$. We can compensate that by reducing $A_{1,2}$ by adjusting the phase pattern of ϕ_j between $j = p + 1 \cdots 2p$ by choosing a random value for ϕ_j

for a random input channel. This is repeated for random input channels until $||A_{1,2}| - A_{1,1}|\,/A_{1,1} < 0.02$. Here $A_{1,2}$ becomes a complex number, however, $\mathrm{Re}(A_{1,2}) \gg \mathrm{Im}(A_{1,2})$ since random values for ϕ_j are chosen and $D \gg 10$.

7. A phase offset of $\arg(\mathbf{T}_{\mathrm{target},1,1})$ is added to $\phi_1 \cdots \phi_p$ and a phase offset of $\arg(\mathbf{T}_{\mathrm{target},1,2})$ is added to $\phi_{p+1} \cdots \phi_{2p}$. The phase mask $\boldsymbol{\theta}_1$ is given by all $\phi_1 \cdots \phi_{2p}$.

8. Repeat steps 4-7 for output mode 2 to obtain $\boldsymbol{\theta}_2$.

9. The total phase mask is given by:

$$\boldsymbol{\Theta} = \arg\left(e^{\mathrm{i}\boldsymbol{\theta}_1} + e^{\mathrm{i}\boldsymbol{\theta}_2}\right), \tag{C.4}$$

And is used to form a diagonal matrix $\boldsymbol{\Theta}$ of the form:

$$\begin{bmatrix} \Theta_1 & 0 & \dots & 0 \\ 0 & \Theta_2 & & 0 \\ \vdots & & \ddots & \vdots \\ 0 & 0 & \dots & \Theta_{2p} \end{bmatrix}. \tag{C.5}$$

10. One now has related all the output channels to the input channels as:

$$\begin{bmatrix} E_1' \\ E_2' \end{bmatrix} = \mathbf{T}' e^{\mathrm{i}\Theta} \begin{bmatrix} E_1 \\ E_2 \\ \vdots \\ E_{2p} \end{bmatrix}. \tag{C.6}$$

This is an equation of the form

$$\begin{bmatrix} E_1' \\ E_2' \end{bmatrix} = \mathbf{T} \begin{bmatrix} \mathbf{E}_1 \\ \mathbf{E}_2 \end{bmatrix}, \tag{C.7}$$

where $\mathbf{E}_j$ are the input modes. The corresponding elements of the 2×2 transmission matrix $\mathbf{T}$ are calculated with Eq. (B.6) by setting all the amplitudes of the input channels $E_j = 1$ for the first input mode ($j = 1 \cdots p$) and $E_j = 0$ for the second input mode ($j = p + 1 \cdots 2p$), and vice versa.

11. The phase difference δ that would be observed in an interference experiment is given by:

$$\delta = |(\arg(T_{1,1}) - \arg(T_{1,2})) - (\arg(T_{2,1}) - \arg(T_{2,2}))|, \tag{C.8}$$

that can be reduced to the range between $0 \cdots 2\pi$.

12. The energy coupling efficiency C_{eff} is given by the average intensity transmission to the target output channels (B.7) divided by the same number for Eq. (B.1). In Fig. C.1 there is a 'virtual' loss beam splitter for every input mode. One therefore gets a value for C_{eff} for every input channel. We restrict ourselves to the average C_{eff} of both input channels.

13. Repeat steps 1-12 for ensemble averaging.

C.2. Computational results

We have performed simulations for different Dim($\mathbf{S}$) and input control ratios R_s. Each realization was repeated 99 times. The results are presented in Fig. C.2.

Figure C.2(a) shows the phase difference δ that one would observe in an interference experiment. The data points correspond with Dim($\mathbf{S}$) = 2000. A mean phase difference $\langle\delta\rangle = \pi$ is observed that is independent of R_s. The phase difference is in excellent agreement with the programmed target phase difference (dashed blue curve). This result reproduces for Dim($\mathbf{S}$) = $100, 200, 500, 1000$ and is therefore expected to have converged to the limit that the presented $\langle\delta\rangle$ are independent of Dim($\mathbf{S}$). The errors are formed by 2 times the standard deviation $\sigma(\delta)$ of the simulations. The error in δ decreases with increasing R_s. Figure C.2(c) demonstrates that $\sigma(\delta)$ decreases as a function of R_s for all Dim($\mathbf{S}$). The higher Dim($\mathbf{S}$) the smaller $\sigma(\delta)$ becomes. Both observations can be attributed to a better control of interference since more input channels contribute to the target output channels.

Figure C.2(b) shows the energy coupling efficiency C_{eff} as a function of R_s. The data points correspond with Dim($\mathbf{S}$) = 2000. The mean coupling efficiency is well described by the line $\langle C_{\text{eff}}\rangle = (1/3)R_s$ (dashed blue curve), for which we do not have an explanation for. Again, this result reproduces for Dim($\mathbf{S}$) = $100, 200, 500, 1000$ and is therefore expected to have converged to the limit that the presented $\langle C_{\text{eff}}\rangle$ are independent of Dim($\mathbf{S}$). The error in C_{eff} increases with increasing R_s. Figure C.2(d) shows that the standard deviation $\sigma(C_{\text{eff}})$ increases as a function of R_s for all Dim($\mathbf{S}$). The higher Dim($\mathbf{S}$) the smaller $\sigma(C_{\text{eff}})$ becomes, which can be attributed to a better control of interference since more channels contribute. For $R_s = 1$ one can expect a wavefront shaped balanced beam splitter with an average splitting ratio of $(1/3)\times$(50:50)=17:17. In other words, if one controls in an experiment all incident modes (over 4π for all polarizations), one would obtain on average a 17:17 beam splitter and the remaining 66% of the light energy is distributed over other output channels.

The mean phase difference $\langle\delta\rangle = \pi$ is excellent for optical experiments. In state-of-the-art wavefront shaping experiments reported in literature it is expected that $R_s \leq 0.1$. The corresponding $\sigma(\delta(R_s = 0.1))$ requires that several realizations might have to be made before $\delta = \pi$ is observed with high precision. The corresponding energy coupling efficiency $C_{\text{eff}}(R_s = 0.1) \simeq 0.03$ is sufficiently high for both classical and quantum optical interference experiments. The expected reference coincidence rate[1] of a Hong-Ou-Mandel (HOM) experiment would decrease by a factor $C_{\text{eff}}^2 \simeq 10^{-3}$ compared to the ideal beam splitter, which would be feasible with current single-photon sources. Our single-photon source gives a reference coincidence rate in the order of $10^3 - 10^4$ s^{-1} with a dip visibility of 36% for a normal beam splitter. The maximum expected HOM reference coincidence

[1] The coincidence rate when the photons do not interfere.

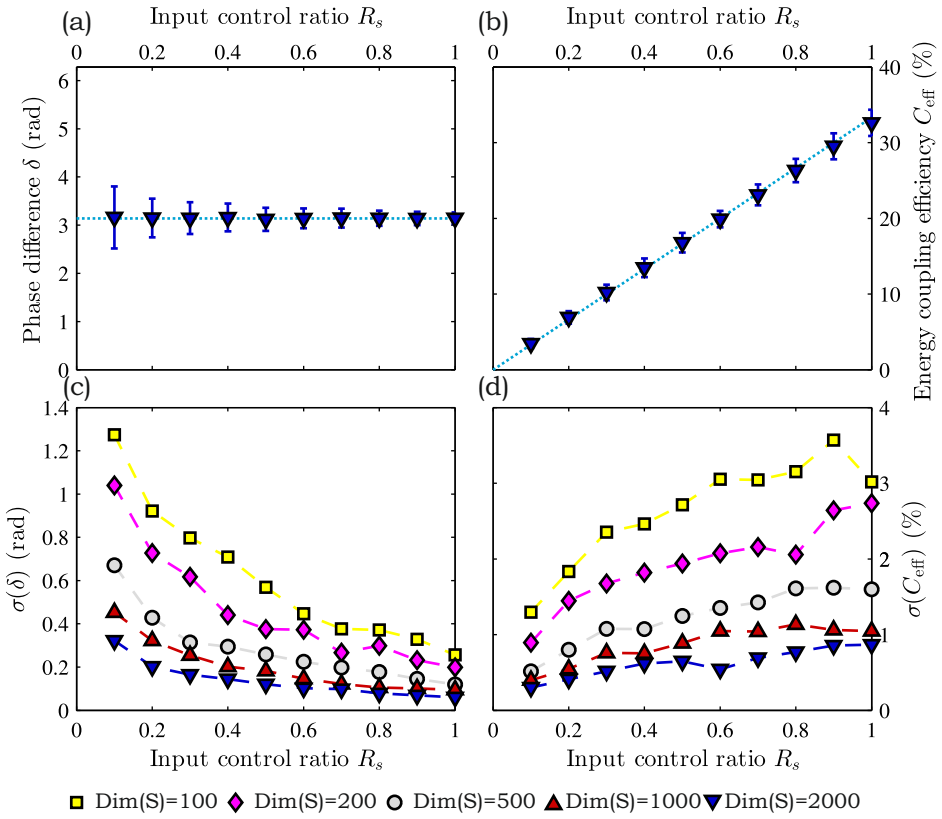

Figure C.2. Calculated efficiency of the wavefront-shaped balanced beam splitter as a function of the relative number of channels that is controlled. (*a*) Obtained phase difference δ one would observe in an interference experiment. The blue dashed curve is the programmed target phase difference of π. (*c*) Standard deviation over the obtained phase difference for different sizes of the scattering matrix Dim(**S**). (*b*) Observed energy coupling efficiency C_{eff}. The blue dashed curve is given by $(1/3)R_s$, which seems to describe the calculated data points very well. (*d*) Standard deviation over the obtained coupling efficiency for different Dim(**S**).

rate would therefore be in the order of $0.1 - 1\ \mathrm{s}^{-1}$ for a wavefront-shaped beam splitter in a random multiple-scattering medium. These numbers demonstrate that a HOM experiment is indeed possible with adaptive quantum optics.

Bibliography

[1] V.P. Bykov. Spontaneous emission form a medium with a band spectrum. *Soviet Journal of Quantum Electronics*, 4:861, 1975. — p.1.

[2] M.P. van Albada and A. Lagendijk. Observation of weak localization of light in a random medium. *Physical Review Letters*, 55:2692, 1985. — p.1.

[3] P.-E. Wolf and G. Maret. Weak localization and coherent backscattering of photons in disordered media. *Physical Review Letters*, 55:2696, 1985. — p.1.

[4] E. Yablonovitch. Inhibited spontaneous emission in solid-state physics and electronics. *Physical Review Letters*, 58:2059, 1987. — p.1, 15, 25.

[5] S. John. Strong localization of photons in certain disordered dielectric superlattices. *Physical Review Letters*, 58:2486, 1987. — p.1, 25, 51.

[6] J.D. Joannopoulos, S.G. Johnson, J.N. Winn, and R.D. Meade. *Photonic crystals molding the flow of light*. Princeton University Press, 2nd edition, 2008. — p.1, 2, 3, 5, 6, 8, 15, 19, 23, 25, 26, 41, 43, 51.

[7] C.M. Soukoulis. *Photonic crystals and light localization in the 21st century*. Kluwer, 2001. — p.1.

[8] L. Novotny and B. Hecht. *Principles of nano-optics*. Cambridge University Press, Cambridge, 2006. — p.1, 41, 52.

[9] A.F. Koenderink. *Emission and transport of light in photonic crystals*. PhD thesis, University of Amsterdam, 2003. — p.1, 5, 32.

[10] J.D. Joannopoulos, P.R. Villeneuve, and S. Fan. Photonic crystals: putting a new twist on light. *Nature*, 386:143, 1997. — p.1, 25.

[11] K.J. Vahala. Optical microcavities. *Nature*, 424:839, 2003. — p.1.

[12] C. López. Materials aspects of photonic crystals. *Advanced Materials*, 15:1679, 2003. — p.1.

[13] A. Lagendijk, B. van Tiggelen, and D.S. Wiersma. Fifty years of Anderson localization. *Physics Today*, 62:24, 2009. — p.1, 7, 51.

[14] D.S. Wiersma. Disordered photonics. *Nature Photonics*, 7:188, 2013. — p.1.

[15] J. Topolancik, B. Ilic, and F. Vollmer. Experimental observation of strong photon localization in disordered photonic-crystal waveguides. *Physical Review Letters*, 99:253901, 2007. — p.1, 8, 50, 52, 53, 55, 56.

[16] P. Lodahl, A.P. Mosk, and A. Lagendijk. Spatial quantum correlations in multiple scattered light. *Physical Review Letters*, 95:173901, 2005. — p.1, 10, 63, 82.

[17] S. Smolka, A. Huck, U.L. Andersen, A. Lagendijk, and P. Lodahl. Observation of spatial quantum correlations induced by multiple scattering of nonclassical light. *Physical Review Letters*, 102:193901, 2009. — p.1, 10, 63, 82.

[18] L. Sapienza, H. Thyrrestrup, S. Stobbe, P.D. García, S. Smolka, and P. Lodahl. Cavity quantum electrodynamics with Anderson-localized modes. *Science*, 327:1352, 2010. — p.1, 8, 10, 50, 52, 55, 57, 63.

[19] A. Peruzzo, M. Lobino, J.C.F. Matthews, N. Matsuda, A. Politi, K. Poulios, X.-Q. Zhou,

Y. Lahini, N. Ismail, K. Wörhoff, Y. Bromberg, Y. Silberberg, M.G. Thompson, and J.L. O'Brien. Quantum walks of correlated photons. *Science*, 329:1500, 2010. — p.1, 10, 63, 82.

[20] J.R. Ott, N.A. Mortensen, and P. Lodahl. Quantum interference and entanglement induced by multiple scattering of light. *Physical Review Letters*, 105:090501, 2010. — p.1, 63, 64, 82.

[21] Y. Lahini, Y. Bromberg, D.N. Christodoulides, and Y. Silberberg. Quantum correlations in Anderson localization of indistinguishable particles. *Physical Review Letters*, 105:163905, 2010. — p.1, 10, 63, 82.

[22] Y. Lahini, Y. Bromberg, Y. Shechtman, A. Szameit, D.N. Christodoulides, R. Morandotti, and Y. Silberberg. Hanbury Brown and Twiss correlations of Anderson localized waves. *Physical Review A*, 84:041806(R), 2011. — p.1.

[23] A. Crespi, R. Osellame, V. Ramoni, Giovannetti, R. Fazio, L. Sansoni, F. De Nicola, F. Sciarrino, and P. Mataloni. Anderson localization of entangled photons in an integrated quantum walk. *Nature Photonics*, 7:322, 2013. — p.1.

[24] J.L. O'Brien, A. Furusawa, and J. Vučković. Photonic quantum technologies. *Nature Photonics*, 3:687, 2009. — p.1, 9, 71.

[25] S. Tanzilli, A. Martin, F. Kaiser, M.P. de Micheli, O. Alibart, and D.B. Ostrowksy. On the genesis and evolution of integrated quantum optics. *Laser and Photonics Reviews*, 6:115, 2012. — p.1, 9.

[26] I.M. Vellekoop and A.P. Mosk. Focusing coherent light through opaque strongly scattering media. *Optics Letters*, 32:2309, 2007. — p.1, 9, 63, 65, 69, 71, 91.

[27] A.P. Mosk, A. Lagendijk, G. Lerosey, and M. Fink. Controlling waves in space and time for imaging and focusing in complex media. *Nature Photonics*, 6:283, 2012. — p.1, 9, 63, 71, 91.

[28] N.W. Ashcroft and N.D. Mermin. *Solid state physics*. Thomson Learning, 1976. — p.2, 4, 6, 15, 16, 25, 51.

[29] E.N. Economou. *The physics of solids*. Springer, 1st edition, 2010. — p.2, 15, 16.

[30] A. Yariv and P. Yeh. *Optical waves in crystals*. John Wiley & Sons, 1984. — p.3, 5.

[31] R.J.P. Engelen. *Ultrafast investigation of slow light in photonic-crystal structures*. PhD thesis, University of Twente, 2008. — p.3, 44.

[32] J.C. Garrison and R.Y. Chiao. *Quantum optics*. Oxford University Press, first edition, 2008. — p.3, 9.

[33] W.L. Bragg. The diffraction of short electromagnetic waves by a crystal. *Proceedings of the Cambridge Philosophical Society*, 17:43, 1913. — p.4.

[34] W.L. Vos, R. Sprik, A. van Blaaderen, A. Imhof, A. Lagendijk, and G.H. Wegdam. Strong effects of photonic band structures on the diffraction of colloidal crystals. *Physical Review B*, 53:16231, 1996. — p.5, 17, 25.

[35] W.L. Vos, H.M. van Driel, M. Megens, A.F. Koenderink, and A. Imhof. Experimental probes of the optical properties of photonic crystals. In C.M. Soukoulis, editor, *Proceedings of the NATO ASI "Photonic Crystals and Light Localization in the 21st century"*, page 181, 2001. — p.5.

[36] K. Sakoda. Symmetry, degeneracy, and uncoupled modes in two-dimensional photonic lattices. *Physical Review B*, 52:7982, 1995. — p.6, 19, 26.

[37] W. Friedrich, P. Knipping, and M. Laue. *Sitzungsberichte der Kniglich Bayerischen Akademie der Wissenschaften*, 303, 1912. — p.6.

[38] H.M. van Driel and W.L. Vos. Multiple Bragg wave coupling in photonic band-gap crystals. *Physical Review B*, 62:9872, 2000. — p.6, 16, 20.

[39] W.L. Vos and H.M. van Driel. Higher order Bragg diffraction by strongly photonic fcc crystals: onset of a photonic bandgap. *Physical Review A*, 272:101, 2000. — p.6, 16, 23, 26.

[40] H.S. Sözüer and J.W. Haus. Photonic bands: simple-cubic lattice. *Journal of the Optical Society of America B*, 10:296, 1993. — p.6.

[41] K.M. Ho, C.T. Chan, and C.M. Soukoulis. Existence of a photonic gap in periodic dielectric structures. *Physical Review Letters*, 65:3152, 1990. — p.6, 26.

[42] C.T. Chan, K.M. Ho, and C.M. Soukoulis. Photonic band gaps in exexperimental realizable periodic dielectric structures. *Europhysics Letters*, 16:563, 1991. — p.6.

[43] E. Yablonovitch, T.J. Gmitter, and K.M. Leung. Photonic band structure: the face-centered-cubic case employing nonspherical atoms. *Physical Review Letters*, 67:2295, 1991. — p.6.

[44] M. Ho, C.T. Chan, C.M. Soukoulis, R. Biswas, and M. Sigalas. Photonic band gaps in three dimensions: new layer-by-layer periodic structures. *Solid State Communications*, 89:413, 1994. — p.6, 26, 27.

[45] K. Busch and S. John. Photonic band gap formation in certain self-organizing systems. *Physical Review E*, 58:3896, 1998. — p.6.

[46] S.R. Huisman, R.V. Nair, L.A.W. Woldering, M.D. Leistikow, A.P. Mosk, and W.L. Vos. Signature of a three-dimensional photonic band gap observed on silicon inverse woodpile photonic crystals. *Physical Review B*, 83:205313, 2011. — p.7, 16.

[47] M.D. Leistikow, A.P. Mosk, E. Yeganegi, S.R. Huisman, A. Lagendijk, and W.L. Vos. Inhibited spontaneous emission of quantum dots observed in a 3D photonic band gap. *Physical Review Letters*, 107:193903, 2011. — p.7, 37, 59, 85.

[48] P.W. Anderson. Absence of diffusion in certain random lattices. *Physical Review*, 109:1492, 1958. — p.7, 51.

[49] P. Sheng. *Introduction to wave scattering, localization, and mesoscopic phenomena*. Academic Press, 1st edition, 1995. — p.7, 51, 63.

[50] M. Notomi, K. Yamada, A. Shinya, J. Takahashi, C. Takahashi, and I. Yokohama. Extremely large group-velocity dispersion of line-defect waveguides in photonic crystal slabs. *Physical Review Letters*, 87:253902, 2001. — p.8.

[51] H. Gersen, T.J. Karle, R.J.P. Engelen, W. Bogaerts, J.P. Korterik, N.F. van Hulst, T.F. Krauss, and L. Kuipers. Real-space observation of ultraslow light in photonic crystal waveguides. *Physical Review Letters*, 94:073903, 2005. — p.8, 41, 52, 54, 57.

[52] T.F. Krauss. Slow light in photonic-crystal waveguides. *Journal of Physics D: Applied Physics*, 40:2666, 2007. — p.8, 41, 51.

[53] T. Baba. Slow light in photonic crystals. *Nature Photonics*, 2:465, 2008. — p.8.

[54] J.-K. Yang, H. Noh, M.J. Rooks, G.S. Solomon, F. Vollmer, and H. Cao. Lasing in localized modes of a slow light photonic crystal waveguide. *Applied Physics Letters*, 98:241107, 2011. — p.8, 50.

[55] M.L.M. Balistreri, H. Gersen, J.P. Korterik, L. Kuipers, and N.F. van Hulst. Tracking femtosecond laser pulses in space and time. *Science*, 294:1080, 2001. — p.8, 41.

[56] R.J.P. Engelen, T.J. Karle, H. Gersen, J.P. Korterik, T.F. Krauss, L. Kuipers, and N.F. van Hulst. Local probing of Bloch mode dispersion in a photonic crystal waveguide. *Optics Express*, 13:4457, 2005. — p.8, 41, 43.

[57] N. Louvion, A. Rahmani, C. Seassal, S. Callard, D. Gérard, and F. de Fornel. Near-field observation of subwavelength confinement of photoluminescence by a photonic crystal microcavity. *Optics Letters*, 31:2160, 2006. — p.8, 41, 52.

[58] S. Mujumdar, A.F. Koenderink, T. Sünner, B.C. Buchler, M. Kamp, A. Forchel, and V. Sandoghdar. Near-field imaging and frequency tuning of a high-Q photonic crystal membrane microcavity. *Optics Express*, 15:17214, 2007. — p.8, 41, 48, 52, 55.

[59] S. Ha, M. Spasenović, A.A. Sukhorukov, T.P. White, C.M. de Sterke, L. Kuipers, T.F. Krauss, and Y.S. Kivshar. Slow-light and evanescent modes at interfaces in photonic crystal waveguides: optimal extraction from experimental near-field measurements. *Journal of the optical society of America B*, 28:955, 2011. — p.8, 42, 44, 52.

[60] I. Freund. Looking through walls and around corners. *Physica A: Statistical Mechanics and its Applications*, 168:49, 1990. — p.9, 63, 71, 91.

[61] I.M. Vellekoop. *Controlling the propagation of light in disordered scattering media*. PhD thesis, University of Twente, 2008. — p.9, 95.

[62] E.G. van Putten, D. Akbulut, J. Bertolotti, W.L. Vos, A. Lagendijk, and A.P. Mosk. Scattering lens resolves sub-100 nm structures with visible light. *Physical Review Letters*, 106:193905, 2011. — p.9, 71, 91.

[63] J. Aulbach, B. Gjonaj, P.M. Johnson, A.P. Mosk, and A. Lagendijk. Control of light transmission through opaque scattering media in space and time. *Physical Review Letters*, 106:103901, 2011. — p.9, 63, 69, 71, 91.

[64] O. Katz, E. Small, Y. Bromberg, and Y. Silberberg. Focusing and compression of ultrashort pulses through scattering media. *Nature Photonics*, 5:372, 2011. — p.9, 63, 71, 91.

[65] Y. Guan, O. Katz, E. Small, J. Zhou, and Y. Silberberg. Polarization control of multiply scattered light through random media by wavefront shaping. *Optics Letters*, 37:4663, 2012. — p.9, 71, 91.

[66] B. Gjonaj, J. Aulbach, P.M. Johnson, A.P. Mosk, L. Kuipers, and A. Lagendijk. Active spatial control of plasmonic fields. *Nature Photonics*, 5:360, 2011. — p.9.

[67] M.O. Scully and Zubairy. M.S. *Quantum optics*. Camebridge University Press, reprinted edition, 1997. — p.9.

[68] M.A. Nielsen and I.L. Chuang. *Quantum computation and quantum information*. Cambridge University Press, 1st edition, 2000. — p.9, 71.

[69] H.A. Bachor and T.C. Ralph. *A guide to experiments in quantum optics*. Wiley-VCH, second, revised and enlarged edition, 2004. — p.9.

[70] P.J. Shadbolt, M.R. Verde, A. Peruzzo, A. Politi, A. Laing, M. Lobino, J.C.F. Matthews, M.G. Thompson, and J.L. O'Brien. Generating, manipulating and measuring entanglement and mixture with a reconfigurable photonic circuit. *Nature Photonics*, 6:45, 2012. — p.9.

[71] S.W. Leonard, H.M. van Driel, J. Schilling, and R.B. Wehrspohn. Ultrafast band-edge tuning of a two-dimensional silicon photonic crystal via free-carrier injection. *Physical Review B*, 66:161102, 2002. — p.10.

[72] D. Bonneau, E. Engin, K. Ohira, N. Suzuki, H. Yoshida, N. Iizuka, M. Ezaki, C.M. Natarajan, M.G. Tanner, R.H. Hadfield, S.N. Dorenbos, V. Zwiller, J. O'Brien, and M.G. Thompson. Quantum interference and manipulation of entanglement in silicon wire waveguide quantum circuits. *New Journal of Physics*, 14:045003, 2012. — p.10, 63, 82.

[73] E. Yüce, G. Ctistis, J. Claudon, E. Dupuy, K.J. Boller, J.M. Gérard, and W.L. Vos. Competition between electronic Kerr and free carrier effects in an ultimate-fast optically switched semiconductor microcavity. *Journal of the Optical Society of America B*, 29:2630, 2012. — p.10.

[74] W.H. Peeters, J.J.D. Moerman, and M.P. van Exter. Observation of two-photon speckle patterns. *Physical Review Letters*, 104:173601, 2010. — p.10, 63, 82.

[75] Y. Bromberg, Y. Lahini, R. Morandotti, and Y. Silberberg. Quantum and classical correlations in waveguide lattices. *Physical Review Letters*, 102:253904, 2009. — p.10, 63, 82.

[76] A. Pe'er, B. Dayan, A.A. Friesem, and Y. Silberberg. Temporal shaping of entangled photons. *Physical Review Letters*, 94:073601, 2005. — p.10.

[77] M. Stütz, E.S. Gröblacher, T. Jennewein, and A. Zeilinger. How to create and detect n-dimensional entangled photons with an active phase hologram. *Applied Physics Letters*, 90:261114, 2007. — p.10.

[78] A. Valencia, A. Ceré, X. Shi, G. Molina-Terriza, and J.P. Torres. Shaping the waveform of entangled photons. *Physical Review Letters*, 99:243601, 2007. — p.10.

[79] S. Cialdi, D. Brivio, and M.G.A. Paris. Demonstration of a programmable source of two-photon multiqubit entangled states. *Physical Review A*, 81:042322, 2010. — p.10.

[80] V.D. Salakhutdinov, E.R. Eliel, and W. Löffler. Full-field quantum correlations of spatially entangled photons. *Physical Review Letters*, 108:173604, 2012. — p.10.

[81] S.M. Popoff, G. Lerosey, R. Carminati, M. Fink, A.C. Boccara, and S. Gigan. Measuring the transmission matrix in optics: an approach to the study and control of light propagation in disordered media. *Physical Review Letters*, 104:100601, 2010. — p.10, 69, 71, 79.

[82] R.W. James. *The optical principles of diffraction of X-rays*. G. Bell and Sons, 1st edition, 1958. — p.15.

[83] B.N. Brockhouse. Slow neutron spectroscopy and the grand atlas of the physical world. *Reviews of Modern Physics*, 67:735, 1995. — p.15.

[84] A.K. Geim and K.S. Novoselov. The rise of graphene. *Nature Materials*, 6:183, 2007. — p.15, 16.

[85] S. Yang, J.H. Page, Z. Liu, M.L. Cowan, C.T. Chan, and P. Sheng. Ultrasound tunneling through 3D phononic crystals. *Physical Review Letters*, 88:104301, 2002. — p.15, 16.

[86] S. Yang, J.H. Page, Z. Liu, M.L. Cowan, C.T. Chan, and P. Sheng. Focusing of sound in a 3d phononic crystal. *Physical Review Letters*, 93:024301, 2004. — p.15, 16.

[87] S.L. Chang. *Multiple diffraction of X-rays in crystals*. Springer, 1st edition, 1984. — p.16.

[88] S.G. Romanov, T. Maka, C.M. Sotomayor Torres, M. Müller, R. Zentel, D. Cassagne, J. Manzanares-Martinez, and C. Jouanin. Diffraction of light from thin-film polymethylmethacrylate opaline photonic crystals. *Physical Review E*, 63:056603, 2001. — p.16.

[89] A. Tikhonov, J. Bohn, and S.A. Asher. Photonic crystal multiple diffraction observed by angular-resolved reflection measurements. *Physical Review B*, 80:235125, 2009. — p.16.

[90] L.A. Woldering, R.W. Tjerkstra, H.V. Jansen, I.D. Setija, and W.L. Vos. Periodic arrays of deep nanopores made in silicon with reactive ion etching and deep UV lithography. *Nanotechnology*, 19:145304, 2008. — p.16.

[91] S.G. Johnson and J.D. Joannopoulos. Block-iterative frequency-domain methods for Maxwell's equations in a planewave basis. *Optics Express*, 8:173, 2001. — p.17, 29, 43,

46, 52.

[92] A.F. Oskooi, D. Roundy, M. Ibanescu, P. Bermel, J.D. Joannopoulos, and S.G. Johnson. MEEP: a flexible free-software package for electromagnetic simulations by the FDTD method. *Computer Physics Communications*, 181:687, 2010. — p.18.

[93] S. Rowson, A. Chelnokov, C. Cuisin, and J.-M. Lourtioz. Two-dimensional photonic bandgap reflectors for free-propagating beams in the mid-infrared. *Journal of Optics A: Pure and Applied Optics*, 1:483, 1999. — p.22.

[94] J.G. Fleming, S.Y. Lin, I. El-Kady, R. Biswas, and K.M. Ho. All-metallic three-dimensional photonic crystals with a large infrared bandgap. *Nature*, 417:52, 2002. — p.25.

[95] A.F. Koenderink, L. Bechger, H.P. Schriemer, A. Lagendijk, and W.L. Vos. Broadband fivefold reduction of vacuum fluctuations probed by dyes in photonic crystals. *Physical Review Letters*, 88:143903, 2002. — p.25, 26, 37.

[96] J.F.G. Lopez and W.L. Vos. Angle resolved reflectivity of single-domain photonic crystals, effects of disorder. *Physical Review E*, 66:036616, 2002. — p.25.

[97] P. Lodahl, A.F. van Driel, I.S. Nikolaev, A. Irman, K. Overgaag, D. Vanmaekelbergh, and W.L. Vos. Controlling the dynamics of spontaneous emission from quantum dots by photonic crystals. *Nature*, 430:654, 2004. — p.25, 26, 37.

[98] S. Ogawa, M. Imada, S. Yoshimoto, M. Okano, and S. Noda. Control of light emission by 3D photonic crystals. *Science*, 305:227, 2004. — p.25, 26, 37.

[99] S.E. Han, A. Stein, and D.J. Norris. Tailoring self-assembled metallic photonic crystals for modified thermal emission. *Physical Review Letters*, 99:053906, 2007. — p.25.

[100] S. Takahashi, K. Suzuki, M. Okana, M. Imada, T. Nakamori, Y. Ota, K. Ishizaki, and S. Noda. Direct creation of three-dimensional photonic crystals by a top-down approach. *Nature Materials*, 8:721, 2009. — p.25, 26.

[101] T. Ergin, N. Stenger, P. Brenner, J.B. Pendry, and M. Wegener. Three-dimensional invisibility cloak at optical wavelengths. *Science*, 328:337, 2010. — p.25.

[102] A. Tandaechanurat, S. Ishida, D. Guimard, M. Nomura, S. Iwamoto, and Y. Arakawa. Lasing oscillation in a three-dimensional photonic crystal nanocavity with a complete bandgap. *Nature Photonics*, 5:91, 2011. — p.25.

[103] J.J. Wierer, A. David, and M.M. Megens. III-nitride photonic-crystal light-emitting diodes with high extraction efficiency. *Nature Photonics*, 3:163, 2009. — p.25.

[104] D. Zhou and R. Biswas. Photonic crystal enhanced light-trapping in thin film solar cells. *Journal of Applied Physics*, 103:093102, 2008. — p.25.

[105] J.G. Fleming and S.-Y. Lin. Three-dimensional photonic crystal with a stop band from 1.35 to 1.95 μm. *Optics Letters*, 24:49, 1999. — p.26.

[106] A. Blanco, E. Chomski, S. Grabtchak, M. Ibisate, S. John, S.W. Leonard, C. López, F. Meseguer, H. Miguez, J.P Mondia, G.A. Ozin, O. Toader, and H.M. van Driel. Large-scale synthesis of a silicon photonic crystal with a complete three-dimensional bandgap near 1.5 micrometres. *Nature*, 405:437, 2000. — p.26.

[107] S. Noda, K. Tomoda, N. Yamamoto, and A. Chutinan. Full three-dimensional photonic bandgap crystals at near-infrared wavelengths. *Science*, 289:604, 2000. — p.26.

[108] Y.A. Vlasov, X. Bo, J.C. Sturm, and D.J. Norris. On-chip natural assembly of silicon photonic bandgap crystals. *Nature*, 414:289, 2000. — p.26.

[109] G. Subramania and S.-Y. Lin. Fabrication of three-dimensional photonic crystal with alignment based on electron beam lithography. *Applied Physics Letters*, 85:5037, 2004.

— p.26.

[110] J. Schilling, J. White, A. Scherer, G. Stupian, R. Hillebrand, and U. Gösele. Three-dimensional macroporous silicon photonic crystal with large photonic band gap. *Applied Physics Letters*, 86:011101, 2005. — p.26.

[111] W.M. Robertson, G. Arjavalingam, R.D. Meade, K.D. Brommer, A.M. Rappe, and J.D. Joannopoulos. Measurement of photonic band structure in a two-dimensional periodic dielectric array. *Phys. Rev. Lett.*, 68:2023, 1992. — p.26.

[112] E. Palacios-Lidón, A. Blanco, M. Ibisate, F. Meseguer, and C. López. Optical study of the full photonic band gap in silicon inverse opals. *Applied Physics Letters*, 81:4925, 2002. — p.26.

[113] I. Staude, G. von Freymann, S. Essig, K. Busch, and M. Wegener. Waveguides in three-dimensional photonic-bandgap materials by direct laser writing and silicon double inversion. *Optics Letters*, 36:67, 2011. — p.26.

[114] R. Hillebrand and W. Hergert. Scaling properties of a tetragonal photonic crystal design having a large complete bandgap. *Photonics and Nanostructures - Fundamentals and Applications*, 2:33 — p.26, 27, 29.

[115] S. Takahashi, M. Okano, M. Imada, and S. Noda. Three-dimensional photonic crystals based on double-angled etching and wafer-fusion techniques. *Applied Physics Letters*, 89:123106, 2006. — p.26.

[116] F.G. Santamaria, M. Xu, V. Lousse, S. Fan, P. V. Braun, and J.A. Lewis. A germanium inverse woodpile structure with a large photonic band gap. *Advanced Materials*, 19:1567, 2007. — p.26.

[117] A. Hermatschweiler, A. Ledermann, G.A. Ozin, M. Wegener, and G. von Freymann. Fabrication of silicon inverse woodpile photonic crystals. *Advanced Functional Materials*, 17:2273, 2007. — p.26.

[118] B. Jia, S. Wu, J. Li, and M. Gu. Near-infrared high refractive-index three-dimensional inverse woodpile photonic crystals generated by a sol-gel process. *Journal of Applied Physics*, 102:096102, 2007. — p.26.

[119] D.J. Shir, E.C. Nelson, D. Chanda, A. Brzezinski, P.V. Braun, J.A. Rogers, and P. Wiltzius. Dual exposure, two-photon, conformal phase mask lithography for three dimensional silicon inverse woodpile photonic crystals. *Journal of Vacuum Science & Technology, B*, 28:783, 2010. — p.26.

[120] L. Tang and T. Yoshie. Light localization in woodpile photonic crystal built via two-directional etching method. *IEEE Journal of Quantum Electronics*, 47:1028, 2011. — p.26.

[121] L.A. Woldering, A.P. Mosk, R.W. Tjerkstra, and W.L. Vos. The influence of fabrication deviations on the photonic band gap of three-dimensional inverse woodpile nanostructures. *Journal of Applied Physics*, 105:093108, 2009. — p.27, 29.

[122] J.M. van den Broek, L.A. Woldering, R.W. Tjerkstra, F.B. Segerink, I.D. Setija, and W.L. Vos. Inverse-woodpile photonic band gap crystals with a cubic diamond-like structure made from single-crystalline silicon. *Advanced Functional Materials*, 22:25, 2010. — p.27, 33.

[123] R.W. Tjerkstra, L.A. Woldering, J.M. van den Broek, F. Roozeboom, I.D. Setija, and W.L. Vos. A method to pattern masks in two inclined planes for three-dimensional nano- and microfabrication. *Journal of Vacuum Science & Technology, B*, 29:061604, 2011. — p.27.

[124] G. Ctistis, A. Hartsuiker, E. van der Pol, J. Clauden, W.L Vos, and J.M. Gérard. Optical characterization and selective addressing of the resonant modes of a micropillar cavity with a white light beam. *Physical Review B*, 82:195330, 2010. — p.30.

[125] S. Datta, C.T. Chan, K.M. Ho, and C.M. Soukoulis. Effective dielectric constant of periodic composite structures. *Physical Review B*, 48:14936, 1993. — p.33.

[126] M. Megens, C.M. van Kats, P. Bösecke, and W.L. Vos. In-situ characterization of colloidal spheres by synchrotron small-angle X-ray scattering. *Langmuir*, 13:6120, 1997. — p.36.

[127] M.S. Thijssen, R. Sprik, J.E.G.J. Wijnhoven, M. Megens, T. Narayanan, A. Lagendijk, and W.L. Vos. Inhibited light propagation and broad band reflection in photonic air-sphere crystals. *Physical Review Letters*, 83:2730, 1999. — p.36.

[128] M. Notomi. Theory of light propagation in strongly modulated photonic crystals: Refractionlike behavior in the vicinity of the photonic band gap. *Physical Review B*, 62:10696, 2000. — p.36.

[129] K.S. Yee. Numerical solution of initial boundary value problems involving Maxwell's equations in isotropic media. *IEEE Transactions on Antennas and Propagation*, 14:302, 1966. — p.36.

[130] J.S. Kole. *New methods for the numerical solution of Maxwell's equations*. PhD thesis, University of Groningen, 2003. — p.37.

[131] L. Li. Formulation and comparison of two recursive matrix algorithms for modeling layered diffraction gratings. *Journal of the Optical Society of America A*, 13:1024, 1996. — p.37.

[132] L. Li. New formulation of the Fourier modal method for crossed surface-relief gratings. *Journal of the Optical Society of America A*, 14:2758, 1997. — p.37.

[133] D. Sármány, F. Izsák, and J.J.W. van der Vegt. Optimal penalty parameters for symmetric discontinuous Galerkin discretisations of the time-harmonic Maxwell equations. *Journal of Scientific Computing*, 44:219, 2010. — p.37.

[134] M.D. Leistikow, J. Johansen, A.J. Kettelarij, P. Lodahl, and W.L. Vos. Size dependent oscillator strength and quantum efficiency of CdSe quantum dots determined by controlling the local density of states. *Physical Review B*, 79:045301, 2009. — p.37.

[135] L. Lalouat, B. Cluzel, F. de Fornel, P. Velha, P. Lalanne, D. Peyrade, E. Picard, T. Charvolin, and E. Hadji. Subwavelength imaging of light confinement in high-Q/small-V photonic crystal nanocavity. *Applied Physics Letters*, 92:111111, 2008. — p.41.

[136] L. Lalouat, B. Cluzel, C. Dumas, L. Salomon, and F. de Fornel. Imaging photoexcited optical modes in photonic-crystal cavities with a near-field probe. *Physical Review B*, 83:115326, 2011. — p.41.

[137] T. Lund-Hansen, S. Stobbe, B. Julsgaard, H. Thyrrestrup, T. Sünner, M. Kamp, A. Forchel, and P. Lodahl. Experimental realization of highly efficient broadband coupling of single quantum dots to a photonic-crystal waveguide. *Physical Review Letters*, 101:113903, 2008. — p.41, 51, 59.

[138] V.S. Volkov, S.I. Bozhevolnyi, P.I. Borel, L.H. Frandsen, and M. Kristensen. Near-field characterization of low-loss photonic crystal waveguides. *Physical Review B*, 72:035118, 2005. — p.41.

[139] M. Burresi, R.J.P. Engelen, A. Opheij, D. van Oosten, D. Mori, T. Baba, and L. Kuipers. Observation of polarization singularities at the nanoscale. *Physical Review Letters*, 102:033902, 2009. — p.41, 48.

[140] S. Ha, A.A. Sukhorukov, K.B. Dossou, L.C. Botten, C.M. de Sterke, and Y.S. Kivshar.

Bloch-mode extraction from near-field data in periodic waveguides. *Optics Letters*, 34:3776, 2009. — p.41, 44, 54, 89.

[141] S. Ha, A.A. Sukhorukov, A.V. Lavrinenko, I.V. Shadrivov, D.A. Powell, and Y.S. Kivshar. Observation of tunneling of slow and fast electromagnetic modes in coupled periodic waveguides. *Applied Physics Letters*, 98:061909, 2011. — p.41.

[142] M. Spasenović, T.P. White, S. Ha, A.A. Sukhorukov, T. Kampfrath, Y.S. Kivshar, C.M. de Sterke, T.F. Krauss, and L. Kuipers. Experimental observation of evanescent modes at the interface to slow-light photonic crystal waveguides. *Optics Letters*, 36:1170, 2011. — p.42.

[143] M.L.M. Balistreri, J.P. Korterik, L. Kuipers, and N.F. van Hulst. Local observations of phase singularities in optical fields in waveguide structures. *Physical Review Letters*, 85:294, 2000. — p.46, 52.

[144] W.C.L. Hopman, K.O. van der Werf, A.J.F. Hollink, W. Bogaerts, V. Subramaniam, and R.M. de Ridder. Nano-mechanical tuning and imaging of a photonic crystal micro-cavity resonance. *Optics Express*, 14:8745, 2006. — p.48, 55.

[145] L. Lalouat, B. Cluzel, P. Velha, E. Picard, D. Peyrade, J.P. Hugonin, P. Lalanne, E. Hadji, and F. de Fornel. Near-field interactions between a subwavelength tip and a small-volume photonic-crystal nanocavity. *Physical Review B*, 76:041102, 2007. — p.48, 55.

[146] P.D. García, S. Smolka, S. Stobbe, and P. Lodahl. Density of states controls Anderson localization in disordered photonic-crystal waveguides. *Physical Review B*, 82:165103, 2010. — p.50, 52, 53, 55.

[147] B.L. Altshuler, V.E. Kravtsov, and I.V. Lerner. *Mesoscopic phenomena in solids*. North-Holland, 1991. — p.51.

[148] E. Akkermans and G. Montambaux. *Mesoscopic physics of electrons and photons*. Cambridge University Press, Cambridge, U.K., 1st edition, 2007. — p.51, 63.

[149] M. Stoytchev and A.Z. Genack. Microwave transmission through a periodic three-dimensional metal-wire network containing random scatterers. *Physical Review B*, 55:R8617, 1997. — p.51.

[150] A.A. Chabanov, M. Stoytchev, and A.Z. Genack. Statistical signatures of photon localization. *Nature*, 404:850, 2000. — p.51.

[151] L. O'Faolain, D.M. Beggs, T.P. White, T. Kampfrath, L. Kuipers, and T.F. Krauss. Compact optical switches and modulators based on dispersion engineered photonic crystals. *IEEE Photonics Journal*, 2:404, 2010. — p.51.

[152] V. Savona. Electromagnetic modes of a disordered photonic crystal. *Physical Review B*, 83:085301, 2011. — p.52, 54, 55, 57, 59.

[153] I.M. Lifshitz. The energy spectrum of disordered systems. *Advances in Physics*, 13:483, 1964. — p.52, 59.

[154] R.J. Elliott, J.A. Krumhansl, and P.L. Leath. The theory and properties of randomly disordered crystals and related physical systems. *Reviews of Modern Physics*, 46:465, 1974. — p.52, 59.

[155] P. Van Mieghem. Theory of band tails in heavily doped semiconductors. *Reviews of Modern Physics*, 64:755, 1992. — p.52, 59.

[156] A.V. Balatsky, I. Vekhter, and J.-X. Zhu. Impurity-induced states in conventional and unconventional superconductors. *Reviews of Modern Physics*, 78:373, 2006. — p.52, 59.

[157] M. Aizenman and S. Warzel. Extended states in a Lifshitz tail regime for random

Schrödinger operators on trees. *Physical Review Letters*, 106:136804, 2011. — p.52, 59.

[158] J. Topolancik, F. Vollmer, R. Ilic, and M. Crescimanno. Out-of-plane scattering from vertically asymmetric photonic crystal slab waveguides with in-plane disorder. *Optics Express*, 17:12470, 2009. — p.52, 55, 56.

[159] N. Le Thomas, H. Zhang, J. Jágerská, V. Zabelin, R. Houdré, I. Sagnes, and A. Talneau. Light transport regimes in slow light photonic-crystal waveguides. *Physical Review B*, 80:125332, 2009. — p.52, 53, 55.

[160] M. Spasenović, D.M. Beggs, P. Lalanne, T.F. Krauss, and L. Kuipers. Measuring the spatial extent of individual localized photonic states. *Physical Review B*, 86:155153, 2012. — p.52.

[161] P.V. Ruijgrok, R. Wüest, A.A. Rebane, A. Renn, and V. Sandoghdar. Spontaneous emission of a nanoscopic emitter in a strongly scattering disordered medium. *Optics Express*, 18:6360, 2010. — p.52.

[162] M.D. Birowosuto, S.E. Skipetrov, W.L. Vos, and A.P. Mosk. Observation of spatial fluctuations of the local density of states in random photonic media. *Physical Review Letters*, 105:013904, 2010. — p.52.

[163] V. Krachmalnicoff, E. Castanié, Y. De Wilde, and R. Carminati. Fluctuations of the local density of states probe localized surface plasmons on disordered metal films. *Physical Review Letters*, 105:183901, 2010. — p.52.

[164] R. Sapienza, P. Bondareff, R. Pierrat, B. Habert, R. Carminati, and N.F. van Hulst. Long-tail statistics of the purcell factor in disordered media driven by near-field interactions. *Physical Review Letters*, 106:163902, 2011. — p.52.

[165] S.R. Huisman, G. Ctistis, S. Stobbe, J.L. Herek, P. Lodahl, W.L. Vos, and P.W.H. Pinkse. Extraction of optical Bloch modes in a photonic-crystal waveguide. *Journal of Applied Physics*, 111:033108, 2012. — p.52, 54, 89.

[166] F. Riboli, P. Barthelemy, S. Vignolini, F. Intonti, A. De Rossi, S. Combrie, and D.S. Wiersma. Anderson localization of near-visible light in two dimensions. *Optics Letters*, 36:127, 2011. — p.52.

[167] Conference organized by B. Altshuler, B. Doucot, M. Mézard, G. Shlyapnikov. In *Conference on disordered quantum systems*, 2012. — p.52.

[168] S. Smolka, H. Thyrrestrup, L. Sapienza, T.B. Lehmann, K.R. Rix, L.S. Froufe-Pérez, P.D. García, and P. Lodahl. Probing the statistical properties of Anderson localization with quantum emitters. *New Journal of Physics*, 13(6):063044, 2011. — p.54, 55.

[169] S. John and T. Quang. Spontaneous emission near the edge of a photonic band gap. *Physical Review A*, 50:1764, 1994. — p.57.

[170] Z.-Y. Li and Y. Xia. Full vectorial model for quantum optics in three-dimensional photonic crystals. *Physical Review A*, 63:043817, 2001. — p.57, 59.

[171] L.I. Deych, D. Zaslavsky, and A.A. Lisyansky. Statistics of the Lyapunov exponent in 1d random periodic-on-average systems. *Physical Review Letters*, 81:5390, 1998. — p.59.

[172] Q. Wang, S. Stobbe, and P. Lodahl. Mapping the local density of optical states of a photonic crystal with single quantum dots. *Physical Review Letters*, 107:167404, 2011. — p.59.

[173] P.D. García, A. Javadi, H. Thyrrestrup, and P. Lodahl. Quantifying the intrinsic amount of fabrication disorder in photonic-crystal waveguides from optical far-field intensity measurements. *Applied Physics Letters*, 102:031101, 2013. — p.59, 86.

[174] B. Dayan, A. Pe'er, A.A. Friesem, and Y Silberberg. Two photon absorption and coherent

control with broadband down-converted light. *Physical Review Letters*, 93:023005, 2004. — p.63.

[175] S. Viciani, A. Zavatta, and M. Bellini. Nonlocal modulations on the temporal and spectral profiles of an entangled photon pair. *Physical Review A*, 69:053801, 2004. — p.63.

[176] J.F. Chen, S. Zhang, H. Yan, M.M.T. Loy, G.K.L. Wong, and S. Du. Shaping biphoton temporal waveforms with modulated classical fields. *Physical Review Letters*, 104:183604, 2010. — p.63.

[177] C. Polycarpou, K.N. Cassemiro, G. Venturi, A. Zavatta, and M. Bellini. Adaptive detection of arbitrarily shaped ultrashort quantum light states. *Physical Review Letters*, 109:053602, 2012. — p.63.

[178] C.W.J. Beenakker. Random-matrix theory of quantum transport. *Reviews of Modern Physics*, 69:731, 1997. — p.63.

[179] A.N. Boto, P. Kok, D.S. Abrams, S.L. Braunstein, C.P. Williams, and J.P. Dowling. Quantum interferometric optical lithography: exploiting entanglement to beat the diffraction limit. *Physical Review Letters*, 85:2733, 2000. — p.64.

[180] S.A. Goorden, M. Horstmann, A.P. Mosk, B. Škorić, and P.W.H. Pinkse. Quantum-secure authentication with a classical key. *ArXiv:1303.0142*, 2013. — p.64, 65.

[181] S.R. Huisman, N. Jain, S.A. Babichev, F. Vewinger, A.N. Zhang, S.H. Youn, and A.I. Lvovsky. Instant single-photon Fock state tomography. *Optics Letters*, 34:2739, 2009. — p.65, 82.

[182] E. Bimbard, N. Jain, A. MacRae, and A.I. Lvovsky. Quantum-optical state engineering up to the two-photon level. *Nature Photonics*, 4:243, 2010. — p.65.

[183] T.J. Huisman, S.R. Huisman, A.P. Mosk, and P.W.H. Pinkse. Characterization of a quantum light source based on spontaneous parametric down-conversion. *arXiv:1302.2816*, 2013. — p.65.

[184] W.P. Grice and I.A. Walmsley. Spectral information and distinguishability in type-II down-conversion with a broadband pump. *Physical Review A*, 56:1627, 1997. — p.65.

[185] I.M. Vellekoop and A.P. Mosk. Phase control algorithms for focusing light through turbid media. *Optics Communications*, 281:3071, 2008. — p.68, 76.

[186] T. Aichele, A.I. Lvovsky, and S. Schiller. Optical mode characterization of single photons prepared via conditional measurements on a biphoton state. *European Physical Journal D*, 18:237, 2002. — p.69.

[187] E. Hecht. *Optics*. Addison Wesley Longman, Inc., 4th edition, 2002. — p.71.

[188] B.E.A. Saleh and M.C. Teich. *Fundamentals of photonics*. Wiley-Interscience, second edition, 2007. — p.71.

[189] E. Knill, R. Laflamme, and G.J. Milburn. A scheme for efficient quantum computation with linear optics. *Nature*, 409:46, 2001. — p.71.

[190] P. Kok, W.J. Munro, K. Nemoto, T.C. Ralph, J.P. Dowling, and G.J. Millburn. Linear optical quantum computing with photonic qubits. *Reviews of Modern Physics*, 79:135, 2007. — p.71.

[191] I.M. Vellekoop, A. Lagendijk, and A.P. Mosk. Exploiting disorder for perfect focusing. *Nature Photonics*, 4:320–322, 2010. — p.71, 91.

[192] D.J. McCabe, A. Tajalli, D.R. Austin, P. Bondareff, I.A. Walmsley, S. Gigan, and B. Chatel. Spatio-temporal focussing of an ultrafast pulse through a multiply scattering medium. *Nature Communications*, 2:447, 2011. — p.71, 91.

[193] R.A. Campos, B.E.A. Saleh, and M.C. Teich. Quantum-mechanic lossless beam splitter:

SU(2) symmetry and photon statistics. *Physical Review A*, 40:1371, 1989. — p.72.

[194] T. Kiss, U. Herzog, and U. Leonhardt. Compensation of losses in photodetection and in quantum-state measurements. *Physical Review A*, 52:2433, 1995. — p.73.

[195] U. Leonhardt. *Measuring the quantum state of light*. Cambridge University Press, 1st edition, 1997. — p.73.

[196] S.M. Barnett, J. Jeffers, A. Gatti, and R. Loudon. Quantum optics of lossy beam splitters. *Physical Review A*, 57:2134, 1998. — p.73.

[197] L. Knöll, S. Scheel, E. Schmidt, D.-G. Welsch, and A.V. Chizhov. Quantum-state transformation by dispersive and absorbing four-port devices. *Physical Review A*, 59:4716, 1999. — p.73.

[198] J. Jeffers. Interference and the lossless lossy beam splitter. *Journal of Modern Optics*, 47:1819, 2000. — p.73.

[199] N.P. Puente, E.I. Chaikina, S. Herath, and A. Yamilov. Fabrication, characterization and theoretical analysis of controlled disorder in the core of the optical fibers. *Applied Optics*, 50:802, 2011. — p.81.

[200] C. Blum, N. Zijlstra, A. Lagendijk, M. Wubs, A.P. Mosk, V. Subramaniam, and W.L. Vos. Nanophotonic control of the Förster resonance energy transfer efficiency. *Physical Review Letters*, 109:203601, 2012. — p.85.

[201] K. Aoki, D. Guimard, M. Nishioka, M. Nomura, S. Iwamoto, and Y. Arakawa. Coupling of quantum-dot light emission with a three-dimensional photonic-crystal nanocavity. *Nature Photonics*, 2:688, 2008. — p.86.

[202] N. Le Thomas, R. Houdré, M.V. Kotlyar, and T.F. Krauss. Phase-sensitive fourier imaging of optical Bloch modes. *Physical Review B*, 77:245323, 2008. — p.86.

[203] M. Kuttge, E.J.R. Vesseur, A.F. Koenderink, H.J. Lezec, H.A. Atwater, F.J. García de Abajo, and A. Polman. Local density of states, spectrum, and far-field interference of surface plasmon polaritons probed by cathodoluminescence. *Physical Review B*, 79:113405, 2009. — p.86.

[204] D.P. Caetano, P.H. Souto Ribeiro, J.T.C. Pardal, and A.Z. Khoury. Quantum image control through polarization entanglement in parametric down-conversion. *Physical Review A*, 68:023805, 2003. — p.87.

[205] K. Srinivasan, M. Borselli, O. Painter, A. Stintz, and S. Krishna. Cavity Q, mode volume, and lasing threshold in small diameter AlGaAs microdisks with embedded quantum dots. *Optics Express*, 14:1094, 2006. — p.89.

Samenvatting

Verstrooiing en interferentie bepalen de transporteigenschappen van golven. Licht is een golfverschijnsel dat gemanipuleerd kan worden met optische nanostructuren. Licht gedraagt zich op unieke wijze in optische nanostructuren vanwege de combinatie van sterke veelvuldige verstrooiing en interferentie over lengteschalen vergelijkbaar met de golflengte. De resulterende transporteigenschappen zijn van belang voor onder andere optische communicatie, detectie, dataverwerking, microscopie, energieopwekking en fundamentele wetenschap.

In dit proefschrift staat het temmen van licht met optische nanostructuren centraal. Er worden zes experimenten beschreven die nieuwe onderzoeksrichtingen beschrijven. Deze experimenten zijn thematisch onderverdeeld in drie delen: I verboden zones voor licht in fotonische kristallen, II lichttransport in fotonische kristal golfgeleiders en III adaptieve kwantum optica. Het proefschrift vangt aan met een algemene introductie op deze drie thema's in hoofdstuk 1.

In deel I wordt onderzoek beschreven aan fotonische kristallen: een speciale klasse van periodiek geordende optische nanostructuren. De combinatie van verstrooiing en interferentie aan het periodieke rooster van fotonische kristallen zorgt ervoor dat licht met bepaalde energieën in specifieke richtingen niet kan voortbewegen door het kristal. Deze verboden energiebanden worden veroorzaakt door een algemeen golfinterferentiefenomeen dat is beschreven door de wet van Bragg. In deze sectie wordt onderzoek gepresenteerd naar verboden energiebanden in twee- en driedimensionale silicium fotonische kristallen door de structuren te beschijnen met licht met een breed energiespectrum. Door het energiespectrum van het gereflecteerde licht te bestuderen worden verboden energiebanden geïdentificeerd.

Theoretisch stond de laagste energie al bijna een eeuw lang onwrikbaar vast zoals voorspeld door de wet van Bragg. In hoofdstuk 2 wordt een speciale vorm van interferentie aangetoond waarbij verboden energiebanden ontstaan met lagere energieën. Dit verrassende interferentiefenomeen blijkt een universeel golfverschijnsel dat op kan treden in bijna de helft van alle klassen van kristalroosters. Wij noemen dit fenomeen *sub-Bragg* diffractie.

Het is voorspeld dat speciaal ontworpen driedimensionale fotonische kristallen een overlappende verboden energieband hebben voor alle richtingen en polarisaties van licht, beter bekend als een fotonische bandkloof. Deze kristallen hebben een kristalrooster geïnspireerd op het rooster van diamant. De fotonische bandkloof vormt een verboden zone voor licht, zoals de elektrische bandkloof dat doet voor elektronen in diamant. De realisatie van een fotonische bandkloof is mogelijk de grootste uitdaging op het gebied van optische nanostructuren en zou revolutionaire doorbraken leveren in de ontwikkeling van onzichtbaarheidsmantels, optische geheugens, efficiëntere lasers, LEDs en zonnecellen. Het aantonen

van de aanwezigheid van een fotonische bandkloof is iets waar niemand tot voor ons werk in was geslaagd. In hoofdstuk 3 wordt het gereflecteerde energiespectrum van deze fotonische kristallen onderzocht voor verschillende invalshoeken, polarisaties en posities. Een overlappende verboden energieband is aangetoond voor alle metingen, waaruit geconcludeerd kan worden dat deze kristallen zeer waarschijnlijk een fotonische bandkloof bevatten.

In deel II wordt onderzoek gepresenteerd aan lichttransport in fotonische kristal golfgeleiders met behulp van nabije-veld microscopie. De fotonische kristal golfgeleiders worden gevormd door een dunne laag GaAs waarin een gatenrooster een tweedimensionale fotonische kristal vormt, waarbij een enkele rij gaten is weggelaten. Licht wordt gedwongen om in deze ontbrekende rij gaten te blijven door het omliggende fotonische kristal en interne reflectie. Licht plant zich langzaam voort in deze structuren wat van belang is voor het beheersen van optische informatie overdracht en het vergroten van de gevoeligheid van nanosensoren. Normaliter blijft licht in deze structuren ingesloten en dus is het lastig om in kaart te brengen hoe het in een structuur beweegt. Nabije-veld microscopie is een unieke techniek die het mogelijk maakt om lokaal het lichtveld te meten terwijl het zich bevindt in fotonische kristal golfgeleiders.

Licht kan met verschillende polarisaties in beide richtingen door een fotonische kristal golfgeleider bewegen. Dit maakt het ingewikkeld om een specifieke toestand van het lichtveld te bestuderen waarbij het licht een gedefinieerde polarisatie en propagatierichting kent. In hoofdstuk 4 wordt een methode toegepast waarbij met behulp van nabije-veld microscopie specifieke lichttoestanden bestudeerd kunnen worden.

Zelfs de meest geavanceerde nanostructuren wijken iets af van het perfecte object dankzij de minieme hoeveelheid wanorde die onvermijdelijk aanwezig is door bijvoorbeeld fabricageprocessen of materiaaleigenschappen. Dit kan leiden tot extra verstrooiing en interferentie in de structuur, wat resulteert in een trilholte voor licht waarin het gevangen komt te zitten. Dit zorgt voor een significante wijziging in het transport van licht nabij verboden energiebanden. In hoofdstuk 5 wordt het effect van wanorde op licht transport in fotonische kristal golfgeleiders bestudeerd. De energie-afhankelijke transporteigenschappen van deze nanostructuren rond de verboden energiebanden zijn volledig in kaart gebracht. De kans dat licht vast komt te zitten neemt toe wanneer de golven zich langzamer voortbewegen. Het gevolg is dat licht gevangen wordt op willekeurige locaties in de golfleider voor energieën dichtbij verboden energiebanden. Zelfs in de verboden energiebanden wordt licht opgesloten. Dit verschijnsel is 60 jaar geleden voorspeld door Lifshitz en aangetoond voor elektronen. Wij laten nu voor het eerst hetzelfde verschijnsel zien voor licht.

In deel III worden compleet wanordelijke optische nanostructuren onderzocht. Dikke ondoorzichtig materialen, zoals witte verflagen, blijken een zeer interessant platform te zijn voor optische experimenten. Veelvuldige verstrooiing en interferentie zorgen ervoor dat licht zich gedraagt alsof het door een optisch doolhof propageert bestaande uit een complex lineair optische circuit gevormd door

elementen zoals spiegels, lenzen en bundelsplitsers. Als een wanordelijk optisch materiaal belicht wordt met een gemodificeerd belichtingspatroon, kan licht op een gewenste manier door dit doolhof bewegen. Op deze manier kan een witte verflaag worden gebruikt als een lineair optisch circuit dat programmeerbaar is in functionaliteit. Dit is ook toepasbaar voor kwantumtoestanden van licht, zoals enkele inkomende fotonen. Dit maakt het mogelijk om kwantuminterferentie te programmeren met behulp van wanordelijke optische nanostructuren, iets wat wij *adaptieve kwantum optica* noemen. In deze sectie worden twee experimenten beschreven die nodig zijn om een Hong-Ou-Mandel interferometrie experiment te doen waarbij de bundelsplitser wordt gevormd door een witte verflaag. Dit vormt de allereerste demonstratie van adaptieve kwantum optica.

Voor het Hong-Ou-Mandel experiment met een witte verflaag als bundelsplitser moet allereerst worden aangetoond dat enkele fotonen programmeerbaar door een wanordelijke optisch materiaal kunnen bewegen. In hoofdstuk 6 worden de kwantumlichtbron beschreven en aangetoond dat het golffront van enkele fotonen gecontroleerd kan worden. Dit vormt de eerste demonstratie van programmeerbare propagatie van enkele fotonen door een wanordelijk optische nanostructuur.

Het Hong-Ou-Mandel experiment heeft een bundelsplitser nodig. In hoofdstuk 7 worden twee inkomende lichtbundels op een witte verflaag dusdanig gemanipuleerd dat het belichtingsspattroon twee uitgaande bundels veroorzaakt. Doormiddel van interferentie experimenten blijkt dat deze twee uitgaande bundels zich bij benadering vrijwel hetzelfde gedragen als de uitgangen van een normale bundelsplitser. Dit werk vormt de basis voor de realisatie van complexere lineaire optische elementen.

In hoofdstuk 8 wordt een samenvatting gegeven van het proefschrift en worden suggesties aangedragen voor toekomstig onderzoek. Appendix A beschrijft een combinatie van het werk van hoofdstuk 4 en 5 waarbij een enkele gevangen toestand van licht langs een fotonische kristal golfgeleider wordt bestudeerd. Appendix B beschrijft theoretisch en experimenteel werk gebaseerd op hoofdstuk 7 over een algemeen toepasbaar algoritme dat het mogelijk maakt om arbitraire lineaire optische circuits te programmeren in wanordelijke optische nanostructuren. Dit algoritme werkt als het ware als een TomTom voor lichtpropagatie. Gebaseerd op dit algoritme is een afschatting gemaakt van hoe efficiënt een bundelsplitser kan zijn die gevormd wordt door een wanordelijk optische nanostructuur. Simulaties hierover worden gepresenteerd in appendix C.

Dankwoord

Het doen van een promotie is meer dan het uitvoeren van een onderzoek en worden opgeleid tot onderzoeker. Het zijn de persoonlijke ontwikkelingen die ik heb doorgemaakt die ik belangrijkst vind. Ik wil dit gedeelte van mijn proefschrift gebruiken om mijn dank te betuigen aan de mensen die hierbij een belangrijke rol hebben gespeeld. Promoveren doe je immers niet alleen.

Ik wil mijn begeleider Pepijn bedanken voor zijn advies, vertrouwen, ondersteuning en enthousiasme. Ik stel onze open discussies zeer op prijs en ik ben blij dat ik mijn ideeën voor AQUO heb mogen doorzetten. Ik ben mijn promotoren Willem en Jennifer dankbaar voor hun expertise, opleiding en ondersteuning. Willem en ik hebben veel meegemaakt sinds dat ik in de zomer van 2007 voor het eerst voet binnen zijn leerstoel zette, voor alle ervaringen ben ik dankbaar. Ik wil Jennifer bedanken voor haar oprechte persoonlijke interesse en de mogelijkheden die zij mij heeft geboden.

De leden van COPS en OS ben ik dankbaar voor de bijdrage die zij hebben geleverd. Onderzoeksgroepen kunnen niet functioneren zonder technische ondersteuning, ik ben veel dank verschuldigd aan Cock, Frans, Hannie, Iwert, Jeroen, Klaas, Léon en Willem. De administratieve ondersteuning van Karen, Marscha en Nilda was onmisbaar. Ik bedank de uitwisselingsstudenten Eric en Henry voor hun hulp bij de nabije-veld metingen. De goede samenwerking met onze Deense collega's David, Henri, Søren en Peter hebben geleid tot prachtig onderzoek. Ik wil Merel bedanken voor haar uitstekende begeleiding. Ik ben de volgende mensen dankbaar voor hun bijdrage: Ad, Alex, Alexander, Allard, Amandev, Bas, Bergin, Bernard, Danang, Dirk Jan, Elbert, Emre, Erik, Femius, Georgios, Harold, Herman, Ivo, Jacopo, Jochen, Klaus, Kobus, Martin, Mirko, Nitin, Paolo, Patrick, Philip, Rajesh, Ramy, Robert, Sanli, Timmo en Tom.

In het bijzonder zou ik mijn broer Thomas willen bedanken voor zijn inzet als afstudeerstudent. Het was ontzettend prettig en een unieke ervaring om samen te werken. Veel hard werken van ons beiden heeft geleid tot prachtige wetenschap.

Ik heb veel van mijn persoonlijke ontwikkeling te danken aan het wedstrijddansen. Ik ben mijn danspartner Sabine en mijn voormalige danspartners Leonie en Wendy dankbaar voor de mooie tijd op de dansvloer. Ik heb veel ondersteuning gehad van Herman, Michèle, Ewoud, Anastasia, Bas, Aletta, Gerben, Erik, Isao, Shirley en Gert.

Ik wil afsluiten met het bedanken van mijn familie, met name mijn ouders René en Rita. Zij hebben mij altijd opgevangen en ondersteund op ontzettend veel manieren.

- Simon Huisman, Juli 2013 -

Propositions

belonging to the thesis

LIGHT CONTROL WITH
ORDERED AND DISORDERED NANOPHOTONIC MEDIA

by Simon R. Huisman

Proposition 1 *Sub-Bragg diffraction affects the melting point of ice and therefore influences our calibration of temperature.*

- Chapter 2 -

Proposition 2 *Not so much new fabrication methods, but rather sophisticated theory on finite-size photonic crystals is warranted to advance the study on light interaction with photonic band gap crystals.*

- Chapter 3 -

Proposition 3 *Two-dimensional random scattering media offer the most versatile platform for programmable interference.*

- Chapters 6 and 7 -

Proposition 4 *The cost of a single-photon counting module scales approximately inversely proportional to its dark count rate.*

Proposition 5 *Every good scientist has to act sometimes like a successful scientist to become a better scientist.*

- Inspired by A. Lagendijk (2012) -

Proposition 6 *Scientists should heed commercial billboard advertisements in order to deliver a message.*

Proposition 7 *The modern Dutch policy on connecting wildlife areas is a waste of resources as long as agriculture is protected.*

Proposition 8 *To present, pretend, and participate are key components in biasing public judgment.*